

Dissertation
submitted to the
Combined Faculties of the Natural Sciences and Mathematics
of the Ruperto-Carola-University of Heidelberg, Germany
for the degree of
Doctor of Natural Sciences

Put forward by

Christian Arnold

born in: Lichtenstein

Oral examination: 24.05.2017

Hydrodynamical cosmological simulations in

$f(R)$ modified gravity

Referees: Prof. Dr. Volker Springel

Prof. Dr. Luca Amendola

Hydrodynamical cosmological simulations in $f(R)$ modified gravity

I study the effects of Hu & Sawicki (2007) $f(R)$ -gravity on astrophysical processes and cosmological observables. Employing hydrodynamical cosmological simulations carried out with the MG-GADGET and AREPO codes in modified gravity the influences on the Lyman- α forest, Milky-Way sized halos, clustering and lensing on large scales as well as on the Sunyaev-Zeldovich effect are investigated. Comparing MG-GADGET to other codes I find that different $f(R)$ -gravity simulation methods agree on a percent-level accuracy for matter power spectra and halo profiles. The $f(R)$ effects are in general smaller at higher redshift, resulting in very small differences between $f(R)$ -gravity and general relativity (GR) for the Lyman- α forest. Structural properties of Milky-Way sized halos are however altered by up to 40%. Requiring that the Solar system is screened within the Milky-Way leads to $|\bar{f}_{R0}| = 10^{-6}$ as a constraint on the background parameter. The fifth force is well described by a theoretical approximation in ideal NFW-halos while this estimate is much less accurate for realistic halos. Two point correlation functions and angular power spectra are increased in $f(R)$ -gravity compared to GR. Dark matter halos are in contrast less strongly correlated, leading to a lower halo clustering bias in $f(R)$ -gravity. The angular power in both thermal and kinetic Sunyaev-Zeldovich maps is by a few percent higher in modified gravity compared to a Λ CDM model.

Hydrodynamische kosmologische Simulationen in $f(R)$ -Gravitation

Diese Arbeit untersucht die Auswirkungen von Hu & Sawicki (2007) $f(R)$ -Gravitation auf astrophysikalische Prozesse und kosmologische Messgrößen. Mit Hilfe von hydrodynamischen kosmologischen Simulationen mit den Programmen MG-GADGET und AREPO werden die Einflüsse von modifizierter Gravitation auf das Lyman- α Absorptionsspektrum, milchstraßengroße Halos, Kosmische Großraumstruktur, Gravitationslinseneffekte sowie den Sunyaev-Zeldovich Effekt analysiert. Ein Vergleich zwischen MG-GADGET und anderen $f(R)$ -Simulationsprogrammen zeigt, dass die Simulationsergebnisse für Materie-Leistungsspektren und Halo Profile bis auf wenige Prozent übereinstimmen. Die Effekte durch $f(R)$ -Gravitation sind im Allgemeinen zu früheren Zeiten schwächer, wodurch auch die Auswirkungen auf den Lyman- α Effekt schwer messbar sind. Die strukturellen Eigenschaften von milchstraßenähnlichen Halos ändern sich allerdings um bis zu 40%. Verlangt man abgeschirmte $f(R)$ -Kräfte im Sonnensystem, ergibt sich ein maximal erlaubtes Hintergrundfeld von $|\bar{f}_{R0}| = 10^{-6}$. Die $f(R)$ -Kraft kann in idealen NFW-Halos gut durch theoretische Approximationen beschrieben werden, für realistische Halos funktionieren diese Näherungen jedoch deutlich schlechter. Zwei-Punkt Korrelationsfunktionen und Winkelleistungsspektren zeigen in $f(R)$ -Gravitation im Vergleich zu Allgemeiner Relativitätstheorie höhere Werte, während Halos aus dunkler Materie weniger stark korreliert sind. Das führt zu einem geringeren Halo Bias in $f(R)$ -Gravitation. Die thermischen und kinetischen Winkel-Leistungsspektren des Sunyaev-Zeldovich Effekts weisen durch die modifizierte Gravitation um einige Prozent höhere Werte auf.

Contents

1	Introduction	9
2	Theory	11
2.1	The standard model of cosmology	11
2.1.1	A brief overview	11
2.1.2	Reasons to look beyond GR	12
2.2	Modified gravity	13
2.2.1	Screening by deep potentials	13
2.2.2	Screening by derivatives of interactions	15
2.3	The $f(R)$ -Universe	16
2.3.1	$f(R)$ -gravity from a GR perspective	16
2.3.2	$f(R)$ -gravity formulated as a scalar tensor theory	19
2.3.3	The Newtonian limit of $f(R)$ -gravity	20
2.3.4	Chameleon screening in $f(R)$ -gravity	22
2.3.5	$f(R)$ cosmology	22
2.3.6	The functional form of $f(R)$	24
2.3.7	Current constraints on $f(R)$ -gravity	26
2.3.8	Screening in spherically symmetric objects	27
3	Numerics	31
3.1	Modified gravity simulations	31
3.2	MG-GADGET	32
3.2.1	P-GADGET3	32
3.2.2	The modified gravity solver	33
3.2.3	Local timestepping in MG-GADGET	37
3.3	AREPO	41
3.3.1	The modified gravity solver in AREPO	42
4	The modified gravity code comparison project	44
4.1	Introduction	44
4.2	Simulations and Methods	44
4.3	Results	45
4.4	Conclusion and discussion	53
5	The Lyman-α forest in $f(R)$-gravity	56
5.1	Introduction	56
5.2	Simulations and methods	56

5.3	Results	63
5.4	Summary and Conclusions	68
6	Zoomed cosmological simulations in $f(R)$-gravity	70
6.1	Introduction	70
6.2	Simulations and methods	70
6.3	Results	75
6.3.1	Ideal NFW halos	75
6.3.2	The Aquarius halos	78
6.4	Summary and Conclusions	88
7	The Modified Gravity Lightcone Simulations	90
7.1	Introduction	90
7.2	Simulations and methods	90
7.3	Results	91
7.4	Conclusion and discussion	100
8	The Sunyaev-Zeldovich effect in $f(R)$-gravity	102
8.1	Introduction	102
8.2	Simulations and Methods	102
8.3	Results	104
8.4	Conclusion and Discussion	106
9	Discussion and Outlook	108
10	List of publications	115
11	Bibliography	116

1 Introduction

The discovery of the accelerated expansion of the Universe (Riess *et al.*, 1998) raised the question of how to theoretically account for this effect. In the standard model of cosmology, the Λ Cold Dark Matter (Λ CDM) model, the accelerated expansion is explained by the cosmological constant. On the one hand the Λ CDM model is a great success and is to date consistent with almost all observational data (see e.g. Planck Collaboration *et al.*, 2016a). On the other hand it also features a few problems, one of them being the lack of a motivation for Λ . The discovery of the accelerated expansion of the Universe therefore not only manifested the success of the Λ CDM model but also triggered an intense search for alternative theories which can explain the acceleration (Dvali *et al.*, 2000; Hinterbichler & Khoury, 2010; Joyce *et al.*, 2015).

These theories can be roughly grouped into two categories, the dark energy and the modified gravity models. Dark energy models add a new type of field to Einstein's equations. If the field is described by an effective equation of state with negative effective pressure, it can account for the accelerated expansion of our Universe (Wetterich, 1988; Caldwell, 2002). Theories of modified gravity on the other hand modify the laws of gravity to achieve the same effect (Hu & Sawicki, 2007). As general relativity (GR) is very well tested in the solar system (Will, 2014), these modifications must be negligibly small in our local environment. Otherwise the considered theory would be immediately ruled out. In order to hide the modifications to Einstein's GR in our neighborhood, practically all modified gravity models employ a so called screening mechanism. These mechanisms are usually triggered by deep gravitational potentials or steep potential gradients and ensure that the theory behaves like GR in high density environments (Jain & Khoury, 2010; Clifton *et al.*, 2012).

The fact that the modifications to gravity are screened in our local environment does immediately imply that the only way to observationally test modified gravity theories is to look for signatures on larger scales or in lower density regions. In the coming years a number of large scale structure surveys, e.g., EUCLID (Amendola *et al.*, 2013) and LSST (Ivezic *et al.*, 2008), will be carried out in order to perform such a test of gravity on large scales. In order to do so, they nevertheless require a detailed understanding of how structure formation is altered by theories of modified gravity.

Apart from being a possible explanation for the accelerated expansion of the universe, modified gravity theories are an alternative to GR. Testing for these models with the mentioned surveys is thus an independent test of gravity on the largest scales. Work on modified gravity will therefore contribute to answer one of the

most important questions in fundamental physics, i.e., the question on the nature on gravity.

The need for a screening mechanism in modified gravity leads to a very non-linear behaviour of the underlying equations. Analytic approaches to cosmic structure formation are therefore even more limited than for the standard cosmology. These limitations resulted in a very active development of a number of cosmological N-body simulation codes for various theories (Oyaizu, 2008; Schmidt *et al.*, 2009; Dvali *et al.*, 2000; Li *et al.*, 2012). These codes can efficiently simulate cosmic structure formation and fully cover the modified gravity effects including the screening mechanisms.

In this thesis, I consider $f(R)$ -gravity which was first mentioned by Buchdahl (1970). This theory modifies Einstein's GR by adding a scalar function of the Ricci scalar to its action. It features the chameleon screening mechanism which screens regions with deep potentials to recover GR in the solar system. If the functional form of $f(R)$ is properly chosen, the theory can account for the accelerated expansion of the universe. In this work, I use the form proposed by Hu & Sawicki (2007) which features an expansion history close to that of a Λ CDM universe.

To find observable cosmological and astrophysical signatures of $f(R)$ -gravity, I performed N-body simulations with the codes MG-GADGET (Puchwein *et al.*, 2013) and AREPO (Springel, 2010). The range of simulations covers both collision-less and hydrodynamical cosmological simulations but also such employing zoomed simulation techniques. To extend the capabilities of the codes I developed them further and implemented e.g. a local timestepping scheme in MG-GADGET and the modified gravity solver in AREPO. As a result of constant optimization work during this thesis both codes can nowadays be used to very efficiently simulate structure formation in $f(R)$ modified gravity.

The simulations I ran are dedicated to analyze the Lyman- α forest, Milky Way sized halos, clustering and lensing on the largest scales and the Sunyaev-Zeldovich (SZ) effect in $f(R)$ -gravity. I also carried out work for a modified gravity code comparison project which was carried out to identify potential differences and shortcomings of various modified gravity simulation techniques (Winther *et al.*, 2015).

This thesis is structured as follows. In Chapter 2 I give a theoretical overview over modified gravity. I specifically concentrate on $f(R)$ -gravity and its implications for cosmology but also make theoretical predictions which are later compared to the simulations. Chapter 3 introduces the codes and the modified gravity simulation techniques. I explain the code developments I carried out during this thesis in this Chapter as well. The results of the modified gravity code comparison project are presented in Chapter 4. In Chapter 5 I discuss how the Lyman- α forest is affected by $f(R)$ -gravity. The next chapter presents the results of zoomed cosmological simulations of Milky Way sized halos in modified gravity. The outcomes of the modified gravity light-cone simulation project are presented and discussed in Chapter 7. First results on the Sunyaev-Zeldovich effect in $f(R)$ -gravity which were obtained through simulations with AREPO are shown in Chapter 8. In Chapter 9 I finally summarize and discuss the results of the work carried out during this thesis and give an outlook on its implications for future research in the field of modified gravity simulations.

2 Theory

2.1 The standard model of cosmology

More than a decade ago the discovery of the accelerated expansion of the Universe (Riess *et al.*, 1998) led to the establishment of what is nowadays called standard model of cosmology, the Λ Cold Dark Matter (Λ CDM) model. Up until now it is – with very few tensions – compatible with all cosmological measurements. The two main ingredients, dark matter and dark energy in the form of a cosmological constant, are nevertheless not well understood yet. While dark matter is cosmologically known to be one or several types of particles whose interactions are effectively limited to gravity (possibly along with a weak interaction) nothing has been detected on the particle physics side yet. The cosmological constant can on the other hand very well explain the expansion history of the universe but its theoretical motivation is still unclear.

2.1.1 A brief overview

Starting out with GR with a cosmological constant Λ as a gravitational theory and adopting the principle cosmological assumptions of homogeneity and isotropy the large scale dynamics in the Λ CDM model is described by Friedmann’s equations (Friedmann, 1922) (which can be derived from the mentioned ingredients):

$$\left(\frac{\dot{a}}{a}\right)^2 = \frac{8\pi G}{3}\rho - \frac{Kc^2}{a^2} + \frac{\Lambda c^2}{3} \quad (2.1)$$

$$\frac{\ddot{a}}{a} = -\frac{4\pi G}{3}\left(\rho + \frac{3p}{c^2}\right) + \frac{\Lambda c^2}{3} \quad (2.2)$$

and the underlying Friedmann-Robertson-Walker (FRW) metric

$$ds^2 = -c^2 dt^2 + a^2(t) [dw^2 + f_K^2(w)d\Omega^2]. \quad (2.3)$$

Here a is the scale factor and ρ and p are the spatially homogeneous (on sufficiently large scales) but time dependent density and pressure, respectively. The gravitational constant is denoted as G , c is the speed of light. For a spatially flat universe (observations show that the universe is at least very close to flat, see e.g. Planck Collaboration *et al.*, 2016a), the curvature is $K = 0$ and the radial function $f_K(w) = w$, where w is the radius in polar coordinates.

The matter content of the universe is usually given in terms of a critical density

$$\rho_{cr} = 3\frac{H^2}{8\pi G}, \quad (2.4)$$

2 Theory

where $H \equiv \dot{a}/a$ is the Hubble parameter, i.e. the relative expansion rate. In a sphere filled with matter of critical density, the gravitational forces are exactly balanced by the expansion of the universe. The matter-energy content of the universe is now specified by

$$\Omega_m = \frac{\rho_m}{\rho_{crit}} \quad \text{and} \quad \Omega_r = \frac{\rho_r}{\rho_{crit}}, \quad (2.5)$$

for the matter and radiation density, respectively. It is also possible to define a density parameter associated with the field of the cosmological constant:

$$\Omega_\Lambda = \frac{\Lambda}{3H^2}. \quad (2.6)$$

Inserting the density parameters into Friedmann's equations yields an expression for the Hubble parameter as a function of time in an FRW universe

$$H^2(a) = H_0^2 \left[\frac{\Omega_{R0}}{a^4} + \frac{\Omega_{m0}}{a^3} + \Omega_\Lambda + \frac{\Omega_{K0}}{a^2} \right], \quad (2.7)$$

where the zeros denote values at zero redshift $z = \frac{1-a}{a}$.

2.1.2 Reasons to look beyond GR

There are several reasons to explore and test alternatives to the standard model and GR. First of all it is not clear that the standard model is the most appropriate description of our universe. In the past years a number of alternatives, i.e., models with a different description of dark energy or modifications to gravity have been developed (Wetterich, 1988; Dvali *et al.*, 2000; Nicolis *et al.*, 2009; Hinterbichler & Khoury, 2010). Many of them are, at first glance, as viable as the standard model and therefore deserve to be explored further as well.

A second reason are the requirements of upcoming surveys of the large scale structure of the universe like EUCLID or LSST. These surveys are designed to test the cosmological model and gravity on the largest scales. In order to do so, they require a detailed theoretical understanding of how possible modifications to the standard model or GR affect cosmological measures and what signatures to look for in order to stress the cosmological model and standard gravity.

Thirdly, the problems with the cosmological constant are a very strong argument to look for alternatives. Along with the lack of an elegant theoretical explanation for Λ there are two major difficulties. On the one hand the old cosmological constant problem just asks the question: "where does Λ come from?" It can be addressed by many modified gravity theories which explain the late time accelerated expansion of the universe by modifications to GR and have no need for a cosmological constant. On the other hand there is the so called new cosmological constant problem, asking the question why the vacuum energy of QCD is many orders of magnitude larger than the energy density required to account for the accelerated expansion. So far,

there is no way to hide this energy density, e.g. via a QFT symmetry. Unfortunately, almost all modified gravity and dark energy models struggle to solve this problem as well.

2.2 Modified gravity

As pointed out above, there are several reasons to consider alternatives to the standard model of cosmology. These alternatives can be grouped in two classes, dark energy and modified gravity models. The former group of theories adds fields (one could also phrase it as a type of "matter") to the right hand side of Einstein's equations. If these fields have an effective equation of state with negative effective pressure, they can account for the accelerated expansion. Examples for such dark energy models are Quintessence (Wetterich, 1988; Peebles & Ratra, 1988), Phantom dark energy (Caldwell, 2002) or coupled dark energy models (Wetterich, 1995; Amendola, 2000).

The latter group of theories modifies the laws of gravity to account for the accelerated expansion. As GR is tested to a very high precision in the Solar system (Will, 2014), theories of modified gravity share the need for a mechanism which hides the modifications to the left hand side of Einstein's equations in our local environment. In order to give an overview of modified gravity models I will therefore follow Joyce *et al.* (2015) and group them according to their mode of screening.

2.2.1 Screening by deep potentials

For a large group of modified gravity theories the screening mechanism depends on the depth of the (Newtonian) gravitational potential Φ . If the gravitational potential depth becomes too large, e.g. in high density environments, the screening mechanism will become active and shield the modifications to GR. Theories of this kind can in general be described by the following action, i.e. written as a scalar tensor theory

$$S = \int d^4x \sqrt{-g} \left[\frac{R}{16\pi G} - \frac{1}{2}(\partial\phi)^2 - V(\phi) \right] + S_M(A(\phi)^2 g_{\mu\nu}, \psi), \quad (2.8)$$

where ϕ is a scalar field with the potential $V(\phi)$, which does couple to the matter action via $A(\phi)$. The acceleration of a test particle is then given by

$$\mathbf{a} = -\nabla [\Phi + \ln A(\phi)]. \quad (2.9)$$

Assuming a FLRW metric and a non-relativistic source of matter the field equation for ϕ resulting from (2.8) is (using the notation $\partial_\phi x = x_{,\phi}$)

$$\square\phi = V_{\text{eff},\phi}(\phi), \quad \text{where} \quad V_{\text{eff}}(\phi) = V(\phi) + A(\phi)\rho. \quad (2.10)$$

The dependence of the effective potential V_{eff} on the matter density ρ is the key point here. By appropriately choosing the potential and the field's coupling to matter, one

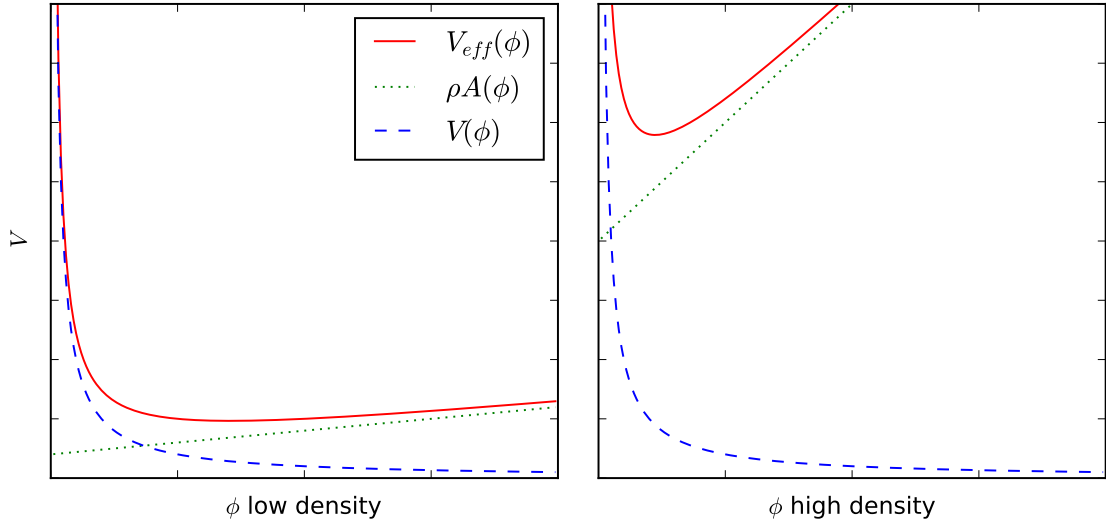


Figure 2.1: The effective potential of the chameleon V_{eff} and its constituents $V(\phi)$ and $\rho A(\phi)$ in low and high density regions.

can – according to (2.10) – create a theory which features modifications to gravity in low density regions but suppresses these in high density environments. Let me now discuss different examples for such a screening mechanism.

Chameleon screening

The chameleon mechanism acts through a density dependent mass of the scalar field (Khouri & Weltman, 2004a,b; Brax *et al.*, 2004). In low density regions the mass is small allowing for a considerable matter coupling while a high mass in high density regions suppresses the coupling to matter and with that the modifications to gravity. The mass is given by the second derivative of V_{eff} at its minimum ϕ_{min}

$$m_{\text{min}}^2(\phi_{\text{min}}) = V_{,\phi\phi}(\phi_{\text{min}}) + A_{,\phi\phi}(\phi_{\text{min}})\rho. \quad (2.11)$$

To demonstrate how the chameleon mechanism works I will now choose a very simple model (first considered in Khouri & Weltman, 2004a) with

$$A(\phi) = e^{\frac{\xi\phi}{M_{\text{Pl}}}} \approx 1 + \xi \frac{\phi}{M_{\text{Pl}}}, \quad (2.12)$$

$$V(\phi) = \frac{M^{4+n}}{\phi^n}, \quad (2.13)$$

where M is a mass scale and $n > 0$ is a constant. The mass of the field is then given by

$$m_{\text{min}}^2(\rho) = n(n+1)M^{-\frac{4+n}{1+n}} \left[\frac{\rho\xi}{nM_{\text{Pl}}} \right]^{\frac{2+n}{1+n}}. \quad (2.14)$$

It obviously increases with increasing density. The behaviour of the effective potential is also illustrated in Figure 2.1. Its curvature at the minimum is small in low density regions, resulting in a small effective mass and an effective gravitational coupling. In high density regions, the curvature at the minimum is large due to the contribution of $\rho A(\phi)$. The effective mass is consequently much bigger and suppresses an efficient coupling of the scalar field to matter.

For a spherically symmetric source the field will in general take the form of a Yukawa potential (Hu & Sawicki, 2007; Joyce *et al.*, 2015)

$$\phi \propto \frac{e^{-m_{\min} r}}{r}. \quad (2.15)$$

This has several implications. If the mass of the field is high (e.g. inside heavy objects) the field contribution from these regions will be suppressed due to the Yukawa term. In regions with moderately low field mass but still close (in terms of $r < m_{\min}^{-1}$) to the source, the field will drop in the same way as a Newtonian potential and give a force contribution. Very far away from the object, i.e. $r > m_{\min}^{-1}$ the field is suppressed by the Yukawa term again. An example for a theory featuring the chameleon screening mechanism is $f(R)$ -gravity, which I consider in this work.

Symmetron screening

The Symmetron screening mechanism is also triggered by deep gravitational potentials but acts through a density dependent coupling of the scalar field (Hinterbichler & Khoury, 2010; Hinterbichler *et al.*, 2011). More specifically, the strength of the scalar field to matter coupling is proportional to the vacuum-expectation-value (VEV) of the field. In low curvature environments the field gains a non-zero VEV through spontaneous symmetry breaking and thus contributes to the gravitational forces. In high density regions the symmetry is restored resulting in a zero VEV for the scalar field and a suppressed coupling to matter.

The Symmetron screening mechanism is used in the Symmetron gravity models. Another screening mechanism which acts through a density dependent coupling is the Dilaton mechanism. It acts very similarly to the Symmetron mechanism and I will therefore not go into further detail here.

2.2.2 Screening by derivatives of interactions

Kinetic screening

Another possibility to construct a screening mechanism is to concentrate on the first order derivatives of the scalar field ϕ . As the Lagrangian must be a scalar, these derivatives can only appear in combinations of $\partial_\mu \phi \partial^\mu \phi$ and multiples of that. Kinetic screening then acts in a way that allows a force contribution due to ϕ far away from a source while the ratio of this force to the standard gravity force shrinks with decreasing distance to the source (Joyce *et al.*, 2015).

Vainshtein screening

The Vainshtein screening mechanism is a special variant of kinetic screening. To give a rough impression how it works, I will choose the galileon gravity model as an example theory. Around a spherically symmetric source, galileons show two modes of operation (Joyce *et al.*, 2015). Assuming a static solution around the spherical source of mass m , the scalar field ϕ can be described by

$$\phi'(r) = \frac{3\Lambda r}{4} \left[-1 + \sqrt{1 + \frac{1}{9\pi} \left(\frac{r_V}{r} \right)^2} \right], \quad (2.16)$$

where

$$r_V \equiv \Lambda^{-1} \left[\frac{gM}{M_{\text{Pl}}} \right]^{\frac{1}{3}} \quad (2.17)$$

is the Vainshtein radius. If $r \gg r_V$, the field will thus be proportional to a $1/r^2$ profile with a fifth force contribution of $F_\phi = \frac{g^2}{3} F_{\text{GR}}$. The constant g sets the coupling strength. Close to the source, i.e. $r \ll r_V$, the modified gravity force contribution shrinks to

$$F_\phi = \left(\frac{r}{r_V} \right)^{\frac{3}{2}} F_{\text{GR}} \ll F_{\text{GR}}. \quad (2.18)$$

The modifications to gravity will consequently be screened in this area. The Vainshtein effect is also responsible for the screening in many theories of massive gravity which I will not consider in more detail here.

2.3 The $f(R)$ -Universe

2.3.1 $f(R)$ -gravity from a GR perspective

The field equations of $f(R)$ -gravity can be derived in a GR framework. This is also the way Buchdahl (1970) derived the field equations when he first mentioned the theory. The action is very similar to that of GR, except for an additional scalar function of the Ricci scalar R , $f(R)$:

$$S = \int d^4x \sqrt{-g} \frac{R + f(R)}{16\pi G} + S_{\text{M}}(g_{\mu\nu}, \phi), \quad (2.19)$$

where g is the determinant of the metric $g_{\mu\nu}$ and S_{M} is the matter action depending only on the metric and the matter fields ϕ . In GR one could now vary the action in different ways but would still end up with the same theory. This is not the case for $f(R)$ -gravity. Varying the action with respect to the metric leads to metric $f(R)$ -gravity, the most widely studied $f(R)$ -theory and also the model I consider in

this work. If the action is in contrast varied with respect to both the metric and an independent connection, one arrives at Palatini $f(R)$ -gravity (Sotiriou, 2006).

Let me now go through the derivation of the field equations for the metric formalism. Requiring the variation of the metric to vanish one starts out from

$$0 = \delta S = \frac{1}{16\pi G} \int d^4x \delta \sqrt{-g} [R + f(R)] + \sqrt{-g} \delta [R + f(R)] + \delta S_M(g_{\mu\nu}, \phi), \quad (2.20)$$

where

$$\delta \sqrt{-g} = -\frac{\delta g}{2\sqrt{-g}} = -\frac{g_{\mu\nu}}{2} \sqrt{-g} \delta g^{\mu\nu} \quad (2.21)$$

and

$$\delta [R + f(R)] = \delta R + F(R) \delta R = [1 + F(R)] \delta R. \quad (2.22)$$

The derivative of the scalar function with respect to R is denoted as $F(R) \equiv \partial f(R)/\partial R$. The variation of the Ricci scalar is in turn given by

$$\delta R = \delta R_{\mu\nu} g^{\mu\nu} + R_{\mu\nu} \delta g^{\mu\nu} \quad (2.23)$$

$$= [\nabla_\gamma (\delta \Gamma_{\mu\nu}^\gamma) - \nabla_\nu (\delta \Gamma_{\mu\gamma}^\nu)] g^{\mu\nu} + R_{\mu\nu} \delta g^{\mu\nu} \quad (2.24)$$

$$= [\nabla_\gamma (g^{\mu\nu} \delta \Gamma_{\mu\nu}^\gamma) - \nabla_\nu (g^{\mu\nu} \delta \Gamma_{\mu\gamma}^\nu)] + R_{\mu\nu} \delta g^{\mu\nu} \quad (2.25)$$

$$= \nabla_\gamma [g^{\mu\nu} \delta \Gamma_{\mu\nu}^\gamma - g^{\mu\gamma} \delta \Gamma_{\mu\nu}^\nu] + R_{\mu\nu} \delta g^{\mu\nu} \quad (2.26)$$

$$\equiv \nabla_\gamma W^\gamma + R_{\mu\nu} \delta g^{\mu\nu}. \quad (2.27)$$

From (2.23) to (2.24) one uses that the variation of a Christoffel symbol $\Gamma_{\mu\nu}^\gamma$ transforms like a tensor, i.e., $\partial_\gamma (\delta \Gamma_{\mu\nu}^\gamma) = \nabla_\gamma (\delta \Gamma_{\mu\nu}^\gamma)$, where ∇_γ is a covariant derivative. The Ricci tensor is denoted as $R_{\mu\nu}$. Inserting everything into (2.20) one arrives at

$$\delta S = \frac{1}{16\pi G} \int d^4x \frac{-g_{\mu\nu}}{2} \sqrt{-g} [R + f(R)] \delta g^{\mu\nu} + \sqrt{-g} [1 + F(R)] \delta R + \delta S_M(g_{\mu\nu}, \phi), \quad (2.28)$$

$$= \frac{1}{16\pi G} \int d^4x \left\{ \frac{-g_{\mu\nu}}{2} [R + f(R)] + [1 + F(R)] R_{\mu\nu} \right\} \sqrt{-g} \delta g^{\mu\nu} + \frac{1}{16\pi G} \int d^4x \sqrt{-g} [1 + F(R)] \nabla_\gamma W^\gamma + \delta S_M(g_{\mu\nu}, \phi). \quad (2.29)$$

Let's focus on the term containing $\nabla_\gamma W^\gamma$. Using the chain rule one obtains

$$\begin{aligned} \frac{1}{16\pi G} \int d^4x \sqrt{-g} [1 + F(R)] \nabla_\gamma W^\gamma &= -\frac{1}{16\pi G} \int d^4x \sqrt{-g} \nabla_\gamma F(R) W^\gamma \\ &+ \frac{1}{16\pi G} \int d^4x \sqrt{-g} \nabla_\gamma \{ [1 + F(R)] W^\gamma \}. \end{aligned} \quad (2.30)$$

2 Theory

Varying the metric only inside the integration domain, the second line of (2.30) vanishes due to Gauss' theorem. In order to bring the remaining term to an appropriate form, the variation of the connection is needed. For brevity, I will use $\nabla_\mu x_\nu \equiv x_{\nu;\mu}$ and $\partial_\mu x_\nu \equiv x_{\nu,\mu}$ for the covariant and the partial derivative, respectively.

$$\delta\Gamma_{\mu\nu}^\gamma = \delta(g^{\gamma\alpha}\Gamma_{\mu\nu\alpha}) \quad (2.31)$$

$$= (\delta g^{\gamma\alpha})\Gamma_{\mu\nu\alpha} + \frac{1}{2}g^{\gamma\alpha}(\delta g_{\mu\alpha;\nu} + \delta g_{\nu\alpha;\mu} - \delta g_{\mu\nu;\alpha}) \quad (2.32)$$

$$= \frac{1}{2}g^{\gamma\alpha}(\delta g_{\mu\alpha;\nu} + \delta g_{\nu\alpha;\mu} - \delta g_{\mu\nu;\alpha}). \quad (2.33)$$

Continuing to calculate (2.30) one arrives at

$$\begin{aligned} & \frac{1}{16\pi G} \int d^4x \sqrt{-g} W^\gamma \nabla_\gamma F(R) \\ &= \frac{1}{16\pi G} \int d^4x \sqrt{-g} \left[g^{\mu\nu} \delta\Gamma_{\mu\nu}^\gamma - g^{\mu\gamma} \delta\Gamma_{\mu\nu}^\nu \right] \nabla_\gamma F(R) \end{aligned} \quad (2.34)$$

$$\begin{aligned} &= \frac{1}{16\pi G} \int d^4x \sqrt{-g} \frac{1}{2} \left[g^{\mu\nu} g^{\gamma\alpha} (\delta g_{\mu\alpha;\nu} + \delta g_{\nu\alpha;\mu} - \delta g_{\mu\nu;\alpha}) \right. \\ & \quad \left. - g^{\mu\gamma} g^{\nu\alpha} (\delta g_{\mu\alpha;\nu} + \delta g_{\nu\alpha;\mu} - \delta g_{\mu\nu;\alpha}) \right] \nabla_\gamma F(R) \end{aligned} \quad (2.35)$$

$$= \frac{1}{16\pi G} \int d^4x \sqrt{-g} \left[g^{\mu\nu} g^{\gamma\alpha} (\delta g_{\nu\alpha;\mu} - \delta g_{\mu\nu;\alpha}) \right] \nabla_\gamma F(R) \quad (2.36)$$

$$= \frac{1}{16\pi G} \int d^4x \sqrt{-g} \left[(\nabla_\mu \delta g^{\mu\gamma}) - (\nabla^\gamma g_{\mu\nu} \delta g^{\mu\nu}) \right] \nabla_\gamma F(R) \quad (2.37)$$

$$= \frac{-1}{16\pi G} \int d^4x \sqrt{-g} \left[\nabla_\mu \nabla_\nu F(R) - g_{\mu\nu} \square F(R) \right] \delta g^{\mu\nu}. \quad (2.38)$$

In the last step, Gauss' theorem was used again. As above, the metric is only varied inside the integration domain requiring the surface terms to vanish.

Finally, the variation of the matter action is commonly expressed in terms of the energy-momentum tensor $T_{\mu\nu}$

$$T_{\mu\nu} = -\frac{2}{\sqrt{-g}} \frac{\partial S_M}{\partial g^{\mu\nu}} \quad \Rightarrow \quad \delta S_M = -\frac{\sqrt{-g}}{2} T_{\mu\nu} \delta g^{\mu\nu} \quad (2.39)$$

Plugging (2.38) and (2.39) into (2.29) leads to

$$\begin{aligned} 0 = \delta S = \frac{1}{16\pi G} \int d^4x \delta g^{\mu\nu} \sqrt{-g} \left\{ -\frac{g_{\mu\nu}}{2} [R + f(R)] + [1 + F(R)] R_{\mu\nu} \right. \\ \left. - \nabla_\mu \nabla_\nu F(R) + g_{\mu\nu} \square F(R) - 8\pi G T_{\mu\nu} \right\}. \end{aligned} \quad (2.40)$$

Substituting the Einstein tensor $G_{\mu\nu} = R_{\mu\nu} - \frac{R}{2}g_{\mu\nu}$ and requiring $\sqrt{-g} \neq 0$ one arrives at the field equations for $f(R)$ -gravity, the *Modified Einstein Equations*

$$G_{\mu\nu} - \frac{g_{\mu\nu}}{2} f(R) + F(R) R_{\mu\nu} - \nabla_\mu \nabla_\nu F(R) + g_{\mu\nu} \square F(R) = 8\pi G T_{\mu\nu}. \quad (2.41)$$

If in contrast the Palatini formalism is applied and the action is varied with respect to both the metric and an independent connection the resulting field equations are different. One important assumption which has to be made in order to derive the field equations is, that the matter action does only depend on the metric and matter fields and not on the connection. Starting out with the same action (2.19) one arrives at (Sotiriou & Faraoni, 2010)

$$[F(R) + 1] \frac{1}{2} (R_{\mu\nu} + R_{\nu\mu}) - \frac{1}{2} [f(R) + R] g_{\mu\nu} = 8\pi G T_{\mu\nu} \quad (2.42)$$

$$\tilde{\nabla}_\lambda \{ \sqrt{-g} [F(R) + 1] g^{\mu\nu} \} = 0. \quad (2.43)$$

Note that the covariant derivative $\tilde{\nabla}_\lambda$ and $R_{\mu\nu}$ are defined with respect to the independent connection in (2.42) and (2.43).

It is obvious that both the Modified Einstein equations obtained from the metric formalism and the field equations of Palatini $f(R)$ -gravity recover GR in the case $f(R) = 0$. In the following I will nevertheless only consider metric $f(R)$ -gravity.

2.3.2 $f(R)$ -gravity formulated as a scalar tensor theory

$f(R)$ -gravity can be easily rewritten as a scalar tensor theory (Brax *et al.*, 2008). Let me start by defining a field ϕ as

$$e^{-\frac{2\beta\phi}{M_{\text{pl}}}} = F + 1, \quad (2.44)$$

where $\beta = \sqrt{1/6}$. Switching to the so called Einstein frame metric, which is defined as

$$\tilde{g}_{\mu\nu} = e^{-\frac{2\beta\phi}{M_{\text{pl}}}} g_{\mu\nu}, \quad (2.45)$$

the action for $f(R)$ -gravity (2.19) becomes

$$S = \int d^4x \sqrt{-\tilde{g}} \left[\frac{M_{\text{pl}}^2}{2} \tilde{R} - \frac{1}{2} \tilde{g}^{\mu\nu} \nabla_\mu \phi \nabla_\nu \phi - V(\phi) + \tilde{\mathcal{L}}_m \right]. \quad (2.46)$$

In the language of section 2.2.1 the above definition of $\tilde{g}_{\mu\nu}$ corresponds to

$$A^2(\phi) = e^{-\frac{2\beta\phi}{M_{\text{pl}}}}. \quad (2.47)$$

The potential of the field ϕ , $V(\phi)$ is given by

$$V(\phi) = \frac{M_{\text{pl}}^2 [R f_R - f(R)]}{2(f_R + 1)^2}. \quad (2.48)$$

All symbols with a $\tilde{}$ are defined with respect to the Einstein frame metric $\tilde{g}_{\mu\nu}$. The field equations then read (Brax *et al.*, 2008)

$$\tilde{G}_{\mu\nu} = \tilde{R}_{\mu\nu} - \frac{1}{2}\tilde{R}\tilde{g}_{\mu\nu} \quad (2.49)$$

$$= \frac{1}{M_{\text{Pl}}^2} \left\{ \tilde{\nabla}_\mu \phi \tilde{\nabla}_\nu \phi - \tilde{g}_{m n} \left[\frac{1}{2}(\tilde{\nabla} \phi)^2 + V \phi \right] + T_{\mu\nu} \right\}, \quad (2.50)$$

$$\tilde{\square} \phi = V'(\phi) - \frac{\beta}{M_{\text{Pl}}}. \quad (2.51)$$

These equations describe exactly the same physics as the Modified Einstein equations. For some applications they are nevertheless easier to handle.

2.3.3 The Newtonian limit of $f(R)$ -gravity

In the context of cosmological simulations the Newtonian limit of GR is considered to be sufficient as the GR effects are negligibly small (See e.g. Adamek *et al.*, 2016, for a comparison between cosmological simulations carried out including higher order GR terms and simulations adopting the weak field limit). It was also shown that relativistic effects in $f(R)$ -gravity due to the finite speed of light and back-reaction do not lead to considerable changes in the laws of physics in the Newtonian limit (Noller *et al.*, 2014; Sawicki & Bellini, 2015). The quasi-static weak field limit is therefore assumed in basically all cosmological simulation codes for $f(R)$ -gravity. Let me now derive an equivalent to the Poisson equation for $f(R)$ -gravity and an equation for the scalar degree of freedom $f_R = F(R)$ in the Newtonian limit.

Starting out with the Modified Einstein equations and taking their trace results in

$$-R - 2f(R) + RF(R) + 3\square F(R) = 8\pi G T. \quad (2.52)$$

Splitting of the background terms, assuming a pressure-less ideal fluid for the matter term and a reasonable $f(R)$ -model with $|F| \ll 1$ (this holds for all models satisfying current constraints) one arrives at

$$-\delta R - 2\delta f(R) + 3\square F(R) = 8\pi G \delta \rho. \quad (2.53)$$

In a quasi-static situation the time derivatives can be neglected. Using $\delta f(R) = F(R)\delta R \ll \delta R$ one arrives at an expression for the scalar degree of freedom

$$\nabla^2 F = \frac{1}{3}[\delta R - 8\pi G \delta \rho], \quad (2.54)$$

where the ∇^2 operator includes spatial derivatives only.

To derive an expression for the gravitational forces, the metric needs to be specified. Adopting conformal Newtonian gauge, the line element reads

$$ds^2 = a(\eta)^2 [-(1 + 2\Phi)d\eta^2 + (1 - 2\Psi)d\mathbf{x}^2], \quad (2.55)$$

where η is the conformal time which is related to physical time by $a(\eta)d\eta = dt$. Considering the 00-element of (2.41) and only weak fields $\Phi \ll 1 \Rightarrow g_{00} \approx -1$ gives

$$R_{00} + \frac{R}{2} + \frac{f}{2} - \nabla_0 \nabla_0 F(R) - g^{\alpha\gamma} \nabla_\alpha \nabla_\gamma F(R) = 8\pi G T_{00}, \quad (2.56)$$

where the $f/2$ term can be neglected for the same reasons as above. Dropping the background terms again in inserting (2.54) leads to

$$\delta R_{00} = \frac{16\pi G}{3} \delta\rho - \frac{1}{6} \delta R. \quad (2.57)$$

What remains is to calculate the 00-element of the Ricci tensor. For brevity, I will use $a' \equiv \partial a / \partial \eta$, $a_{\mu,\nu} = \partial a_\mu / \partial x_\nu$. Latin indices (i, j, k, \dots) denote spatial coordinates in the following, Greek indices all four space-time coordinates. The time-time component of the Ricci tensor is given by

$$R_{00} = \Gamma_{00,\alpha}^\alpha - \Gamma_{\alpha 0,0}^\alpha + \Gamma_{\alpha\gamma}^\alpha \Gamma_{00}^\gamma - \Gamma_{0\gamma}^\alpha \Gamma_{\alpha 0}^\gamma \quad (2.58)$$

$$= \Gamma_{00,i}^i - \Gamma_{i0,0}^i + \Gamma_{i0}^i \Gamma_{00}^0 + \Gamma_{ij}^i \Gamma_{00}^j - \Gamma_{00}^i \Gamma_{i0}^0 - \Gamma_{0j}^i \Gamma_{i0}^j \quad (2.59)$$

$$= \nabla_c^2 \Phi - (\mathcal{H} - \Psi')' + 3(\mathcal{H} - \Psi')(\mathcal{H} + \Phi') \\ - \nabla_c \Psi \nabla_c \Phi - (\nabla_c \Phi)^2 - 3(\mathcal{H} - \Psi')^2, \quad (2.60)$$

where ∇_c denotes the gradient with respect to the spatial part of the conformal coordinates and $\mathcal{H} \equiv \frac{a'}{a}$. The quasi static assumption allows us to neglect all time derivatives and since Ψ and Φ are weak fields, all second order terms in the fields can be dropped as well. Thus

$$\delta R_{00} = \nabla_c^2 \delta\Phi. \quad (2.61)$$

In order to transform equation (2.61) back to physical coordinates, the Ricci tensor translates as $R_{\mu\nu}^c = a^2 R_{\mu\nu}$. Since $\nabla = \frac{1}{a} \nabla_c$ the a -factors cancel and one gets

$$\delta R_{00} = \nabla^2 \delta\Phi, \quad (2.62)$$

in physical coordinates. Combining this result with (2.57) and noting that Φ is the Newtonian potential ϕ in the weak field limit leads to the *Modified Poisson equation*

$$\nabla^2 \phi = \frac{16\pi G}{3} \delta\rho - \frac{1}{6} \delta R. \quad (2.63)$$

An expression for the so called fifth force, the additional gravitational force due to the modifications to gravity, can be obtained by combining the Modified Poisson equation with (2.54)

$$\nabla^2 \phi = 4\pi G \delta\rho - \frac{1}{2} \nabla^2 F(R). \quad (2.64)$$

Subtracting the standard gravity part and integrating once leads to

$$a_{\text{Fifth force}} = -\nabla \phi_{f(R)} = \frac{1}{2} \nabla F(R). \quad (2.65)$$

The fifth force can thus simply be calculated from the gradient of the scalar field.

2.3.4 Chameleon screening in $f(R)$ -gravity

As already mentioned above, GR is tested to remarkably high precision in high density regions like the solar system (Will, 2014). Therefore all modified gravity theories need a screening mechanism to recover GR in these environments. For $f(R)$ -gravity this is achieved by the chameleon mechanism. Its basic operation modes can already be seen from the Modified Poisson equation. In a low density environment, where the gravitational potential is shallow, the curvature will be small and thus $\delta R \approx 0$. Neglecting the term containing δR in (2.63) it is obvious that the gravitational forces will be enhanced by a factor of $4/3$ compared to standard gravity or – in other words – screening is inactive.

Considering a high density environment, the curvature will be comparatively large: $\frac{1}{3}\delta R \gg |\nabla^2 F|$. (2.54) consequently reduces to

$$\delta R \approx 8\pi G \delta\rho. \quad (2.66)$$

Using this approximation in (2.63) reproduces the Poisson equation of standard Newtonian gravity:

$$\nabla^2 \phi = 4\pi G \delta\rho, \quad (2.67)$$

showing that the chameleon screening mechanism screens the modifications to GR in high density environments.

2.3.5 $f(R)$ cosmology

The evolution of the large scale background can be described by an equivalent to Friedmann's equations. In order to derive those Modified Friedman equations, let me assume a FRW metric for the large scale structure of the Universe (see e.g. Sotiriou & Faraoni, 2010, for a discussion on why this is a valid assumption). Furthermore considering a spatially flat background with $K = 0$ gives

$$ds^2 = -c^2 dt^2 + a^2(t) [dw^2 + w^2 d\Omega^2]. \quad (2.68)$$

As for standard gravity, the Ricci scalar is then given by

$$R = 12H^2 + 6\dot{H}. \quad (2.69)$$

In order to obtain an equation for the Hubble constant $H = \frac{\dot{a}}{a}$ ($\dot{a} \equiv \partial_t a$) I will start out with the 00-element of the Modified Einstein equations

$$R_{00} + \frac{R + f}{2} + FR_{00} - \nabla_0 \nabla_0 F - \square F = 8\pi G T_{00}. \quad (2.70)$$

The covariant derivatives of F which is assumed to depend on time only on sufficiently large scales are now given by

$$\square F = -\nabla_0 \nabla_0 F + \frac{1}{a^2} \sum_i \nabla_i \nabla_i F, \quad (2.71)$$

$$\nabla_\mu F = \partial_\mu F = \dot{F} \delta_{\mu 0}, \quad (2.72)$$

$$\nabla_\nu \nabla_\mu F = \delta_{\mu 0} \delta_{\nu 0} \ddot{F} - \Gamma_{\nu\mu}^0 \dot{F}. \quad (2.73)$$

With $\Gamma_{00}^0 = 0$ and $\Gamma_{ij}^0 = \dot{a}a\delta_{ij}$ this leads to

$$\nabla_0\nabla_0 F = \ddot{F} \quad \text{and} \quad \nabla_i\nabla_j F = -\dot{a}a\delta_{ij}\dot{F}. \quad (2.74)$$

Assuming that cosmic matter behaves like an ideal fluid with the four-velocity u_μ

$$T^{\mu\nu} = (\rho + P)u^\mu u^\nu + Pg^{\mu\nu}, \quad (2.75)$$

and plugging everything into (2.70) one obtains

$$-\frac{3\ddot{a}}{a}(F+1) + \frac{R+f}{2} + \frac{3}{a^2}\dot{a}a\dot{F} = 8\pi G\rho, \quad (2.76)$$

$$\Leftrightarrow 3\left[H^2 - \frac{R}{6}\right](F+1) + \frac{R+f}{2} + 3H\dot{F} = 8\pi G\rho, \quad (2.77)$$

$$\Leftrightarrow (F+1)H^2 = \frac{8\pi G\rho}{3} + \frac{RF-f-6H\dot{F}}{6}, \quad (2.78)$$

which is the first Friedman equation for $f(R)$ -gravity. The second one can be derived from the trace of the Modified Einstein equation (2.52)

$$-(F+1)\left[12H^2 + 6\dot{H}\right] + 2(RF-f) - 3\ddot{F} - 9H\dot{F} = 8\pi G(3P - \rho). \quad (2.79)$$

Inserting (2.82) for the density yields

$$-(F+1)\left[3H^2 + 2\dot{H}\right] + \frac{1}{2}(RF-f) - \ddot{F} - 2H\dot{F} = 8\pi GP \quad (2.80)$$

Rewriting (2.78) and (2.80) one obtains the *Modified Friedman equations*. The $f(R)$ -gravity contributions can be viewed as an effective density and pressure, ρ_{eff} and P_{eff}

$$H^2 = \frac{1}{3(1+F)} \left[8\pi G\rho + \frac{RF-f-6H\dot{F}}{2} \right] \quad (2.81)$$

$$= \frac{8\pi G\rho}{3(1+F)} + \frac{\rho_{\text{eff}}}{3}, \quad (2.82)$$

$$3H^2 + 2\dot{H} = \frac{-1}{(1+F)} \left[8\pi GP - \frac{1}{2}(RF-f) + \ddot{F} + 2H\dot{F} \right] \quad (2.83)$$

$$= -\frac{8\pi GP}{(1+F)} - P_{\text{eff}}. \quad (2.84)$$

Using the above result one can calculate the effective equation of state parameter for $f(R)$ -gravity in vacuum,

$$w_{\text{eff}} = \frac{P_{\text{eff}}}{\rho_{\text{eff}}} = \frac{-(RF-f) + 2\ddot{F} + 4H\dot{F}}{RF-f-6H\dot{F}}. \quad (2.85)$$

It is easy to see that for a Λ CDM Universe, where $f = -2\Lambda$ this equation returns the well known standard model value of $w_{\text{eff}} = -1$. In order to reproduce a Λ CDM expansion history, the following equation must hold for the $f(R)$ theory of choice

$$\frac{F'}{F''} = \frac{\dot{R}^2}{H\dot{R} - \ddot{R}}, \quad (2.86)$$

where $F' = \partial_R^2 f$ and $F'' = \partial_R^3 f$.

2.3.6 The functional form of $f(R)$

In order to compute gravitational forces in $f(R)$ gravity, e.g. to solve equations (2.63) and (2.54) one has to pick a certain $f(R)$ -model or – in other words – choose a particular function $f(R)$. The numerical form of this function will determine the behaviour of the cosmological model. Theories of $f(R)$ -gravity can account for inflation if one picks e.g. $f(R) = \alpha R^2$ (De Felice & Tsujikawa, 2010) or for the late time accelerated expansion of the Universe. Examples are $f(R) \propto \frac{1}{R}$ (Vollick, 2003) or the Starobinski model

$$f(R) = aM^2 \left[\left(1 + \frac{R^2}{M^4} \right)^{-\frac{\alpha}{2}} - 1 \right]. \quad (2.87)$$

The model I will consider in this work was proposed by Hu & Sawicki (2007). It is designed to account for the late time acceleration of the expansion of the Universe. It is given by

$$f(R) = -m^2 \frac{c_1 \left(\frac{R}{m^2}\right)^n}{1 + c_2 \left(\frac{R}{m^2}\right)^n}, \quad (2.88)$$

where $m^2 = H_0^2 \Omega_m$. The model has three constants n , c_1 , and c_2 which control its behaviour. The constant n can in principle be chosen arbitrarily but is most commonly set to $n = 1$. I will adopt this convention throughout this work. The two remaining constants can be used to control the background evolution of the universe in the theory and to adjust the onset threshold for chameleon screening. In order to be consistent with current observations, I require the model to have an expansion history which is similar to that of a Λ CDM universe (Planck Collaboration *et al.*, 2016a), or $w_{\text{eff}} = -1$. Calculating the derivatives of $f(R)$ gives

$$f_R = F = -c_1 n \frac{\left(\frac{R}{m^2}\right)^{n-1}}{\left[1 + c_2 \left(\frac{R}{m^2}\right)^n\right]^2} \quad (2.89)$$

$$\approx -\frac{c_1 n}{c_2^2} \left(\frac{m^2}{R}\right)^{n+1}, \quad (2.90)$$

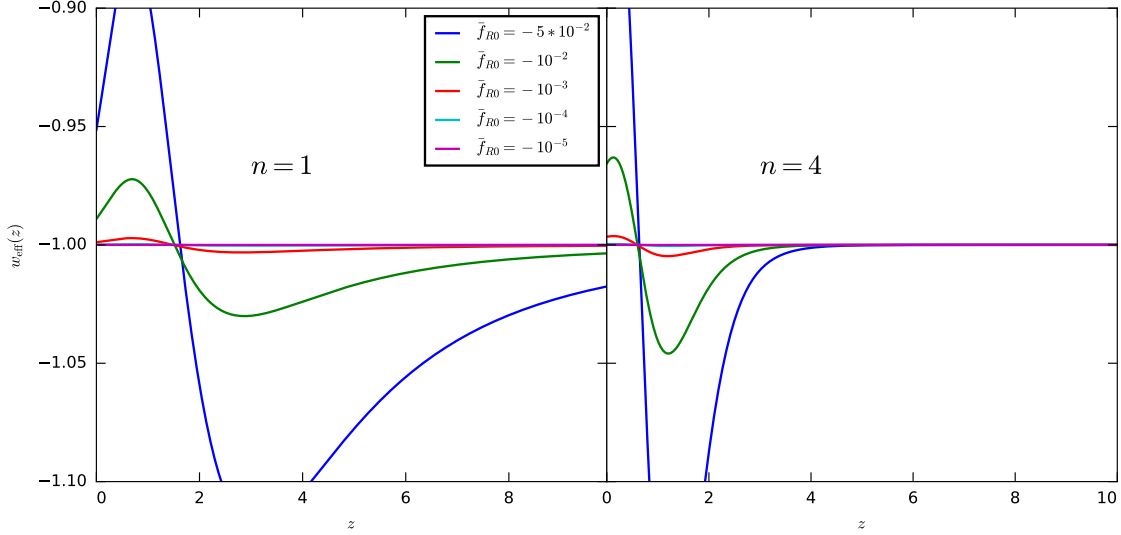


Figure 2.2: The redshift evolution of the effective equation of state parameter w_{eff} for Hu & Sawicki (2007) $f(R)$ -gravity and different values for the background field. In the *left panel* a model with $n = 1$ is shown while the *right panel* displays the same data for $n = 4$.

where (2.90) holds if $1 \ll c_2 \left(\frac{R}{m^2}\right)^n$.

$$f_{RR} = F' = -\frac{c_1 n (n-1) \left(\frac{R}{m^2}\right)^{n-2} - (n+1)c_2 \left(\frac{R}{m^2}\right)^{2n-2}}{m^2 \left[1 + c_2 \left(\frac{R}{m^2}\right)^n\right]^3}, \quad (2.91)$$

$$f_{RRR} = F'' = -c_1 m^2 n \left(\frac{R}{m^2}\right)^n \times \frac{2 \left(1 + c_2 \left(\frac{R}{m^2}\right)^n\right)^2 + 3n \left(-1 + c_2^2 \left(\frac{R}{m^2}\right)^{2n}\right) + n^2 \left(1 - 4c_2 \left(\frac{R}{m^2}\right)^n + c_2^2 \left(\frac{R}{m^2}\right)^{2n}\right)}{R^3 \left(1 + c_2 \left(\frac{R}{m^2}\right)^n\right)^4}. \quad (2.92)$$

Evaluating the time derivatives in (2.85) and inserting the derivatives of $f(R)$ leads to

$$w_{\text{eff}} = -\frac{Rf_R - f - 2(f_{RRR}\dot{R}^2 + f_{RR}\ddot{R}) - 4Hf_{RR}\dot{R}}{Rf_R - f - 6Hf_{RR}\dot{R}}. \quad (2.93)$$

As one can see from Figure 2.2, the model obeys a phantom behaviour of the background evolution for $f(R)$ -gravity models with a large (negative) value for f_{R0} . For viable models with $|\tilde{f}_{R0}| \leq 10^{-4}$, the theory nevertheless has a background evolution parameter which is hardly distinguishable from the Λ CDM value of $w_{\text{eff}} = -1$.

In the limit (2.90) one can now derive a simple expression for the time evolution

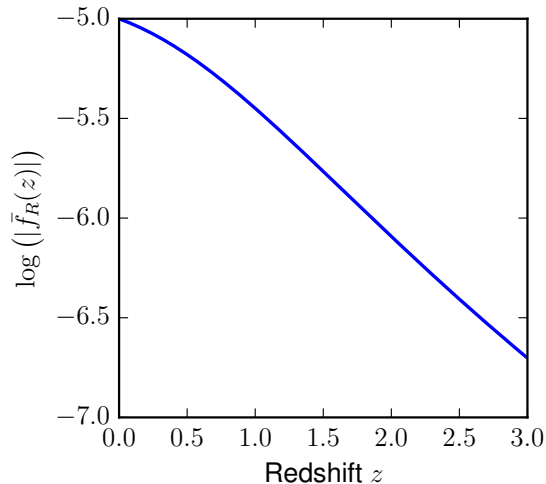


Figure 2.3: The redshift evolution of the background field in Hu & Sawicki (2007) $f(R)$ -gravity for $|\bar{f}_{R0}| = 10^{-5}$.

of the background scalar field

$$\bar{f}_R(a) = \bar{f}_{R0} \left[\frac{\bar{R}_0}{\bar{R}(a)} \right], \quad (2.94)$$

and

$$\delta R = \bar{R}(a) \left[\sqrt{\frac{\bar{f}_R(a)}{f_R}} - 1 \right]. \quad (2.95)$$

The dependence of \bar{f}_R on redshift is shown in Figure 2.3. As one can see from the plot, the background value of f_R drops with growing redshift. At redshift $z = 1.5$, a $|\bar{f}_{R0}| = 10^{-5}$ model will therefore behave like an $|\bar{f}_{R0}| = 10^{-6}$ model at redshift zero. The screening threshold will thus become lower at higher redshift resulting in weaker $f(R)$ effects at earlier times.

2.3.7 Current constraints on $f(R)$ -gravity

The current observational constraints on the Hu & Sawicki (2007) $f(R)$ model were obtained from measurements spanning a wide range of scales, reaching from Solar system and dwarf galaxy constraints at sub parsec scales to Gpc scales for the CMB constraints (Terukina *et al.*, 2014). The most stringent restrictions on \bar{f}_{R0} come nevertheless from local measurements. Requiring that the Solar system is screened within the Milky way leads to a maximum background parameter of $|\bar{f}_{R0}| = 10^{-6}$ (Hu & Sawicki, 2007; Lombriser *et al.*, 2014; Arnold *et al.*, 2016). The other, even more stringent small scale constraint is obtained from distance indicators in dwarf galaxies (Jain *et al.*, 2013). Due to their low mass, these objects are usually unscreened

(unless they live in a high density environment), maximizing the $f(R)$ -effects. By comparison to more massive screened galaxies, one can derive a constraint of $|\bar{f}_{R0}| < 5 \times 10^{-7}$ at 95% confidence level.

On the large scale side of the constraints, the most stringent results come from observations of the Coma cluster. Comparing hydrostatic mass measurements (these are sensitive to $f(R)$ -gravity in unscreened regions, Arnold *et al.*, 2014) to the weak lensing mass of the object (which is the same in both GR and $f(R)$ -gravity) one can derive an upper bound of $|\bar{f}_{R0}| < 6 \times 10^{-5}$ (Terukina *et al.*, 2014). At the same scales, measurements of cluster density profiles lead to a constraint of $|\bar{f}_{R0}| < 3.5 \times 10^{-3}$ (Lombriser *et al.*, 2012b). Through a comparison of cluster abundance in simulations with cosmological data, one obtains an upper bound of $|\bar{f}_{R0}| < 1.3 \times 10^{-4}$ at a 2σ level (Schmidt *et al.*, 2009). Finally, Planck data on the CMB leads to a constraint of $|\bar{f}_{R0}| < 10^{-2}$ (Hu *et al.*, 2013).

Summarizing one can say that the strongest currently allowed $f(R)$ model is $|\bar{f}_{R0}| = 10^{-6}$. It is nevertheless sometimes useful to consider stronger modifications to GR as a toy model in order to find out how $f(R)$ -gravity acts on certain observables in general.

2.3.8 Screening in spherically symmetric objects

¹ It is in general not possible to analytically describe the scalar field and the fifth forces for a complex density field. If the geometry of the density field is on the other hand reasonably simple, such analytical solutions are well possible. In the following I will derive an expression for the screening radius and the fifth force inside a spherically symmetric over-density, following Davis *et al.* (2012); Sakstein (2013). In order to do so, it is easier to work in the frame of $f(R)$ as a scalar-tensor theory as described in Section 2.3.2.

Consider a spherical over-density of radius R and density profile $\rho(r)$ which is embedded in a homogeneous background density ρ_0 . If at least part of the object is screened, there will be some screening radius r_s inside which the $f(R)$ modifications to GR are completely suppressed (Davis *et al.*, 2012). When approaching r_s from the outside, the ratio of fifth-to-GR force will monotonically drop from its background value to zero. The cases $r_s \geq R$ and $r_s = 0$ refer to the fully screened and unscreened situations, respectively (see Fig. 2.4).

In the scalar-tensor theory description of $f(R)$ -gravity, the Newtonian limit of the field equations (2.50) and (2.51) is given by

$$\nabla^2 \phi = \frac{\partial V}{\partial \phi} + \frac{\beta \rho}{M_{\text{pl}}}. \quad (2.96)$$

One now has to distinguish different cases. If the object is at least partially screened (top right panel in Fig. 2.4), the effective potential will reach its minimum

¹The results and parts of the text of this section have already been published in Arnold *et al.* (2016).

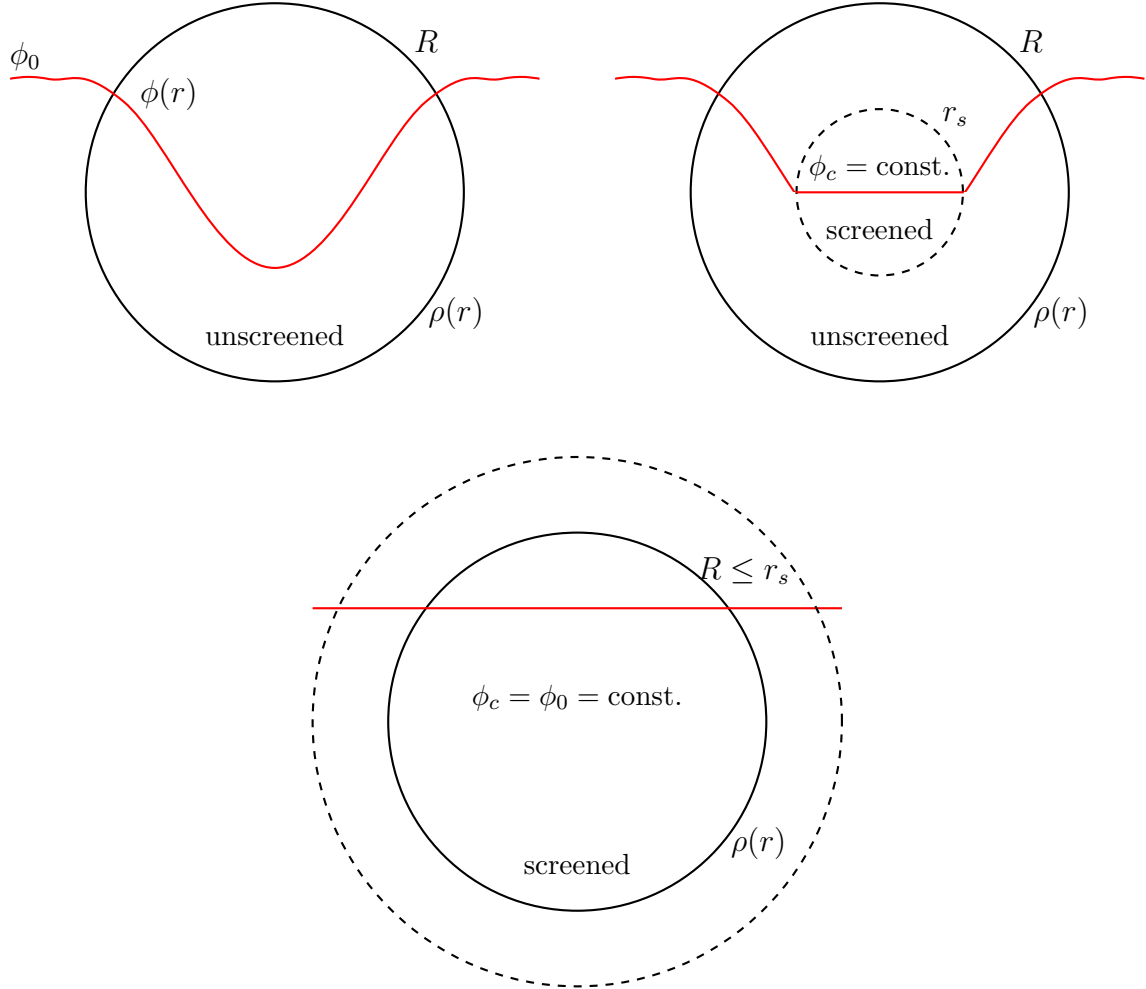


Figure 2.4: Sketch of the screening mechanism on the field ϕ in a spherical over-density $\rho(r)$ with outer radius R . The *top left panel* shows a completely unscreened case with the fifth force contribution $\mathbf{F}_5 \propto \nabla\phi$ present at all radii. In the *top right panel* a partially screened situation is sketched, where the field is constant inside a screening radius r_s . A completely screened case, where the screening radius exceeds the radius of the over-density is illustrated in the *lower panel*.

inside r_s and one has (Hui *et al.*, 2009)

$$\frac{\partial V}{\partial \phi} = -\frac{\beta \rho}{M_{\text{pl}}}. \quad (2.97)$$

In other words, the derivative of the field ϕ will be constant inside r_s , and since there are no sources, $\phi = \text{const}$. Far outside the sphere (for $r \gg R$), the field ϕ_0 is just given by the background value f_{R0} of the scalar degree of freedom. To obtain ϕ in the remaining region in between, i.e. in the partially screened shell of the sphere, one can linearize Eqn. (2.96) and express it in terms of perturbations of the background value $\delta\phi = \phi - \phi_0$,

$$\nabla^2 \delta\phi = \frac{\partial^2 V}{\partial \phi^2} \delta\phi + \frac{\beta \delta\rho}{M_{\text{pl}}}. \quad (2.98)$$

Writing the density in Eqn. (2.98) in terms of the Newtonian potential $\nabla^2 \Phi_N = 4\pi G\rho$, integrating twice, and re-substituting the Newtonian potential for a spherical over-density, $d\Phi_N/dr = GM(< r)/r^2$, one arrives at an expression for the fifth force for $r > r_s$ (Sakstein, 2013; Davis *et al.*, 2012):

$$F_5 = \alpha \frac{GM(< r)}{r^2} \left[1 - \frac{M(r_s)}{M(< r)} \right], \quad (2.99)$$

where $\alpha = 2\beta^2 = 1/3$ is the coupling strength of $f(R)$ gravity.

What remains to be done in order to obtain the fifth force is to estimate the screening radius r_s . It is implicitly given by the integral equation (Sakstein, 2013)

$$\frac{\phi_0}{2\beta M_{\text{pl}}} = 4\pi G \int_{r_s}^R r \rho(r) dr. \quad (2.100)$$

Equations (2.99) and (2.100) yield an estimate for the radius inside which the object is fully screened as well as the fifth force profile for objects which are roughly spherical (as the dark matter halos presented in Chapter 6). Given the density profile of a simulated halo, one can easily compute an approximate estimate for the fifth force and compare it to the simulation outcomes. The only remaining question is which radius one should choose for the outer boundary R , as in practice it is hard to judge where an halo exactly ends. In this work, I use r_{200} (the radius which encloses a sphere with a mean density of 200 times the critical density) as a natural choice for R .

Let us now assume that the density of the halo is given by a NFW-profile (Navarro *et al.*, 1997):

$$\rho(r) = \frac{\rho_{\text{crit}} \delta_c}{\left(\frac{r}{r_{\text{NFW}}}\right) \left(1 + \frac{r}{r_{\text{NFW}}}\right)^2}. \quad (2.101)$$

2 Theory

To avoid confusion with the screening radius r_s the scaling radius of the NFW-profile is denoted as r_{NFW} here. Inserting Eqn. (2.101) into (2.100), and solving for r_s gives

$$r_s = \frac{r_{\text{NFW}}}{\frac{1}{1+r_{200}/r_{\text{NFW}}} - \frac{3\ln(f_{R0}+1)}{8\pi G\rho_{\text{crit}}\delta_c r_{\text{NFW}}^2}} - r_{\text{NFW}}. \quad (2.102)$$

The scale introduced by the screening radius will obviously break the self-similarity of dark matter halos with equal concentration but different masses as known in the standard model of cosmology. Scaling both halo mass and f_{R0} such that the ratio r_s/r_{200} and the concentration parameter stay constant for different $f(R)$ models is nevertheless possible. This restores some kind of self-similarity in $f(R)$ gravity:

$$\left(\frac{M_1}{M_2}\right)^{\frac{2}{3}} = \frac{\ln(f_{R0_1} + 1)}{\ln(f_{R0_2} + 1)} \approx \frac{f_{R0_1}}{f_{R0_2}}, \quad (2.103)$$

where M denotes M_{200} and the subscripts 1 and 2 refer to the first and the second model/halo, respectively. As a cautionary remark it is important to say that this involves a scaling of f_{R0} and will therefore not work for a given fixed $f(R)$ model.

3 Numerics

3.1 Modified gravity simulations

There have been huge developments in the field of modified gravity numerical N-body simulations over the recent years. The theories most commonly studied in simulations are $f(R)$ -gravity, galileon gravity and the Symmetron model.

For the $f(R)$ -model, there are four efficient cosmological simulation codes which can be used for large scale simulations. Two of them, ECOSMOG (Li *et al.*, 2012) and ISIS (Llinares *et al.*, 2014a) are based on RAMSES (Teyssier, 2002), a cosmological hydrodynamical simulation code employing a grid based method with adaptive mesh refinement (AMR) and multigrid acceleration for the computation of both the gravitational forces and the hydrodynamical equations. ECOSMOG and ISIS use this grid to also solve the equations for the scalar field. MG-GADGET (Puchwein *et al.*, 2013) is a cosmological $f(R)$ -gravity simulation code which I used and further developed for the projects of this thesis. I also developed a modified gravity solver for the moving mesh code AREPO (Springel, 2010). The functionality of these two codes is described in detail below.

Numerical simulation studies of $f(R)$ -gravity include works on the matter power spectrum (Oyaizu, 2008; Li *et al.*, 2012, 2013c; Llinares *et al.*, 2014b; Puchwein *et al.*, 2013; Arnold *et al.*, 2015), the mass function of dark matter halos (Schmidt *et al.*, 2009; Ferraro *et al.*, 2011; Li & Hu, 2011; Zhao *et al.*, 2011), the velocity dispersions of halos (Schmidt, 2010; Lam *et al.*, 2012; Lombriser *et al.*, 2012a), cluster concentrations (Lombriser *et al.*, 2012a) as well as density profiles (Lombriser *et al.*, 2012b). Furthermore, the integrated Sachs-Wolfe effect (Cai *et al.*, 2014), redshift space distortions (Jennings *et al.*, 2012), the properties of voids (Zivick *et al.*, 2015), and the properties of semi-analytically modeled galaxy populations (Fontanot *et al.*, 2013) have been studied in $f(R)$ -gravity. Recently, hydrodynamical simulations have been used to study galaxy clusters and groups in $f(R)$ gravity (Arnold *et al.*, 2014), the Lyman- α forest (Arnold *et al.*, 2015, as a part of this thesis), and power spectra and density profiles (Hammami *et al.*, 2015). In addition, galaxy clusters (Corbett Moran *et al.*, 2014) and Milky Way sized halos (Arnold *et al.*, 2016, also part of this thesis) were simulated employing a zoomed simulation technique in order to obtain high resolution for the object but also cover large scale cosmological effects.

The Symmetron model has been studied using the ISIS code for both the quasi static (Llinares *et al.*, 2014b) and the non-static limit (Llinares & Mota, 2014). It was also used to study scalar waves applying a leapfrog solver to the field equations (Hagala *et al.*, 2016). Further simulations of the Symmetron model were carried out with ECOSMOG (Davis *et al.*, 2012). The ECOSMOG code was also used to simulate

cubic and quartic galileon models (Barreira *et al.*, 2013; Li *et al.*, 2013b) as well as the DGP model (Li *et al.*, 2013a).

In the following I will give an overview over the two cosmological simulation codes I used and developed for the projects of this thesis.

3.2 MG-GADGET

MODIFIED GRAVITY GADGET (MG-GADGET) is a modified gravity cosmological simulation code based on P-GADGET3. It essentially has all the functionalities of the base code with a modified gravity solver for the Hu & Sawicki (2007) $f(R)$ -gravity model on top. MG-GADGET is thus capable of performing both collision-less and hydrodynamical cosmological simulations but also zoomed simulations in $f(R)$ -gravity.

The sections below are structured as follows. I will first introduce the base code P-GADGET3, then describe the modified gravity module and finally explain how the local timestepping scheme of the code works.

3.2.1 P-GADGET3

P-GADGET3 is based on GADGET2 (Springel, 2005). It employs a Tree Particle-Mesh (PM) solver for the gravitational forces and an entropy based smoothed particle-hydrodynamics algorithm (Springel & Hernquist, 2002) to solve the hydrodynamical equations. The code is parallelized with MPI, making it applicable to very large cosmological simulations (see e.g. Schaye *et al.*, 2015).

The gravity solver of the code splits the gravitational forces into a long- and a short-range part, which are computed with a PM and a gravitational Oct-Tree algorithm, respectively. The advantage over a pure tree-based method is, that the force-split algorithm avoids extensive communication between different MPI-tasks which would compromise the scalability of the code for larger numbers of CPUs. P-GADGET3 can either be used with periodic boundary conditions in the simulation setup or with non-periodic boundaries through zero-padding in the PM-force calculation.

The tree in the short-range part of the gravity solver refines by particle number, i.e. each time a tree-node contains more than one particle, it is refined to between one and eight sub-nodes, depending on how many of the eight sub-cubes are populated by particles. Starting out from a top-node, which covers the whole simulation box, this procedure is recursively repeated until each tree node contains at most one particle (except for very close particle groups, which are distributed over the neighboring nodes). In the force calculation for each particle, the force of the center of mass of every ‘small-enough’ node on the particle is computed, i.e. only the monopoles of the multipole expansion of the node’s mass distribution are considered. If a node is ‘small-enough’ or has to be opened is decided through a relative opening criterion which estimates the force error and compares it to the particle’s acceleration in the

previous timestep (at the beginning of each simulation the force calculation has to be carried out using a geometric opening criterion once, as no previous forces are available).

For zoomed simulations, the forces are split into three parts, a periodic long range part (calculated with PM), a non-periodic intermediate range part for the zoomed region (calculated via non-periodic PM) and short range tree forces.

The time integration in P-GADGET3 is carried out with an adaptive timesteps using an operator split approach (Springel, 2005). The timestep for each particle is determined such that it is small enough to prevent too large acceleration changes from one force integration to another but as small as possible to avoid unnecessary force calculations which would slow down the code. The total simulation time T (e.g. from redshift $z = 127$ to 0) is split into $\Delta t_{\min} = T/2^{32}$ equally sized pieces. The allowed timesteps are then hierarchically grouped into levels, which differ by a factor of two in step size. The timestep size on level a is consequently given by $\Delta t_a = 2^a \Delta t_{\min}$. Depending on its acceleration (which is used as a proxy for the acceleration changes) a particle is then assigned to one of these levels. The hierarchy ensures that all particles end up exactly at the end of a simulation and that all particles on smaller timesteps $t_b < t_a$ are at the same integration time at the end of t_a .

The timestepping for the different parts of the gravity solver is carried out as follows. For the short range tree forces, each particle is assigned an individual timestep Δt_i as described above. The PM force calculation is done on a global timestep Δt_{PM} for all particles at once, based on a velocity criterion. The individual timesteps of the particles are not allowed to exceed this timestep.

3.2.2 The modified gravity solver

Cosmological simulations are usually carried out in the Newtonian limit of GR as the influence of back-reaction and the finite speed of light are negligible for those (Adamek *et al.*, 2016). The applicability of the quasi-static, weak field limit has also been questioned for $f(R)$ -gravity but the errors made due to this assumption were estimated to be very small on the scales of cosmological simulations (Sawicki & Bellini, 2015).

The equations which have to be solved by the code are consequently the modified Poisson equation (2.63) and the equation for the scalar degree of freedom (2.54). The problem with the former equation is that it is very non-linear due to the chameleon screening mechanism. A tree algorithm as it is used in the gravity solver of P-GADGET3 is therefore not applicable. To overcome this issue, the gravity tree of P-GADGET3 is used to construct an AMR grid on which equation (2.54) is solved iteratively. The grid is build as follows.

Each node of the gravity tree represents one grid cell. The AMR grid consequently refines to particle number as well, i.e. it has a finer resolution in high density regions. In order to avoid a too patchy structure on the finer levels of the grid, the tree is build in a slightly different manner compared to P-GADGET3. If a tree node is

3 Numerics

refined (which is the case if it contains more than one particle), all eight sub-nodes are constructed no matter if all of them are populated by particles or not. The refinement of the AMR grid is limited to a maximum level which can be set as a parameter for each simulation setup individually. The minimum refinement level of the grid is limited as well.

Solving (2.54) directly with an iterative Newton method would lead to very slow convergence due to its non-linearity. The code therefore solves for

$$u \equiv \ln \left(\frac{f_R}{\bar{f}_R(a)} \right), \quad (3.1)$$

a trick which was first applied in Oyaizu (2008). Rewriting equation (2.54) accordingly and using (2.95) gives

$$\nabla^2 e^u = -\frac{1}{3\bar{f}_R(a)} [\bar{R}(a) (1 - e^{-\frac{u}{2}}) + 8\pi G\delta\rho]. \quad (3.2)$$

Again following the method of Oyaizu (2008), (3.2) is discretised for a given cell size h by

$$(\nabla^2 e^u)_{ijk} = \frac{1}{h^2} \left\{ b_{i-jk} u_{i-1jk} + b_{i+jk} u_{i+1jk} - u_{ijk} (b_{i-jk} + b_{i+jk}) \right. \quad (3.3)$$

$$\left. + b_{ij-k} u_{ij-1k} + b_{ij+k} u_{ij+1k} - u_{ijk} (b_{ij-k} + b_{ij+k}) \right. \quad (3.4)$$

$$\left. + b_{ijk-} u_{ijk-1} + b_{ijk+} u_{ijk+1} - u_{ijk} (b_{ijk-} + b_{ijk+}) \right\}, \quad (3.5)$$

where

$$b_{i-jk} = \frac{e^{u_{i-1jk}} + e^{u_{ijk}}}{2} \quad b_{i+jk} = \frac{e^{u_{i+1jk}} + e^{u_{ijk}}}{2} \quad (3.6)$$

and accordingly for the other b terms. Defining

$$L_{ijk} = (\nabla^2 e^u)_{ijk} + \frac{1}{3\bar{f}_R(a)} \bar{R}(a) \left(1 - e^{-\frac{u_{ijk}}{2}} \right) \quad (3.7)$$

and

$$f_{ijk} = \frac{1}{3\bar{f}_R(a)} 8\pi G [\bar{\rho}(a) - \rho_{ijk}], \quad (3.8)$$

one can now write

$$L_{ijk} = f_{ijk} \quad (3.9)$$

instead of (3.2). This equation is now suitable to be solved with an iterative Gauss-Seidel scheme. A new field u^n is then obtained from the one of the previous iteration step $n-1$ via

$$u_{ijk}^n = u_{ijk}^{n-1} + \frac{f_{ijk} - L_{ijk}^{n-1}}{dL_{ijk}^{n-1}/du_{ijk}^{n-1}}. \quad (3.10)$$

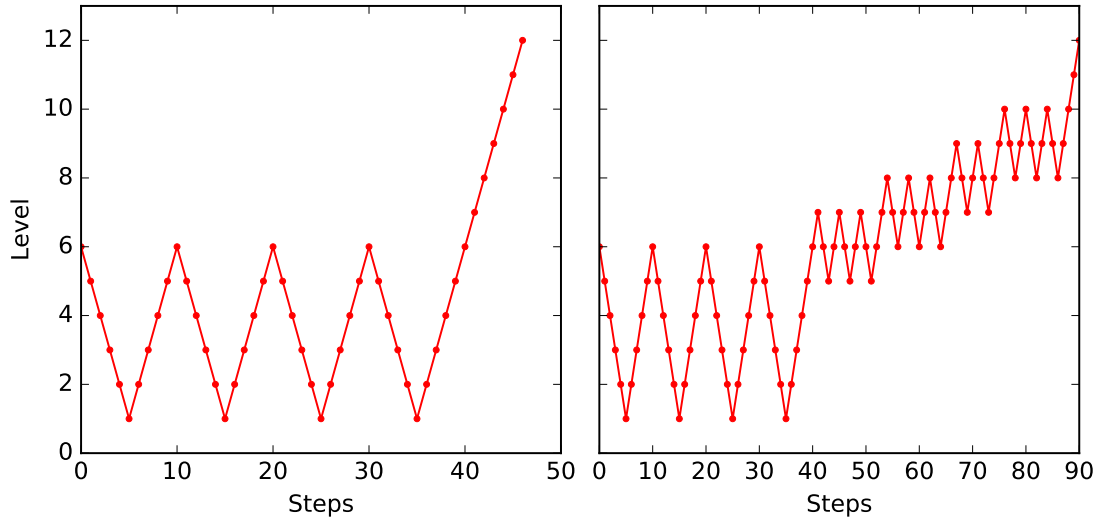


Figure 3.1: The iteration scheme for the multigrid solver in standard cosmological simulations (*left panel*) and for zoomed simulations (*right panel*). Each dot represents a number of red-black sweeps. In both cases $l_c = 6$ and the maximum grid level is 12.

In order to allow for efficient parallelization the iterations are carried out in a chess-board-pattern red-black sweep. As the information can at most "travel" one cell per iteration if one iterates on a fixed grid level, pure Gauss-Seidel solvers show very slow convergence. A significant speedup can be achieved through multigrid acceleration, where (not yet converged) solutions from the finer levels are mapped to coarser ones and back in a V-cycle manner in order to provide a good initial guess for the finest level which already contains the large scale information.

In MG-GADGET multigrid acceleration is applied in the following way. Starting out from an initial guess for the scalar field (obtained from the previous timestep) on the finest level which covers the complete simulation box (let's call it l_c here) the multigrid solver performs a few ($\approx 2 - 4$) red-black sweeps on l_c . The solution is then mapped to the next coarser level $l_c - 1$, i.e. a restriction is applied. On the $l_c - 1$ level, again a few red-black sweeps are carried out before the process is recursively repeated. The restriction operations end either on the coarsest AMR level (full V-cycle) or on a certain given level $l_c - n$ (W-cycle). After a number of iterations have been performed on the coarsest level the results are mapped back to the finer levels (i.e. prolongation). In order to not lose the small scale information which is already present on the finer level, only the difference of the solution on the coarse level to the initial value which was mapped is added to the finer level. The prolongations are applied until the initial level l_c is reached again. In MG-GADGET, full V-cycles are repeated on this level until the solution converges. The result is then prolonged to the next finer level. On this level the code either performs red-black sweeps until the solution converges (for normal cosmological setups) or a

series of W-cycles going up 2 – 3 levels each (zoom runs). This scheme for zoomed simulations differs from the procedure described in Puchwein *et al.* (2013), but shows a much better performance for this particular setup. The prolongations and sweeps are repeated until the finest AMR level is reached. The W-cycles are repeated until the second-last level is reached. Afterwards only red-black sweeps are performed for zoomed simulations.

The two different modes for multigrid acceleration are illustrated in Figure 3.1. The left panel shows the behaviour for a standard simulation setup and the right panel for zoom runs. Each dot represents a number of red black sweeps. Although the procedure for the zoomed simulations seems to involve more computations in the plot it is much faster than the standard scheme for zoom runs as the number of “iterations per dot” is significantly lower.

Once the value of the scalar field is known, there are two options to compute the modified gravity acceleration. The first method uses equation (2.65) to directly compute the acceleration from the gradient of the scalar field. This scheme is adopted by ECOSMOG and ISIS. It nevertheless requires a mapping of the scalar field gradients to the particle positions. The other option is to rewrite (2.63) in terms of an effective mass density ρ_{eff} which accounts for all $f(R)$ effects including the chameleon screening mechanism

$$\nabla^2\phi = 4\pi G(\delta\rho + \delta\rho_{\text{eff}}), \quad (3.11)$$

where

$$\delta\rho_{\text{eff}} = \frac{\delta\rho}{3} - \frac{\delta R}{24\pi G}. \quad (3.12)$$

δR is obtained through (2.95). The total gravitational force can be computed employing any standard gravity solver by adding the two mass densities. This is the way the forces were computed in the original version of MG-GADGET (Puchwein *et al.*, 2013) using the Tree-PM gravity solver. The local timestepping scheme for modified gravity which I implemented to make the code more efficient (described in detail below) nevertheless required to separate standard gravity and $f(R)$ forces. This is still possible with the effective mass scheme. Due to its linearity, equation (3.11) can be split into a “normal” and an effective mass part. The Tree-PM gravity solver of P-GADGET3 is then used to compute the accelerations separately.

It is not easily possible to couple local timestepping schemes for multigrid codes, e.g. the ones used in RAMSES (Teyssier, 2002), to the adaptive time integration in P-GADGET3. The original version of MG-GADGET therefore used equal timesteps for all particles. This method is computationally very costly, as a single particle in a region with very short dynamical timescales will trigger a full force computation for all simulation particles. Especially zoomed or hydrodynamical simulations with feedback require very short timesteps in certain regions and are therefore essentially impossible with global timestepping. To overcome this problem I developed a local timestepping scheme for MG-GADGET as a part of this thesis which is described in detail below.

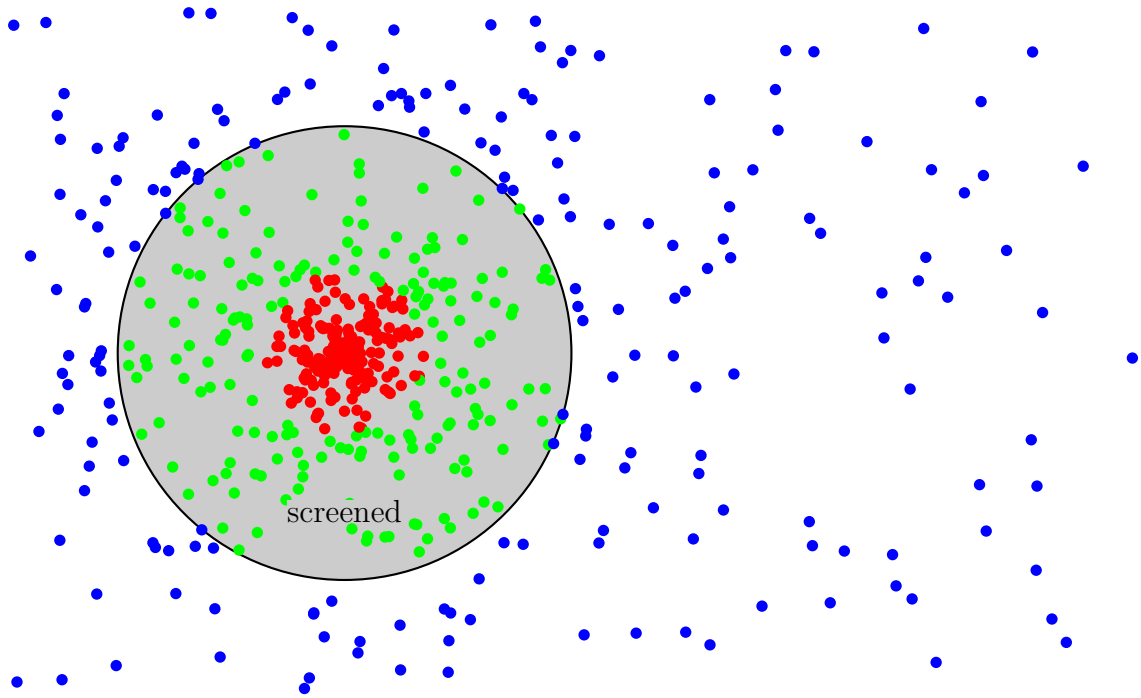


Figure 3.2: Illustration of the local timestepping scheme in MG-GADGET. The grey shaded region displays a screened high-density environment. Blue particles will be integrated on the global MG-PM timestep for all force parts. The green and the red particles are also integrated on this timestep for the PM- and modified gravity force, but are allowed to individually adjust their tree-gravity timestep to smaller values based on an acceleration criterion.

3.2.3 Local timestepping in MG-GADGET

¹ The local timestepping scheme of MG-GADGET is based on the fact that the regions with the shortest dynamical timescales are to a large degree screened in $f(R)$ -gravity. Short timesteps are mostly required in the center of over-dense regions like the centers of galaxies or galaxy clusters. These regions are high density environments and therefore, depending on the background field, screened to a certain degree by the chameleon mechanism. The modified gravity forces will consequently be very small (and change on large timescales) compared to the Newtonian gravity force. It is thus unnecessary to compute the modified gravity forces with the same high frequency as for standard gravity in these regions. For the local timestepping scheme which I implemented in MG-GADGET the two force components are therefore calculated separately and on individual timesteps.

The computation of the modified gravity forces and the very costly scalar field

¹The method and parts of the results of this section have already been published in Arnold *et al.* (2016)

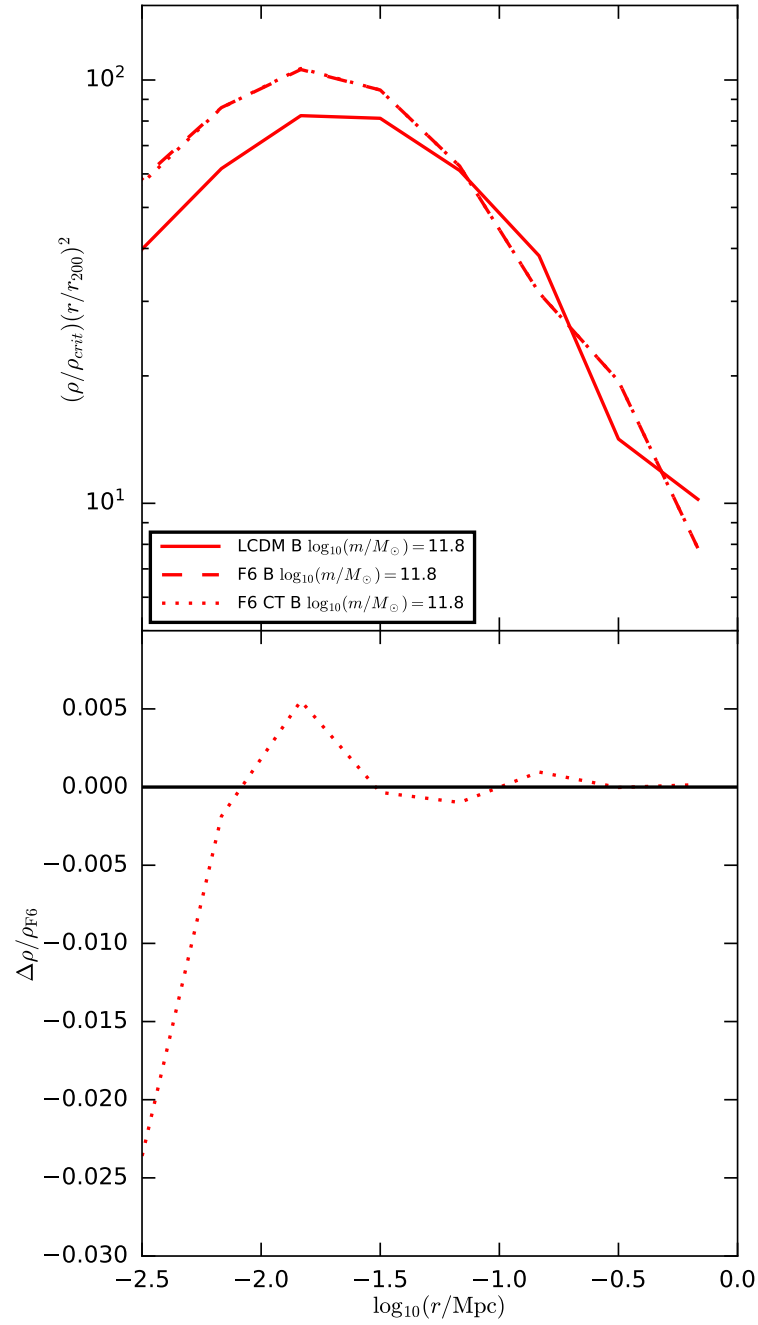


Figure 3.3: Local timestepping test: comparison between a simulation with the standard setup and one with a four times smaller MG-timestep (labeled CT). The *upper panel* shows density profiles of the central zoomed halo in a Λ CDM simulation and the two $f(R)$ -gravity runs with the different timesteps. The *lower panel* displays the relative difference in the density profiles between the two timestepping schemes.

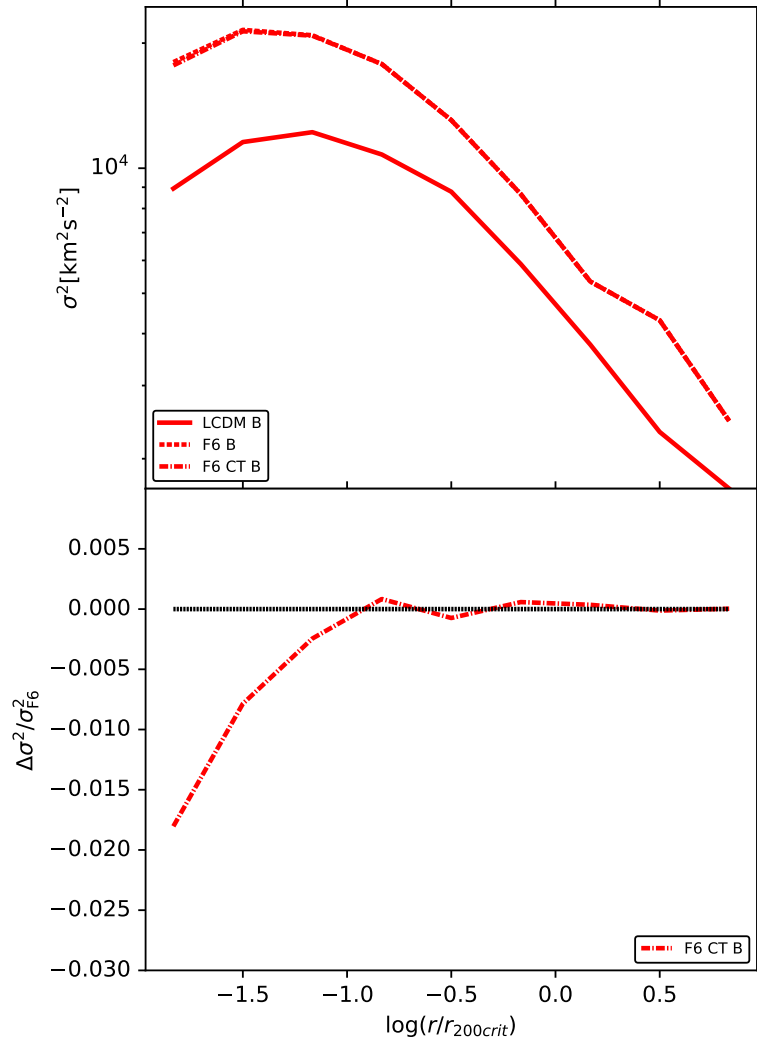


Figure 3.4: Same as Figure 3.3 but for the velocity dispersion profiles

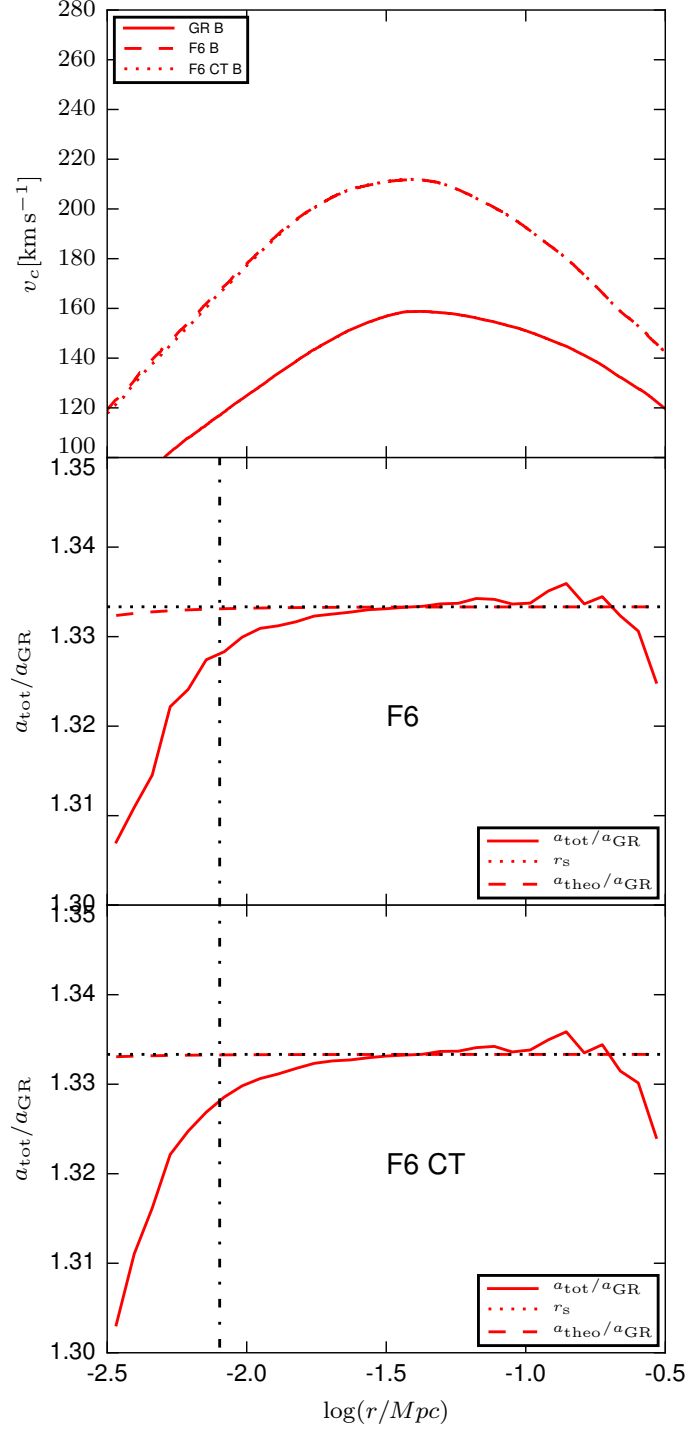


Figure 3.5: Local timestepping test: comparison between a simulation with the standard setup and one with a four times smaller MG-timestep (labeled CT). The *upper panel* shows circular velocity profiles of the central zoomed halo in a Λ CDM simulation and the two $f(R)$ -gravity runs with the different timesteps. The *middle panel* and the *lower panel* display the relative difference between total and GR-force in the two timestep setups.

computation are coupled to the PM-force calculation. In order to avoid a too large PM-MG timestep, it is calculated via

$$\Delta t_{\text{PM-MG}} = \min(\Delta t_{\text{PM}}, \Delta t_{\text{MG}}), \quad (3.13)$$

where the MG timestep is in turn computed from

$$\Delta t_{\text{MG}} = \min(\Delta t_{\text{MG}i}). \quad (3.14)$$

The modified gravity timestep $\Delta t_{\text{MG}i}$ for each individual particle is estimated based on the particles modified gravity acceleration, ensuring that the MG-PM timestep is never too large for any particle in the simulation box. In between the MG-PM timesteps individual standard gravity integration steps are allowed for the short range tree force and the SPH solver in the same way as in P-GADGET3.

The local timestepping scheme is also illustrated in Figure 3.2. The grey shaded region indicates a screened high density area, where the modified gravity forces are negligible. The global modified gravity-PM timestep is thus calculated considering the maximum modified gravity acceleration of all blue particles and the PM step (in fact all particles are considered for the MG timestep but the MG-accelerations of the red and green particles are negligible due to screening). As the dynamical timescales for the red particles are much shorter compared to those of the blue particles, the global MG-PM timestep will be much larger than the standard gravity timestep for the red particles in the over-dense region. In the same way as in P-GADGET3, the tree gravity timesteps will be factors of 2, 4, ... smaller for the green and the red particles, respectively.

In order to test if the modified gravity timestep criterion is stringent enough, a few tests with zoomed simulations of Milky-Way sized halos were carried out (with the B-halo in Arnold *et al.*, 2016). The same simulation (identical initial conditions (ICs), same parameters) was done once with the standard setup described above and once with a four times smaller modified gravity timestep. A comparison of the density profiles of the central halos in the zoomed regions is shown in Figure 3.3. The density curves agree at a 0.5% level until $r = 0.01$ Mpc which shows that a smaller timestep does not change the result for the density, i.e. the result in the standard setup is converged. A similar conclusion can be drawn for the velocity dispersion profiles (Fig. 3.4) and the fifth force to standard force ratio (Fig. 3.5). The difference in the velocity dispersion is smaller than 0.5% until $r < 0.1 r_{200\text{crit}} \approx 0.01$ Mpc as well. The total to GR force ratio is practically indistinguishable for the two timestep sizes in Figure 3.5. One can therefore conclude that the adaptive timestep scheme in MG-GADGET is converged and produces reliable results.

3.3 AREPO

AREPO (Springel, 2010) is a state-of-the-art massively (MPI) parallel cosmological hydrodynamical simulation code which is widely used for large scale simulations.

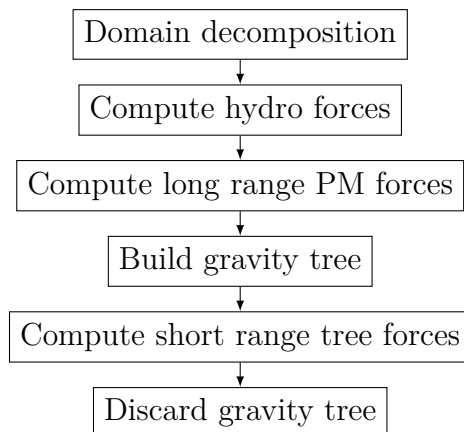
In recent years it was used in high-resolution cosmological simulations of galaxy formation (Vogelsberger *et al.*, 2014b) covering a wide range of baryonic processes like star formation, cooling, stellar- and AGN-feedback. It was also applied in zoomed hydrodynamical simulations of Milky-Way sized galaxies (Marinacci *et al.*, 2014) and in hydrodynamical simulations including magnetic fields (Pakmor *et al.*, 2014) as well as cosmic rays (Pfrommer *et al.*, 2017).

While the gravity solver of AREPO is similar to that of P-GADGET3, the hydrodynamical equations are solved in a completely different way. Instead of using an SPH-solver, AREPO uses a moving Voronoi mesh to obtain the hydrodynamical forces.

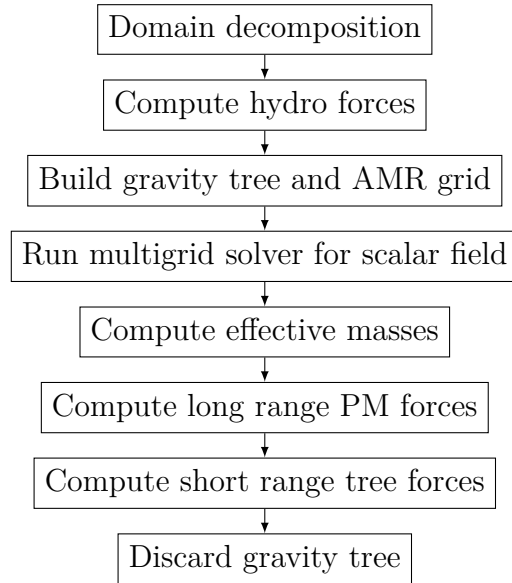
As a part of this work, I implemented a solver for $f(R)$ modified gravity in AREPO which I will describe in detail below. It is similar to the $f(R)$ solver in MG-GADGET described above. I will therefore focus on the differences to MG-GADGET.

3.3.1 The modified gravity solver in AREPO

One of the major differences between AREPO and P-GADGET3 concerns the gravity tree. While the tree is stored at all times (and frequently reconstructed or updated) in P-GADGET3 it is only built for the calculation of the short range tree forces and immediately discarded afterwards in AREPO. This method reduces the memory footprint of the code. As the tree is also needed as an AMR grid for the modified gravity solver and to store the effective masses, the order of the different steps in the force computation algorithm has to be changed for the modified gravity solver. While in the standard setup of AREPO the force computation in the order (on global PM timesteps; Springel, 2010),



the order in the modified gravity mode for global timesteps is:



The memory footprint will thus be significantly higher in the modified gravity mode as the tree is allocated during the PM-force calculation. The code is nevertheless still more memory efficient compared to MG-GADGET. This is partially achieved by storing a major part of the information needed for every AMR cell of the multigrid solver in a separate data structure which is immediately discarded once the field is computed and not in the gravity tree.

The individual steps in the chart above are carried out in a very similar way as in MG-GADGET. In between the global steps multiple tree-gravity calculations for the short range forces can be carried out according to the individual timesteps of the particles. These calculations necessarily involve a tree construction but only for a subset of them a domain decomposition is done.

4 The modified gravity code comparison project

In this chapter I will present a subset of the results from *The modified gravity code comparison project* (Winther *et al.*, 2015) which I contributed to as a part of this thesis. I will focus on the outcomes which are related to MG-GADGET and $f(R)$ -gravity.

4.1 Introduction

While gravity is tested to remarkably high precision on small scales (Will, 2014) it has not been tested to the same degree on large scales. In order to perform such a large scale test of gravity one has to statistically observe the large-scale structure of the universe and compare the outcomes to the expectations from different gravity theories (Jain & Khoury, 2010; Koyama, 2016). In the coming years several large scale structure surveys such as EUCLID or LSST will provide powerful tests of GR on large scales. In order to constrain or rule out possible alternative theories, e.g. the ones described in Section 2.2, they nevertheless require a detailed understanding of how these theories of modified gravity alter the large scale structure of the universe.

As described earlier, theories of modified gravity require screening mechanisms to recover GR in our local environment, leading to a very non-linear behaviour of the underlying equations. Therefore analytic approaches to cosmic structure formation are very limited in theories of this kind. In order to understand how structure formation is affected by theories of modified gravity it is therefore necessary to employ cosmological N-body simulations in these theories.

The methods of the codes used to carry out these simulations should be verified in order to ensure that their results are not significantly affected by their numerical schemes. In order to do so, this project compared the results of a number of different modified gravity simulation codes for different modified gravity models.

In the following I will present the results on how MG-GADGET compares to other modified gravity codes for $f(R)$ -gravity simulations.

4.2 Simulations and Methods

To have a common starting point, all simulations in this chapter were carried out with the same (binary identical) initial conditions. For all codes, a Λ CDM comparison run was carried out in addition to simulations in $|\bar{f}_{R0}| = 10^{-5}$ and $|\bar{f}_{R0}| = 10^{-6}$ modified gravity.

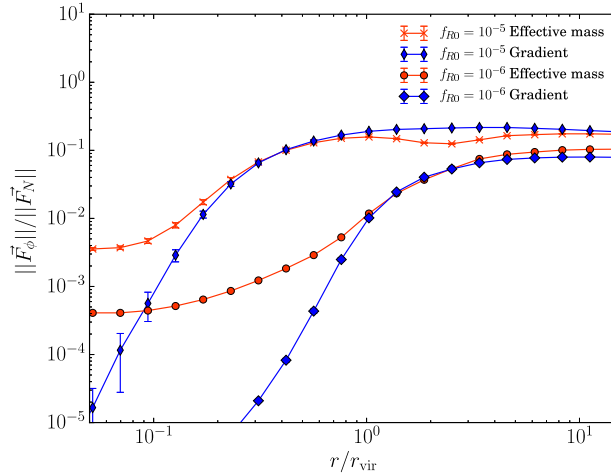


Figure 4.1: The fifth-force to Newtonian force ratio profiles in MG-GADGET for $|\bar{f}_{R0}| = 10^{-5}$ and $|\bar{f}_{R0}| = 10^{-6}$. *Red lines* show forces obtained via the effective mass algorithm, *blue lines* forces which are directly calculated from the field gradients. The force profiles were stacked for all halos in the mass range $10^{14}M_{\odot} < m < 5 \times 10^{14}M_{\odot}$ contained in the simulation box. (from Winther *et al.*, 2015)

The codes compared to MG-GADGET are ISIS and ECOSMOG. Both codes are based on RAMSES, i.e. employ a mesh based technique also for standard gravity. The major difference in the modified gravity part of the codes is that they find the modified gravity force directly from the field gradients on the grid while MG-GADGET employs the effective mass algorithm (see also Section 3.2.2).

The simulations presented below use 512^3 simulation particles in a box of $250 \text{ Mpc}/h$ side length and start at redshift $z = 49$. The set of cosmological parameters is $\Omega_m = 0.269$, $\Omega_{\Lambda} = 0.731$, $h = 0.704$, $n_s = 0.966$ and $\sigma_8 = 0.8$.

4.3 Results

In order to test the effective mass algorithm used in MG-GADGET, Figure 4.1 compares the stacked fifth-force to standard force profiles in halos in the mass range between $10^{14}M_{\odot} < m < 5 \times 10^{14}M_{\odot}$ for the two force calculation methods (see Section 3.2.2). All forces are obtained starting from the same density field at $z = 0$. The forces of the effective mass algorithm are part of the standard output while I implemented an additional mapping routine for the field gradients to also be able to calculate the fifth force directly from the AMR grid in MG-GADGET.

As one can see from the plot, the forces of the two methods are in good agreement in the outer region ($r > r_{\text{vir}}$) of the halos for the $|\bar{f}_{R0}| = 10^{-6}$ model. In the inner region the discrepancy is large. While interpolated fifth forces keep dropping over the whole range of the plot, the effective mass force ratio does not drop below 5×10^{-4} . The reason is that large positive and negative effective masses have to

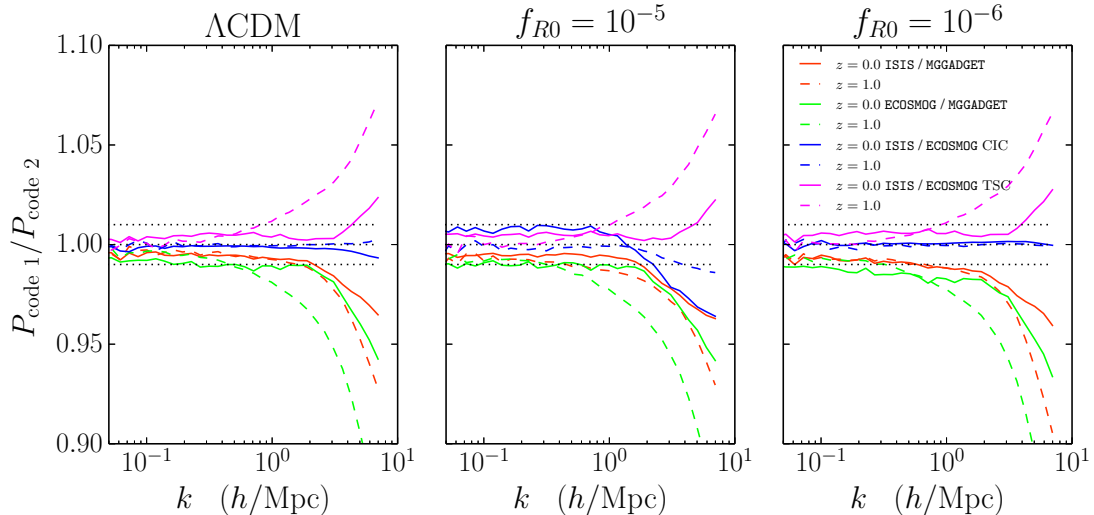


Figure 4.2: The ratio of the matter power spectra obtained with different codes for a Λ CDM model (*left panel*), $|\bar{f}_{R0}| = 10^{-5}$ (*center panel*) and $|\bar{f}_{R0}| = 10^{-6}$ (*right panel*) at different redshifts. The dotted lines display equality and a 1% error margin. For the ECOSMOG code both a rectangular (CIC) and a triangular (TSC) shaped kernel for the mass and force assignment are used. (from Winther *et al.*, 2015)

cancel each other in screened regions which leads to relatively large numerical errors. In practice, these residual forces will have no effect on the total acceleration as the fifth force contribution is way below 1% of the total force at these radii.

For the $|\bar{f}_{R0}| = 10^{-5}$ model, the picture is very similar in the inner regions of the halo but there is an additional small force discrepancy at $r = 2r_{\text{vir}}$, i.e. in a region where the fifth force contributes significantly to the total force. In the regions where the chameleon screening mechanism sets in, the two curves match each other very well. The following results will show, that these force discrepancies do not lead to significant deviations in other observables.

In order to analyze the consistency of the matter power spectra obtained from simulations with the different codes one has to distinguish between differences induced by the base codes, i.e. already in the Λ CDM part of the power spectrum and differences induced by the modified gravity solvers. Figure 4.2 displays the ratio of the total matter power spectrum between different codes at redshift zero and one for $|\bar{f}_{R0}| = 10^{-5}$, $|\bar{f}_{R0}| = 10^{-6}$ and a Λ CDM comparison simulation. The simulations with ECOSMOG were carried out twice with different assignment kernels. The codes agree with a 2% error until $k = 1$ for all models and redshifts. As ISIS and ECOSMOG TSC are two implementations of the very same method and based on the same code, it is not surprising that the results of both codes are basically indistinguishable for the standard model and for the $|\bar{f}_{R0}| = 10^{-6}$ simulations. There are slight deviations in the $|\bar{f}_{R0}| = 10^{-5}$ model but the errors are still within a 1% error until $k = 3$. The TSC kernel in ECOSMOG produces significantly less power compared to ISIS on

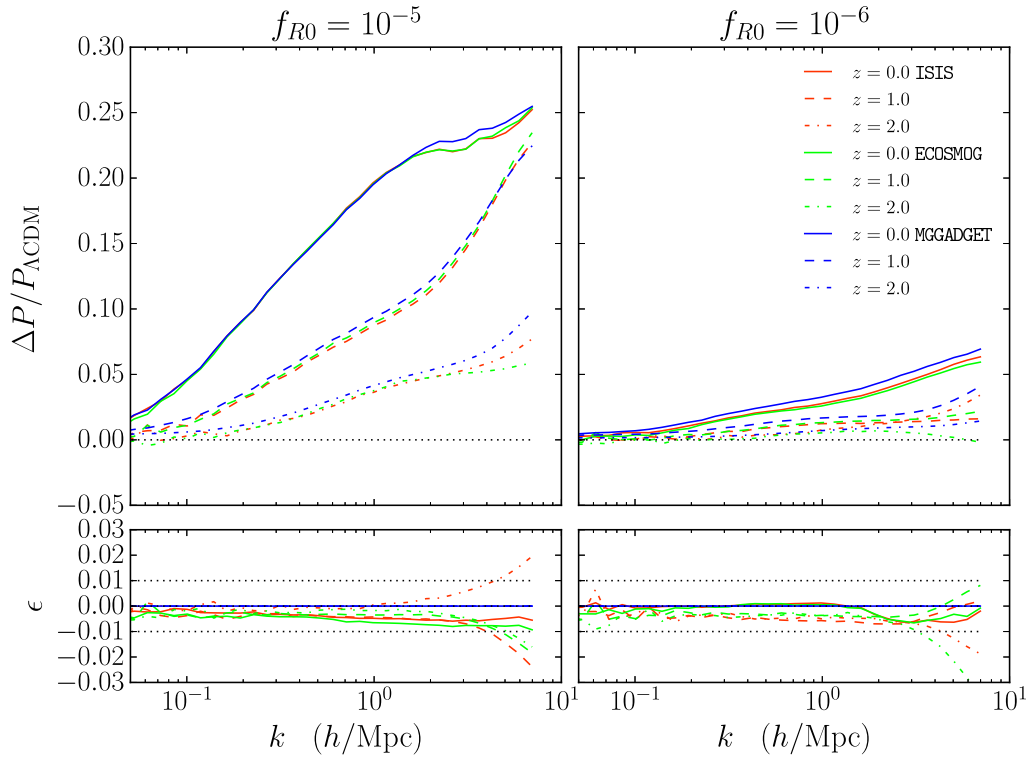


Figure 4.3: The *upper panels* display the relative difference of the $|\bar{f}_{R0}| = 10^{-5}$ and $|\bar{f}_{R0}| = 10^{-6}$ matter power spectra obtained from simulations carried out with ISIS, ECOSMOG and MG-GADGET with respect to power spectra from Λ CDM simulations carried out with the same code. In the *lower panels* the results relative difference compared to MG-GADGET is shown. The black dotted lines indicate a 1% error margin. (from Winther *et al.*, 2015)

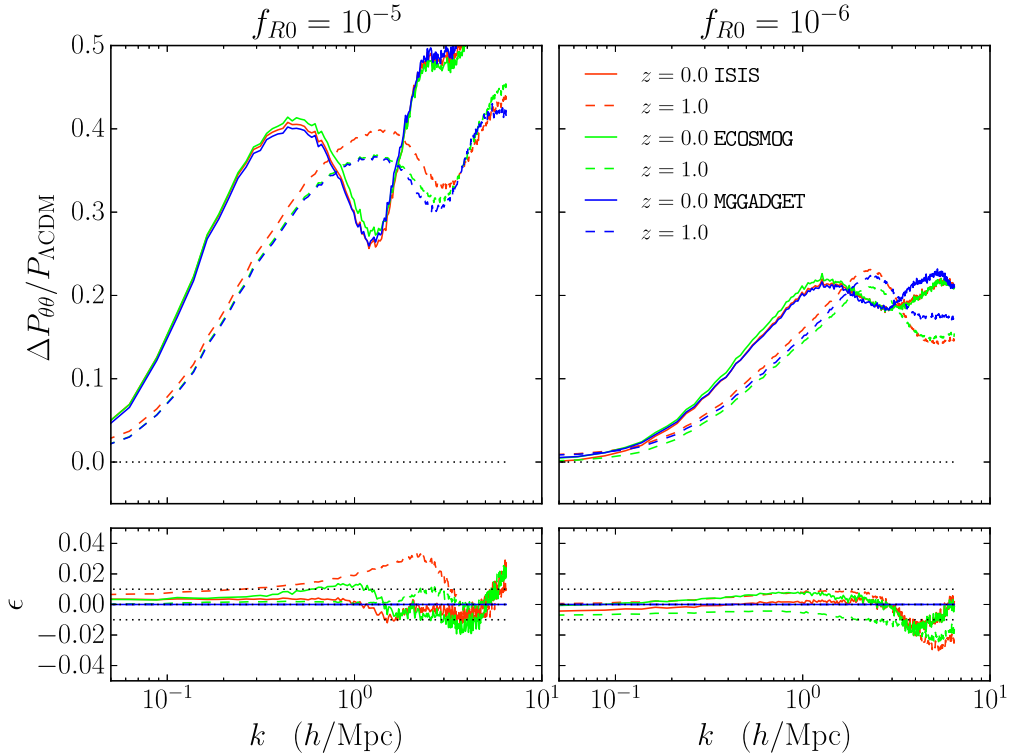


Figure 4.4: Same as Figure 4.3 but for the velocity divergence power spectrum. (from Winther *et al.*, 2015)

small scales, underlining that the power spectrum is quite sensitive to small numerical changes. Comparing both ECOSMOG and ISIS to MG-GADGET it turns out that both codes produce less power on small scales for all models and redshifts. This is a known issue with grid codes which struggle to reproduce structures on the very smallest scales due to their limited cell size. Tree codes like P-GADGET3 do not have this problem and will therefore show larger values for the power spectrum on small scales. As the results for all three models shown in the plot are very similar, I conclude that the differences are mainly induced by the base codes and not by the modified gravity solvers, a finding which is confirmed by Figure 4.3. It illustrates the relative difference in the matter power spectrum between $|\bar{f}_{R0}| = 10^{-5}$ and $|\bar{f}_{R0}| = 10^{-6}$ with respect to a Λ CDM model for the codes, i.e. it provides a test of the modified gravity modules. The results of MG-GADGET, ISIS and ECOSMOG agree on a one percent level until $k = 10$. Keeping in mind that it is very difficult to bring Λ CDM power spectra of different codes to that level of agreement (Schneider *et al.*, 2016), this result shows that modified gravity solvers of all codes produce reliable results for the matter power spectrum.

A very similar result is obtained for the velocity divergence power spectra, $P_{\theta\theta} \equiv \langle \theta_k^2 \rangle$, $\theta_k = \nabla \cdot \mathbf{v}/H_o$, shown in Figure 4.4. Except for the ISIS power spectrum at $z = 1$, all results agree within a 1% error margin until $k = 3$.

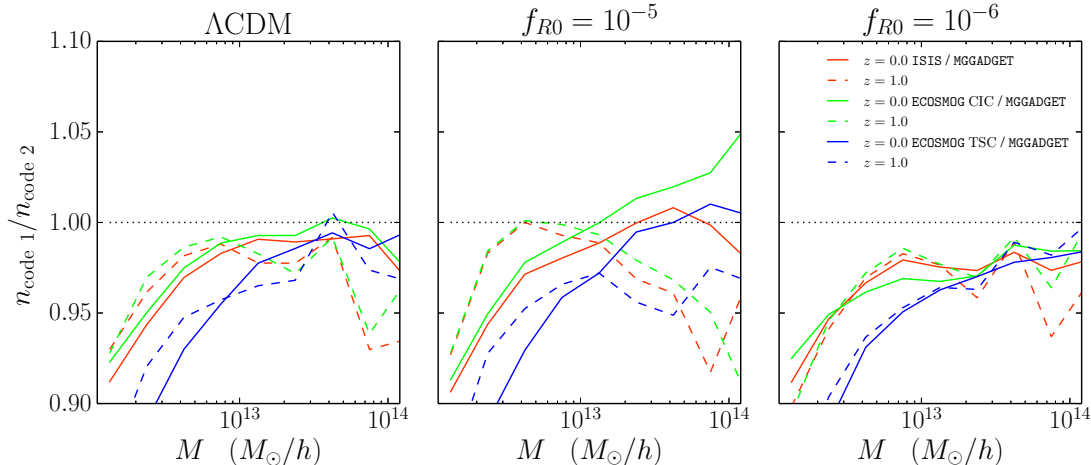


Figure 4.5: The ratio of the halo mass functions obtained with different codes for a Λ CDM model (*left panel*), $|\bar{f}_{R0}| = 10^{-5}$ (*center panel*) and $|\bar{f}_{R0}| = 10^{-6}$ (*right panel*) at different redshifts. The dotted lines display equality. For the ECOSMOG code both a rectangular (CIC) and a triangular (TSC) shaped kernel for the mass and force assignment are used. (from Winther *et al.*, 2015)

The differences between the codes in terms of the halo mass functions are larger compared to the power spectra but still mainly induced by differences in the base codes, as one can see from Figures 4.5 and 4.6. Both ECOSMOG and ISIS produce less halos than MG-GADGET in Λ CDM simulations. The discrepancy is larger at the low mass end of the plot, reaching 10% for milky-way sized halos. The reason is again that grid codes struggle to form structures on small scales due to their finite grid size.

The differences induced by the modified gravity solvers in Figure 4.6 are much smaller. The enhancement of the mass function due to $f(R)$ -gravity agrees almost perfectly for lower mass halos at $z = 0$. The relative differences at higher masses do not exceed 2% and are likely induced by statistical fluctuations due to the low number of high mass objects in the simulation boxes. At $z = 1$ the deviations are slightly higher but still within a range of 5%, underlining that the modified gravity solvers work very reliably.

Figure 4.7 shows stacked f_R profiles for halos of different mass bins in the simulations. The least massive halos are obviously unscreened in $|\bar{f}_{R0}| = 10^{-5}$ as their scalar field profile stays at its background value over the whole radial range of the plot. For more massive halos, the field starts to deviate from the background value around r_{vir} and drops for several orders of magnitude towards the center of the object. The $f(R)$ effects will thus be largely screened inside r_{vir} for these objects. As expected, the onset of screening is triggered already in lower mass halos for the $|\bar{f}_{R0}| = 10^{-6}$ model. The differences between the results from the different codes are almost negligible for the stronger $f(R)$ model considered. For $|\bar{f}_{R0}| = 10^{-6}$, the re-

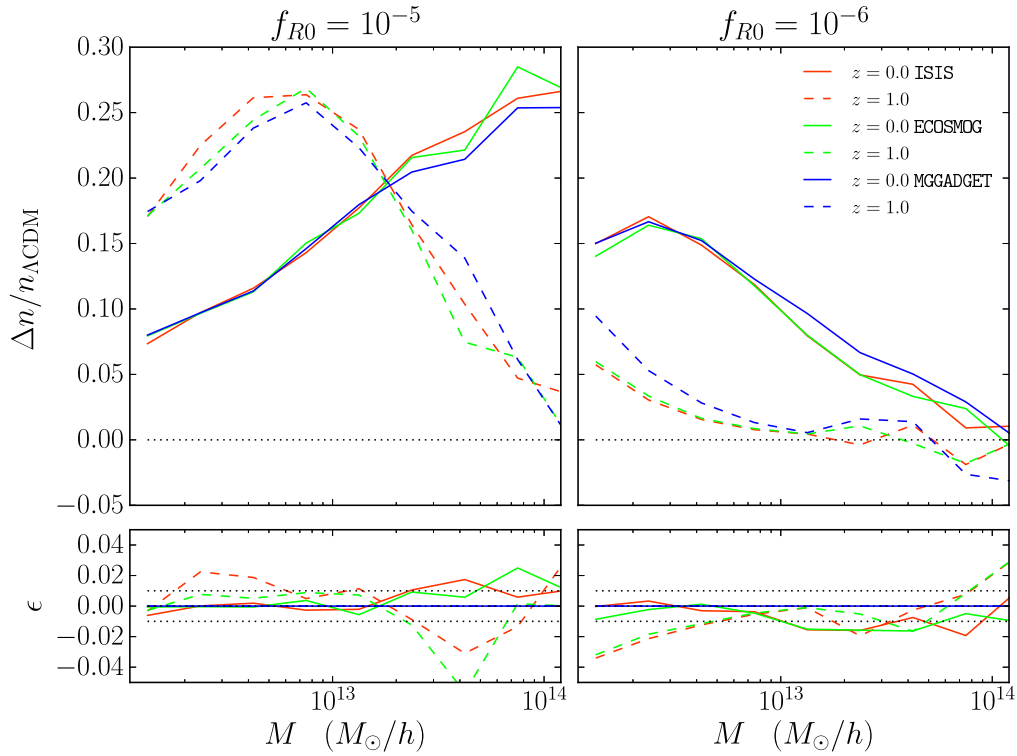


Figure 4.6: The *upper panels* display the relative difference of the $|\bar{f}_{R0}|=10^{-5}$ and $|\bar{f}_{R0}|=10^{-6}$ halo mass functions obtained from simulations carried out with ISIS, ECOSMOG and MG-GADGET with respect to mass functions from Λ CDM simulations carried out with the same code at different redshifts. In the *lower panels* the results relative difference compared to MG-GADGET is shown. The black dotted lines indicate a 1% error margin. (from Winther *et al.*, 2015)

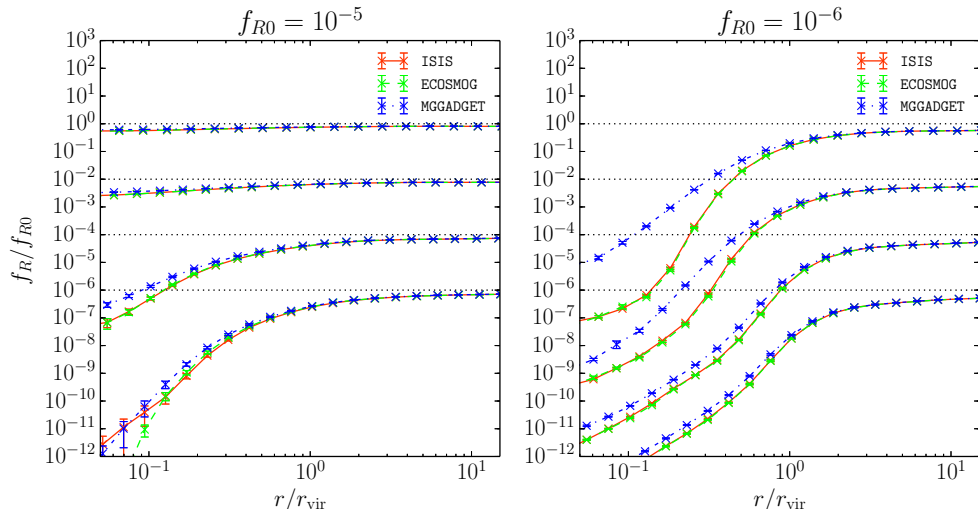


Figure 4.7: Stacked scalar field profiles of the halos in the simulations carried out with the three different codes. The profiles are shown for 4 different mass bins: $M \in [1 \cdot 10^{14}, 5 \cdot 10^{14}]$, $M \in [5 \cdot 10^{13}, 1 \cdot 10^{14}]$, $M \in [1 \cdot 10^{13}, 5 \cdot 10^{13}]$ and $M \in [5 \cdot 10^{12}, 1 \cdot 10^{13}] M_{\odot}/h$ (bottom to top), which are vertically displaced in the plot. The *dotted black lines* indicate equality for each of the bins. The *left panel* displays the results for $|\bar{f}_{R0}| = 10^{-5}$, the *right panel* for $|\bar{f}_{R0}| = 10^{-6}$. (from Winther *et al.*, 2015)

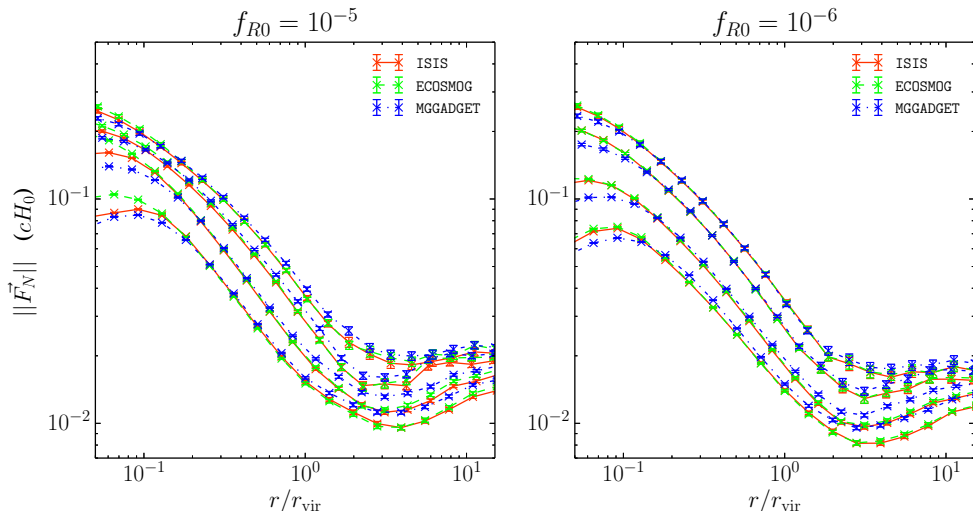


Figure 4.8: Stacked Newtonian force profiles of the halos in the simulations shown for the same mass bins used in Figure 4.7 (with more to less massive halos from top to bottom). The *left panel* displays the results for $|\bar{f}_{R0}| = 10^{-5}$, the *right panel* for $|\bar{f}_{R0}| = 10^{-6}$. (from Winther *et al.*, 2015)

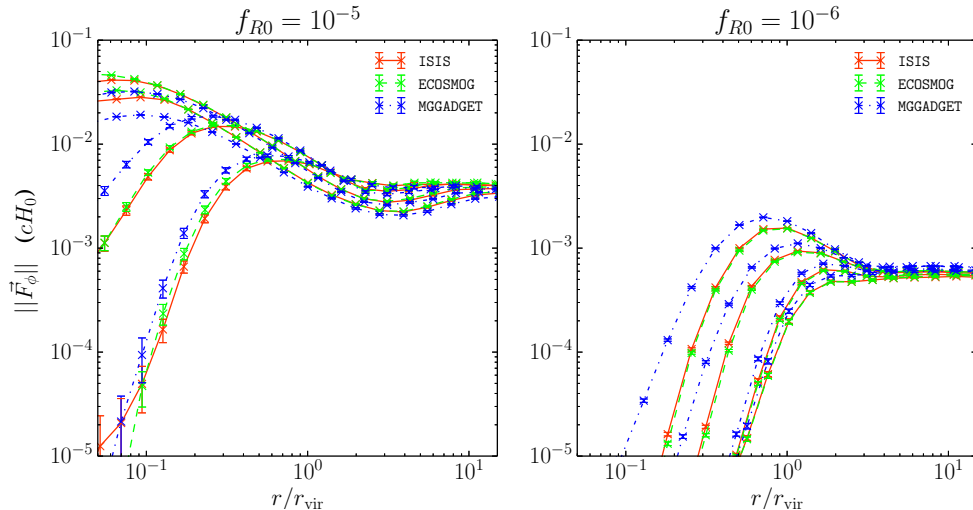


Figure 4.9: Stacked fifth force profiles of the halos in the simulations shown for the same mass bins used in Figure 4.7 (with more to less massive halos from top to bottom). The *left panel* displays the results for $|\bar{f}_{R0}| = 10^{-5}$, the *right panel* for $|\bar{f}_{R0}| = 10^{-6}$. (from Winther *et al.*, 2015)

sults of MG-GADGET deviate from those of the other codes. While the curves agree very well in the outer unscreened regions and at the onset of screening, there are large differences in the inner screened regions for lower mass halos. The fields calculated with ISIS and ECOSMOG drop by 7 orders of magnitude until the innermost radius of the plot. MG-GADGET gives a field value which is only $10^{-5} \times \bar{f}_{R0}$ at this radius. The field calculation in the codes is practically identical, this difference can thus only be caused by a different residual threshold in the multi-grid solvers. As the following results demonstrate, the deviations in the field in screened regions do not have an effect on the total forces because the fifth force is much smaller than the Newtonian force there.

In order to also compare the standard gravity force of the base codes, Figure 4.8 shows stacked Newtonian force profiles. The plot does not show a significant difference on a code to code basis. As the mass distribution inside the halos in the two $f(R)$ models is slightly different, the curves are not exactly the same for both theories.

The force contribution from $f(R)$ -gravity, i.e. the fifth force, is compared in Figure 4.9. The forces agree very well in the outer parts of the halo but there are again differences between MG-GADGET and the other codes in the central regions. There are two major reasons for the deviation. First, the scalar fields deviate in screened regions (see Figure 4.7) and second, the effective mass mechanism will produce slightly different results for the forces compared to the gradient based method used in ISIS and ECOSMOG. These deviations in screened regions are even more prominent in Figure 4.10, which displays the ratio of fifth- to standard force for the three codes in $|\bar{f}_{R0}| = 10^{-5}$ and $|\bar{f}_{R0}| = 10^{-6}$. Larger deviations do nevertheless only appear in

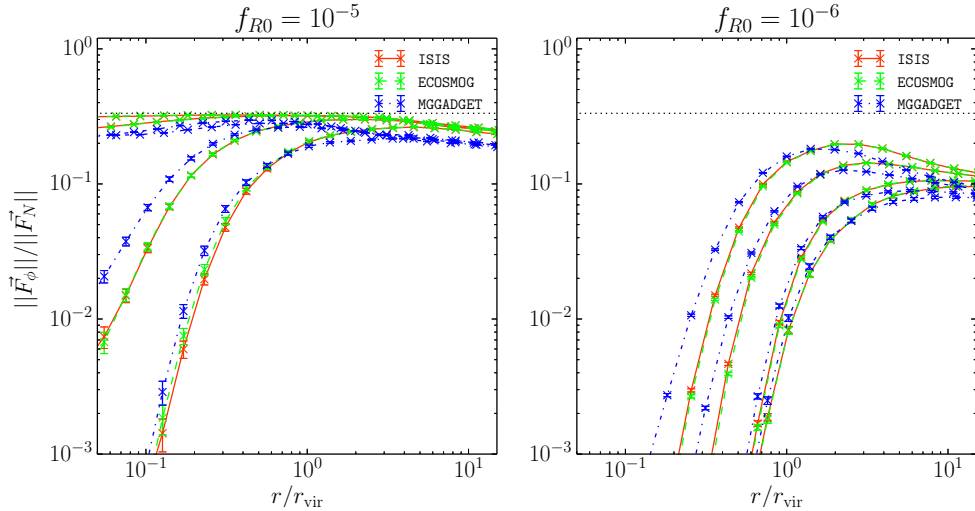


Figure 4.10: Stacked fifth force to standard force ratio profiles of the halos in the simulations shown for the same mass bins used in Figure 4.7 (with more to less massive halos from bottom to top). The *left panel* displays the results for $|\bar{f}_{R0}| = 10^{-5}$, the *right panel* for $|\bar{f}_{R0}| = 10^{-6}$. Vertical *dotted lines* indicate the theoretically expected force ratio in unscreened regions of $F_\phi = F_N/3$. (from Winther *et al.*, 2015)

regions where the fifth force contribution is negligible and will therefore not have an impact on the total force.

Figure 4.11 shows the ratio of stacked density profiles of dark matter halos in the simulations carried out with the different codes. Apart from statistical fluctuations, there are no significant differences between the codes for the stronger $|\bar{f}_{R0}| = 10^{-5}$ model. The only difference which can be spotted in $|\bar{f}_{R0}| = 10^{-6}$, is that the least massive group of halos in the ISIS and ECOSMOG simulations is about 10% less dense in the center compared to MG-GADGET.

Velocity dispersion profiles for the same mass bins as above are displayed in Figure 4.12. The results agree very well for both models and all mass bins.

4.4 Conclusion and discussion

Testing gravity on large scales with upcoming large scale structure surveys requires a detailed understanding of how theories of modified gravity alter structure formation. Modified gravity simulations thereby deliver a key ingredient to these upcoming tests of GR. In this Chapter I presented a comparison between different codes which are capable of simulating cosmic structure formation in $f(R)$ -gravity. In order to do so, the considered codes (ISIS, ECOSMOG and MG-GADGET) solve the field equations for the scalar field using an iterative multi-grid technique but slightly different approaches to obtain the gravitational forces. With the aim to validate the

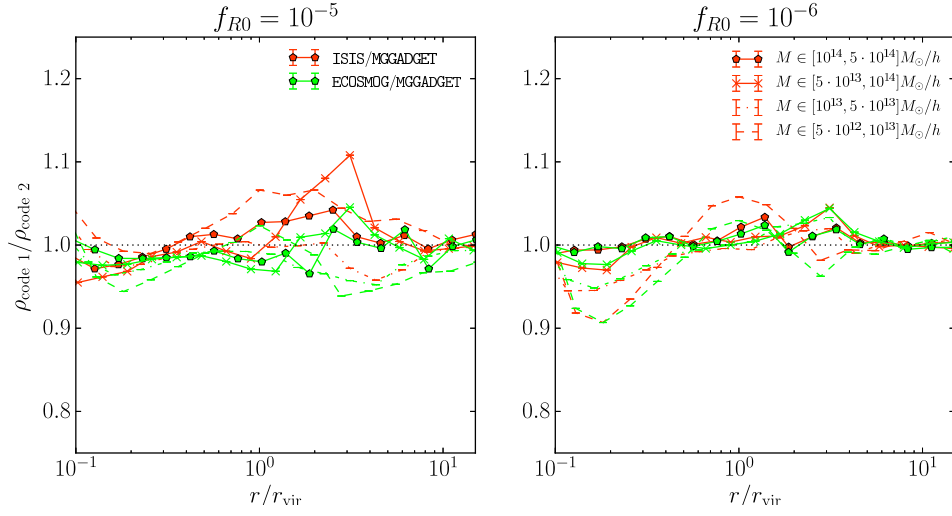


Figure 4.11: Ratios of the stacked density profiles of the halos obtained from simulations carried out with different codes. The halos are grouped in the same mass bins as for Figure 4.7. The *dotted lines* indicate unity; the *left panel* shows results for $|\bar{f}_{R0}| = 10^{-5}$, the *right panel* for $|\bar{f}_{R0}| = 10^{-6}$. (from Winther *et al.*, 2015)

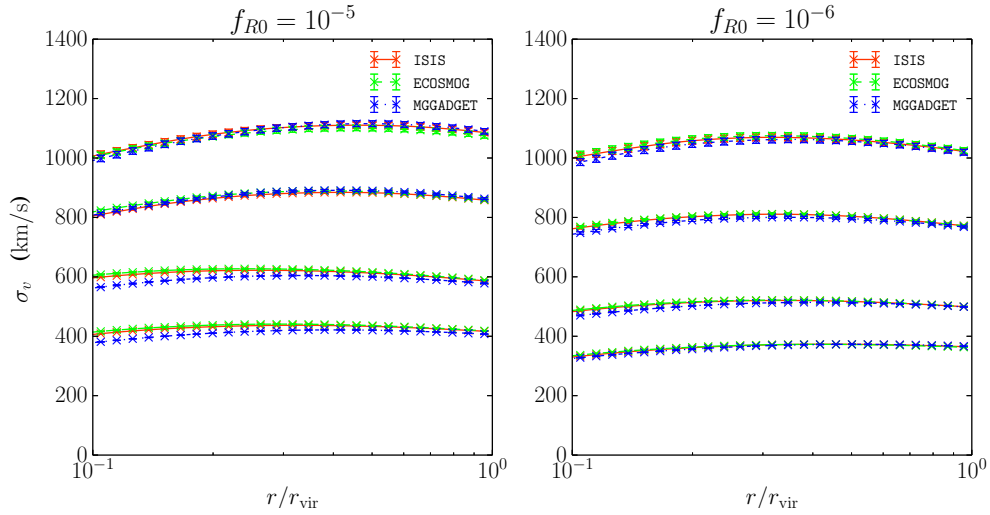


Figure 4.12: Stacked velocity profiles for halos of the same mass bins as in Figure 4.7 computed with the different codes. The *left panel* shows results for $|\bar{f}_{R0}| = 10^{-5}$, the *right panel* for $|\bar{f}_{R0}| = 10^{-6}$. (from Winther *et al.*, 2015)

methods of the codes, I therefore focused on comparing the differences induced by modified gravity.

One can summarize the findings as follows.

- The matter power spectra agree at a one percent level until $k = 1$. Differences between the codes are mainly induced by the Λ CDM parts. The enhancement in the power spectrum due to $f(R)$ -gravity agrees on a 1%-level for $k < 3$.
- The velocity power spectrum enhancement differences at $z = 0$ are completely within a 1% error margin, showing very good agreement between the codes.
- The halo mass functions differ by about 10% between the codes. The main source of these deviations are again the base codes. Errors from the modified gravity modules stay with a 5% margin.
- I found that the scalar field profiles agree very well in unscreened regions while there are differences in the screened parts of halos. These will nevertheless have a negligible effect on the total force.
- The differences in the fields are also one source for differences in the fifth forces. Together with different force calculation schemes they lead to a deviation in the modified gravity forces in screened regions. But because those regions are screened, there will again be no significant effects on the total force.
- The density and velocity dispersion profiles do not show significant differences between the codes.

Summarizing one can say that the results of the codes agree on a percent-level. Residual differences are induced by different relaxation criteria and the effective mass scheme used in MG-GADGET. It is important to point out here that the uncertainty in statistical cosmological measures caused by different modified gravity solvers is much smaller than the uncertainties due to the Λ CDM parts of the codes and due to baryonic physics. It will therefore be important to either find observables which are less affected by baryons or to find a robust description of baryonic feedback effects, and to improve the Λ CDM solvers in order to meet the requirements of upcoming large scale structure surveys.

5 The Lyman- α forest in $f(R)$ -gravity ¹

5.1 Introduction

In this work, I will for the first time extend the analysis of hydrodynamical $f(R)$ modified gravity simulations to the statistical properties of the Lyman- α forest. Employing the modified gravity simulation code MG-GADGET I carry out simulations to redshift $z = 2$, given that most Lyman- α data lies at redshifts $z \sim 2 - 4$. Creating synthetic Lyman- α absorption spectra from the simulation outputs, I present an analysis of flux PDFs, flux power spectra, line shape statistics, as well as of the matter power spectrum for both $f(R)$ -gravity and an ordinary Λ CDM model. I particularly focus on the relative differences between these two cosmologies and compare my results to observations.

This Chapter is structured as follows. Section 5.2 describes the simulation set I have carried out. In Section 5.3, I present my main results, and I conclude in Section 5.4.

5.2 Simulations and methods

Modeling the statistical properties of the Lyman- α forest requires a cosmological simulation code which is capable of accounting for a variety of gas physics, including photo-heating, radiative cooling and star formation. For $f(R)$ -gravity, the fifth force influence has to be computed in addition.

The simulations used to obtain the results on the Lyman- α forest presented in this section were carried out with MG-GADGET. Making use of its SPH hydrodynamics solver and the modified gravity solver a set of hydrodynamical simulations with cooling were carried out. In order to keep the computational cost at a reasonable level, the simulations were done with the "Quick Lyman- α " setup of the code which turns high-density gas into stars before the actual threshold for star-formation is reached. This avoids the computationally costly integration of high-density gas on short dynamical timescales. The effect on the Lyman- α forest signal is negligible as only regions far inside the virial radius r_{200} of the halos in the simulations are affected.

For a reliable analysis of $f(R)$'s impact on the Lyman- α forest it is necessary to run simulations in both modified gravity and Λ CDM using identical initial conditions. I do so by carrying out hydrodynamical simulations using 2×512^3 particles (512^3

¹The results and large parts of the text of this chapter have already been published in Arnold *et al.* (2015).

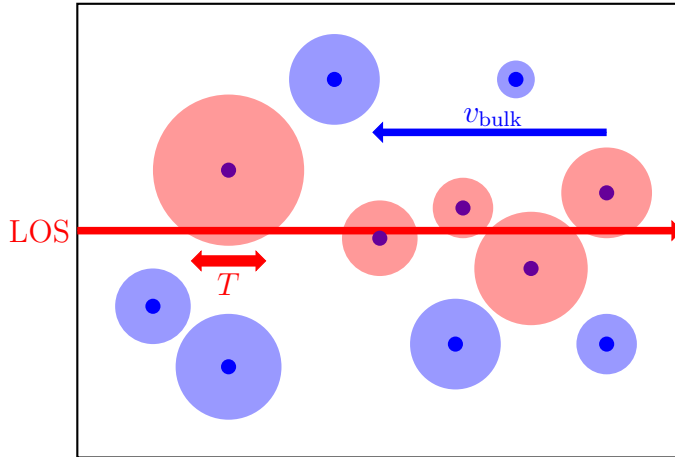


Figure 5.1: Sketch of the method to extract synthetic Lyman- α absorption spectra from a simulation snapshot. The red line indicates the line-of-sight. All SPH particles whose smoothing length it intersects are considered for the spectrum calculation.

each gas and dark matter) in a $60 h^{-1}\text{Mpc}$ box for $|\bar{f}_{R0}| = 10^{-5}$ and GR. To explore the parameter space at a coarse level, a set of smaller box simulations at the same mass resolution, but using 2×128^3 particles in a $15 h^{-1}\text{Mpc}$ box for $|\bar{f}_{R0}| = 10^{-4}$, 10^{-5} and GR were done. The set of cosmological parameters is $\Omega_m = 0.305$, $\Omega_\Lambda = 0.695$, $\Omega_b = 0.048$ and $H_0 = 0.679$, consistent with CMB constraints.

To extract the statistical properties of the Lyman- α forest, synthetic absorption spectra were calculated at different redshifts. Using the output of the hydrodynamical simulations, I randomly select 5000 lines-of-sight (LOS), each intersecting the simulation box parallel to one of the three coordinate axes. Dividing each line into 2048 pixels, the density of the neutral hydrogen, the gas temperature and the neutral gas weighted velocity fields of the gas are computed along the lines of sight. For this computation, we consider all SPH particles whose smoothing length is intersected by the sight-line (see also Fig. 5.1). With the bulk flow velocities and temperatures along the line of sight in hand, I then account for kinematic Doppler shifts and thermal broadening of the absorption lines, which are themselves calculated from the neutral hydrogen density. As final output, the code creates for each LOS a file with optical depth τ as a function of distance along the LOS. This output can be converted into a transmitted flux $F = e^{-\tau}$.

In the simulations, MG-GADGET uses a tabulated UV-background² which allows the calculation of gas temperatures and ionization fractions assuming ionization equilibrium. The results might however not fit the mean Lyman- α flux transmission

² Taken from Haardt & Madau (2012), however with the He II photo-heating rate boosted by a factor 1.7 for $2.2 < z < 3.4$. This slight modification results in a better agreement with observational constraints (Becker *et al.*, 2011) on the temperature of the intergalactic medium.

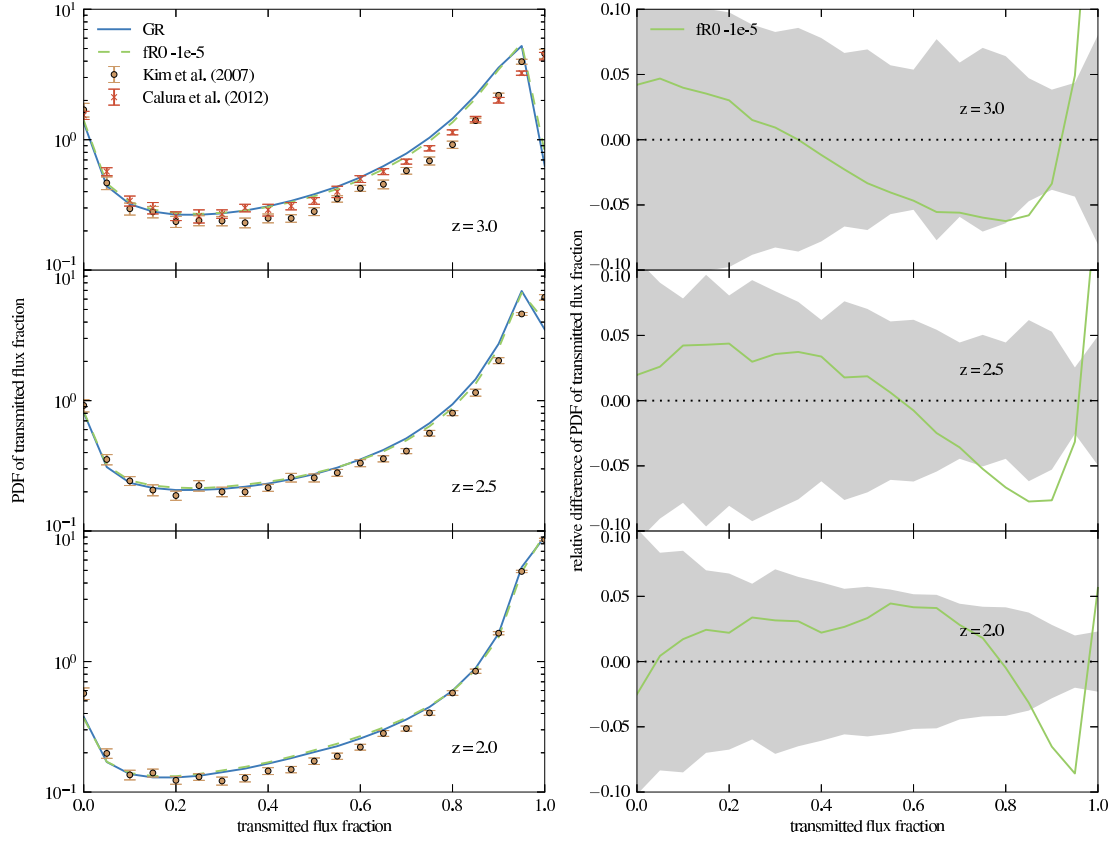


Figure 5.2: *Left panel:* PDF of the transmitted flux fraction for different redshifts for Λ CDM and $|f_{R0}| = 10^{-5}$, using the results of the large simulation boxes. The dots with error-bars show the data of Kim *et al.* (2007). For $z = 3$, the observational results of Calura *et al.* (2012) are shown in addition (I plot the “no metals, no LLS” values of this work here). *Right panel:* relative difference of the PDFs on the left hand side. The shaded regions show the 1σ relative errors of the observational results of Kim *et al.* (2007). The mean transmission is tuned to the values of this work in both panels.

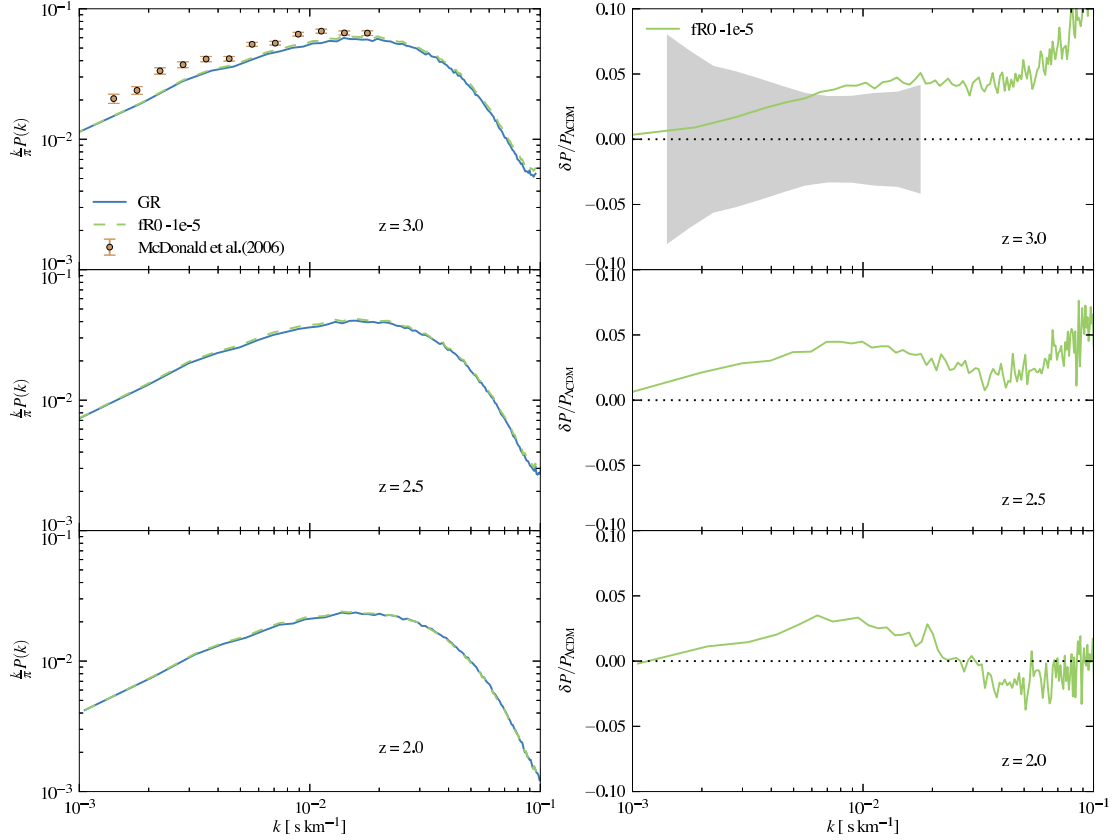


Figure 5.3: *Left panel:* Flux power spectra for $f(R)$ -gravity and ΛCDM obtained from the $60 h^{-1}\text{Mpc}$ simulation boxes at different redshifts. The dots with error-bars show the results of McDonald *et al.* (2006). *Right panel:* relative difference in the flux power spectra shown on the left hand side. The shaded area represents the relative errors of the McDonald *et al.* (2006) results at $z = 3$. The mean transmission is tuned to the values of Kim *et al.* (2007) for both panels.

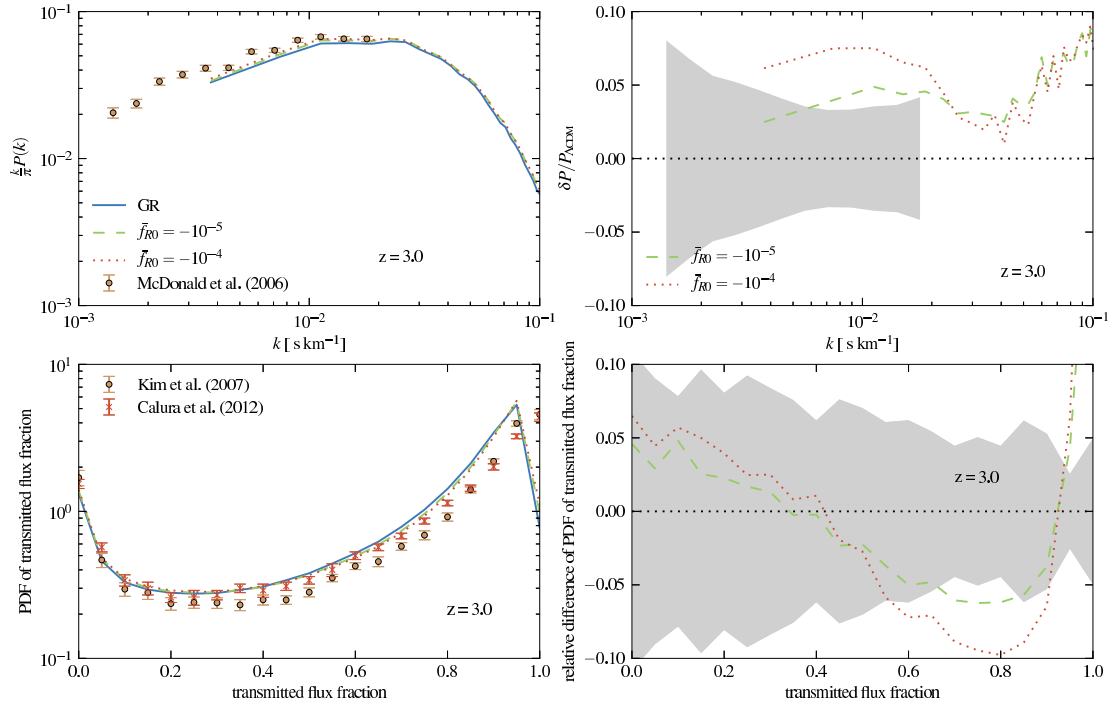


Figure 5.4: *Top panels:* Same as Figure 5.3. *Bottom panels:* same as Figure 5.2. In contrast to the previous figures the results are obtained from the $15 h^{-1} \text{Mpc}$ simulation boxes and for both $|\bar{f}_{R0}| = 10^{-4}$ and 10^{-5} .

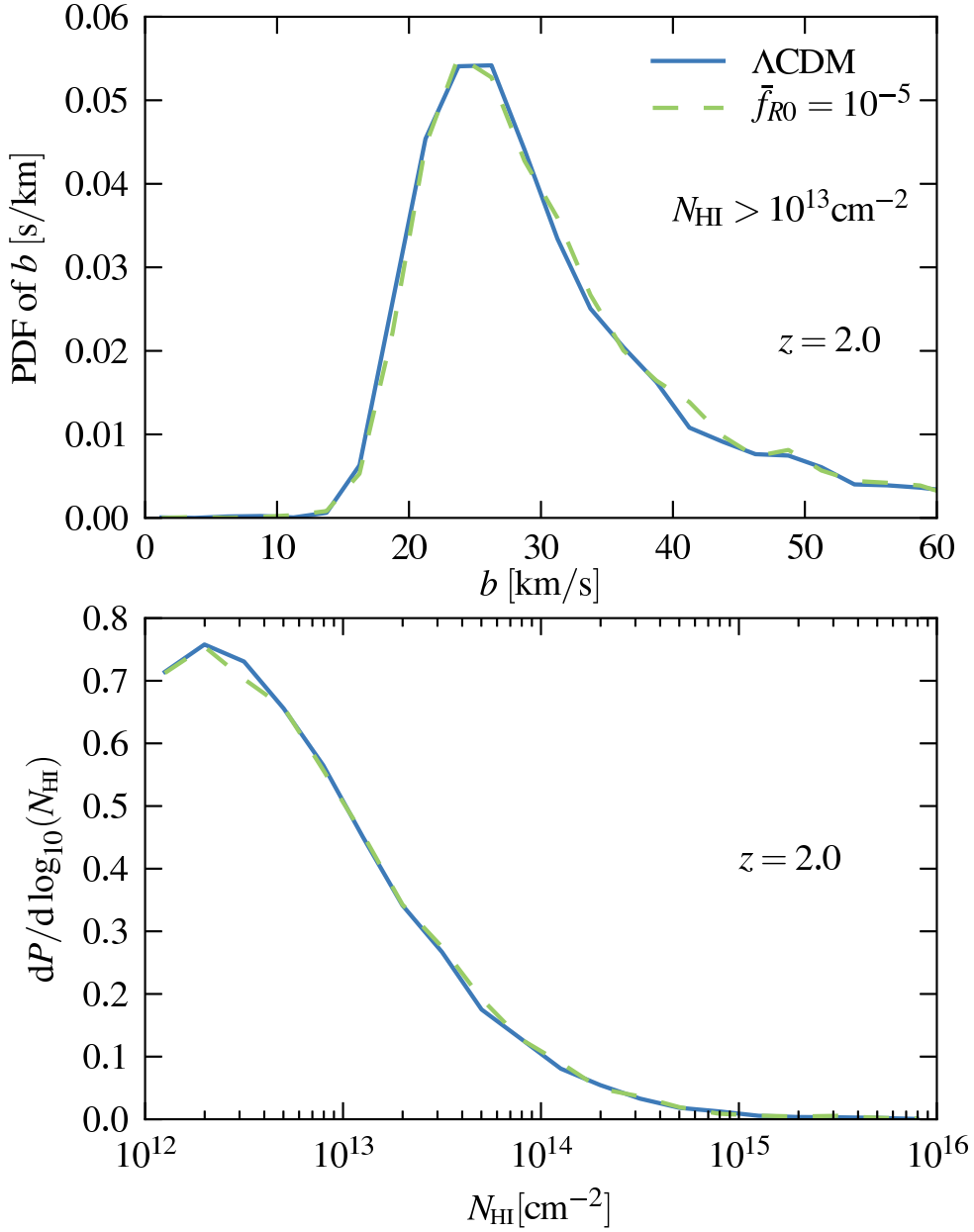


Figure 5.5: *Upper panel:* PDF of the line-widths of the Voigt profile fits to the Lyman- α absorption lines in the synthetic spectra for all lines with neutral hydrogen column density $N_{\text{HI}} > 10^{13} \text{cm}^{-2}$ at $z = 2$. *Lower panel:* normalized PDF of the column density, considering all lines with $N_{\text{HI}} > 10^{12} \text{cm}^{-2}$ at the same redshift. The spectra for both panels were tuned to the mean transmission of Becker *et al.* (2013) and were calculated from the $60 h^{-1} \text{Mpc}$ simulations.

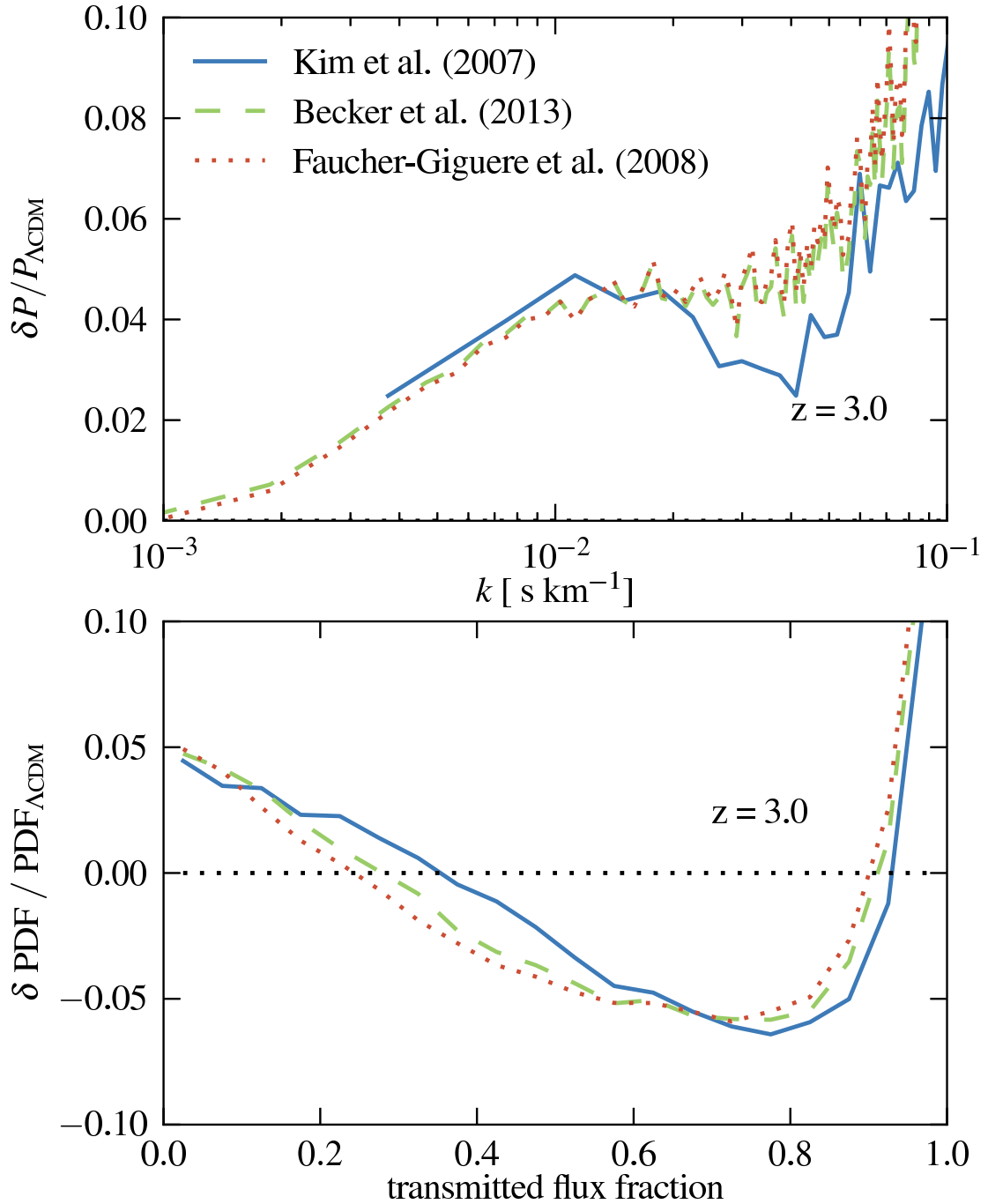


Figure 5.6: *Upper panel:* relative difference between $f(R)$ and ΛCDM in the Lyman- α flux power spectrum; *lower panel:* relative difference between modified gravity and GR in the PDF of the transmitted flux fraction. For both plots, the values of the mean transmitted flux were tuned either to Kim *et al.* (2007, *blue solid line*), Becker *et al.* (2013, *green dashed line*), or Faucher-Giguère *et al.* (2008, *brown dotted line*), respectively. The results refer to $z = 3$.

actually seen in the observational data. In order to compare the mock spectra to observations more faithfully, it is therefore necessary to tune the mean transmitted flux to the corresponding value obtained in the observations. I perform this rescaling of the optical depths, which is a standard procedure in theoretical studies of the Lyman- α forest, in the post-processing of the LOS data.

5.3 Results

In analyzing the synthetic Lyman- α absorption spectra, we first consider the PDF of the transmitted flux fraction in the $60 h^{-1}\text{Mpc}$ box simulations for both $|\bar{f}_{R0}| = 10^{-5}$ and ΛCDM . Figure 5.2 shows these PDFs at redshifts $z = 2, 2.5$ and 3 (*left hand panels*), as well as the relative differences between the two cosmological models (*right hand panels*). The mean transmitted flux fraction is tuned in this plot to the observational values of Kim *et al.* (2007). We also show this data in the panels on the left hand side and its relative errors on the right hand side, for reference. In addition, the results of Calura *et al.* (2012) are shown for redshift $z = 3$. In both observations metal lines were excised, in the latter also Lyman-limit systems (LLS). The mean transmission measured by Calura *et al.* (2012) is consistent with the one of Kim *et al.* (2007). One can thus compare to the same theoretical prediction.

Comparing the absolute values, it is obvious that, despite the tuning to the same effective $\bar{\tau}$, the simulation results do not match the observations particularly well. Especially at redshift $z = 3$, the gap between the simulation results of both $f(R)$ gravity and GR and the observational values of Kim *et al.* (2007) is much larger than the error-bars. At intermediate fluxes, the Calura *et al.* (2012) results are much closer to the simulations. Nevertheless, the differences at large transmitted flux fractions clearly exceed the 3σ observational error. Considering the panels for redshift $z = 2$ and 2.5 , the discrepancies between simulations and the observational data are smaller, but in certain regimes still larger than 3σ . These differences might have their origin in the still uncertain systematic errors of observations (like, e.g., in the continuum placement) and simulations, in an underestimate of the statistical errors (Rollinde *et al.*, 2013) or in an unaccounted heating of the very low-density intergalactic medium (Bolton *et al.*, 2008; Viel *et al.*, 2009) by radiative transfer (McQuinn *et al.*, 2009; Compostella *et al.*, 2013) and non-ionization-equilibrium (Puchwein *et al.*, 2014) effects or, as recently suggested, by TeV blazars (Broderick *et al.*, 2012; Puchwein *et al.*, 2012).

The difference between $|\bar{f}_{R0}| = 10^{-5}$ and ΛCDM is much smaller than the difference between the simulation results and the observed values and somewhat smaller than the error-bars of the observations. This is even more obvious in the right hand panels of Figure 5.2. Comparing the relative difference in the flux PDF between $f(R)$ and GR, it turns out that the differences between the models are mostly within the observational errors for individual flux bins for all considered redshifts. The overall deviation over many flux bins and redshifts could, however, still be statistically significant if systematic effects were better understood. Given the current uncer-

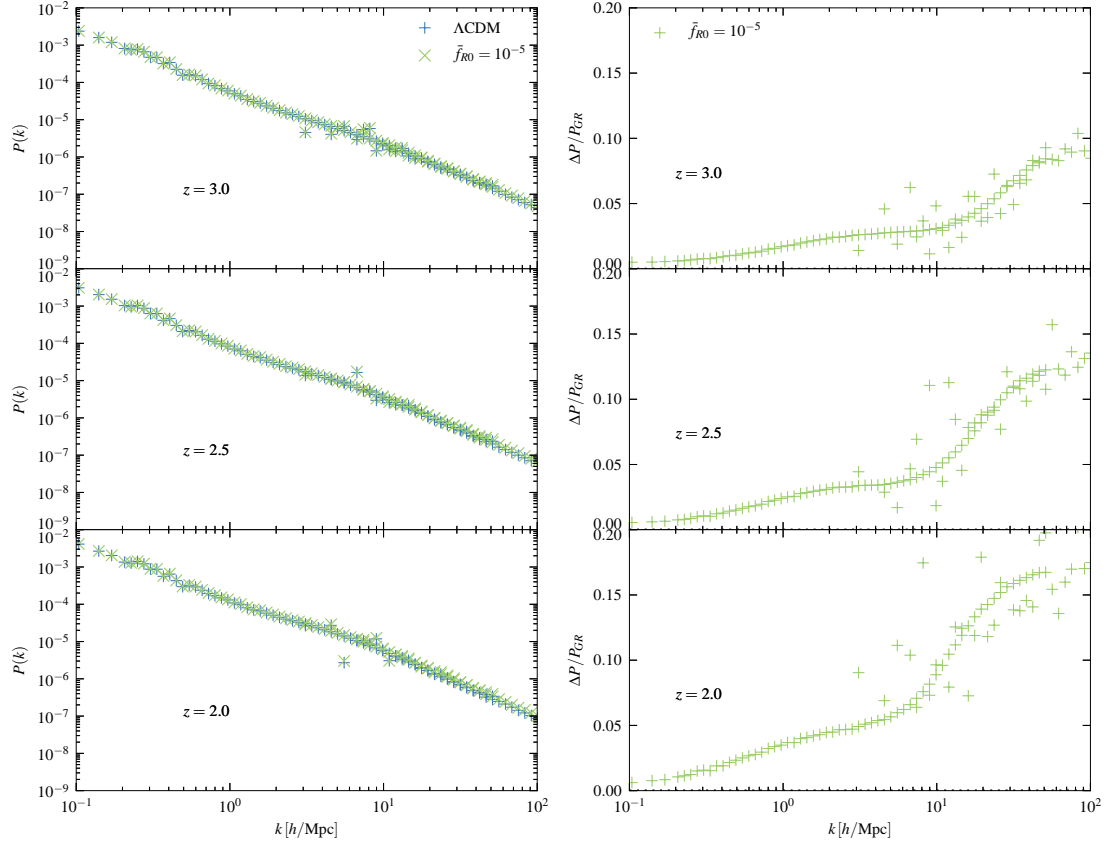


Figure 5.7: *Left Panel:* matter power spectrum for Λ CDM and $|\bar{f}_{R0}| = 10^{-5}$ at three different redshifts. *Right panel:* Corresponding relative difference in the power spectra $(P_{f(R)} - P_{GR})/P_{GR}$ between $f(R)$ and GR.

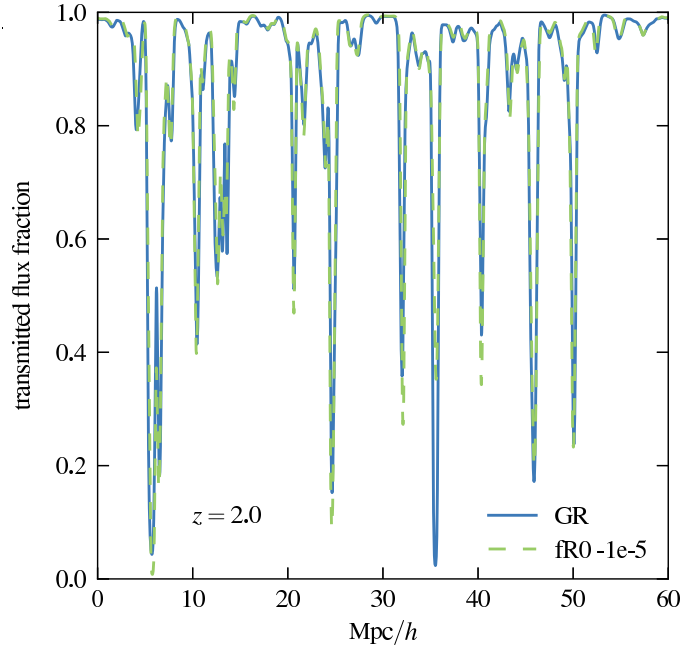


Figure 5.8: The transmitted flux fraction as a function of distance along an arbitrarily selected line of sight at $z = 2$. The results for a Λ CDM universe are shown in *blue*, those for a $f(R)$ cosmology in *green*.

tainties in Lyman- α forest studies and the already very tight constraints on the Hu & Sawicki (2007) model of $f(R)$ gravity from other observables, it will therefore be hard to get competitive constraints on $|\bar{f}_{R0}|$ using the flux PDF of the Lyman- α forest.

I arrive at a similar conclusion for the Lyman- α flux power-spectra obtained for the large simulation box: Figure 5.3 shows their absolute value for both $f(R)$ gravity and a Λ CDM cosmology as well as the relative difference between these models. The theoretical results from our synthetic spectra are again tuned to the mean transmission of Kim *et al.* (2007). For $z = 3$, the simulation values are compared to the observational results of McDonald *et al.* (2006), with the gray shaded area in the relative difference plot indicating their quoted errors.

As for the flux PDF, the discrepancy between simulations and observations at redshift $z = 3$ is quite large, in particular much larger than the errors given in McDonald *et al.* (2006). This might have its origin in systematic uncertainties which are not considered by the error-bars. Again, the difference between the two gravitational models is tiny, compared to the difference between observational data and the results from the simulations. Because the difference to GR is again smaller than or comparable to the error-bars of the shown observations, one needs to conclude that the Lyman- α flux power-spectrum is only mildly affected by $f(R)$ -gravity.

This is also particularly evident in the relative difference plots at the right hand side. The difference in the flux power-spectrum between $|\bar{f}_{R0}| = 10^{-5}$ and GR is

about 5% at maximum, considering redshifts $z = 2, 2.5$ and 3 . Normalizing the results of McDonald *et al.* (2006) to the Λ CDM outcome, it is obvious that the relative difference between the $f(R)$ simulation results and the fiducial model is consistent with the relative errors quoted for the individual k bins. The overall deviation over many bins and redshifts may be statistically significant. However, systematic effects would need to be better understood to obtain interesting constraints on \bar{f}_{R0} based on such observations.

To test if it is at all possible to constrain $f(R)$ gravity using the Lyman- α forest, I also run a set of simulations with smaller box size at equal mass and spatial resolution, for $|\bar{f}_{R0}| = 10^{-4}, 10^{-5}$ and GR. The power spectra and flux PDFs at redshift $z = 3$ are shown in Figure 5.4. For both power spectra and the PDFs, the results for GR and $|\bar{f}_{R0}| = 10^{-5}$, as well as their relative differences, are compatible with the values from the bigger simulation box shown in Figures 5.2 and 5.3. One can therefore conclude that the smaller box runs are sufficient for an analysis over the shown range of values. In the $|\bar{f}_{R0}| = 10^{-4}$ simulations, the flux power spectrum does not fit the observed values of McDonald *et al.* (2006) despite tuning the mean transmission. As the absolute value of the Lyman- α power spectrum is not known with great accuracy, one should not overestimate the, compared to the other gravitational models, smaller difference of the $|\bar{f}_{R0}| = 10^{-4}$ curve to the observations. Again, normalizing the GR results to the observations, one can compare the observational errors to the differences between $f(R)$ and a Λ CDM universe. At intermediate scales the difference between $|\bar{f}_{R0}| = 10^{-4}$ and GR is larger than for $|\bar{f}_{R0}| = 10^{-5}$. Nevertheless it does not exceed the 2σ relative error of the observations for individual k bins. Given that $|\bar{f}_{R0}| = 10^{-4}$ appears already clearly ruled out by other methods (Lombriser *et al.*, 2012a,b; Smith, 2009; Schmidt *et al.*, 2009; Dossett *et al.*, 2014), it does not seem that current Lyman- α data can add much new information here.

Figure 5.4 also shows the PDF of the transmitted flux for the three different gravity models. As for the power spectrum, the $|\bar{f}_{R0}| = 10^{-4}$ values do not fit the data much better than the other models at $z = 3$. Comparing relative errors to the difference between the models, one sees that the difference between $|\bar{f}_{R0}| = 10^{-4}$ and GR lies within the 1σ -error region for almost all values. Only between a transmitted flux fraction of 0.6 and 0.9 the difference is larger than 1σ and reaches about 2σ at maximum. The flux PDF does therefore also not seem to be very competitive with current observational data compared to other methods to constrain \bar{f}_{R0} .

In comparison to other uncertainties in the cosmological model, the impact of $f(R)$ gravity on Lyman- α flux power spectra or PDFs is fairly small, even if one considers quite extreme and already excluded values for $|\bar{f}_{R0}|$.

Figure 5.8 illustrates how small the modified gravity effect on the Lyman- α forest is. It displays the transmitted flux fraction along an arbitrarily selected line of sight for $f(R)$ and Λ CDM as a function of distance along this line. The positions of the absorption lines are the same for both models, as identical initial conditions have been used in both simulations. While there appear slight differences in the transmitted flux fractions for the individual absorption lines, no general pattern can be identified from a visual inspection.

Taking a more systematic approach, I used the code AutoVP (Davé *et al.*, 1997) to fit Voigt-profiles to the absorption lines of the synthetic spectra. The PDF of the line-width of the fitted Voigt-profiles is shown in the upper panel of Figure 5.5 for all lines with a neutral hydrogen column density $N_{\text{HI}} > 10^{13} \text{cm}^{-2}$ at redshift $z = 2$. As the lines almost perfectly overlap each other, it is perhaps not surprising that there is no significant difference in the line-width distributions between $f(R)$ gravity and a Λ CDM universe. The lower panel of the figure displays the normalized column density PDF of the absorption lines. As for the line-width, the difference between the curves for $|\bar{f}_{R0}| = 10^{-5}$ and the Λ CDM model is negligible.

The absolute values of the statistical Lyman- α measures depend on the observational value the mean transmitted flux is tuned to. To justify my previous analysis, I briefly show that the relative differences do not depend strongly on the actual value that is adopted. Figure 5.6 shows the relative difference in flux PDF and power spectrum between $|\bar{f}_R| = 10^{-5}$ and GR. Each line in the plot is tuned to a different mean τ , representing the observational data of Becker *et al.* (2013), Kim *et al.* (2007) and Faucher-Giguère *et al.* (2008). The figure shows that neither the relative difference in the power spectra nor the flux PDF do strongly depend on the choice of the tuning value for $z = 3$. As the analysis confirms, this does also hold for $z = 2$ and 2.5. One can therefore conclude that the relative differences can be explored safely despite the fact that the absolute values depend on the actual value used for the mean transmission.

To complement my analysis of the Lyman- α forest in the simulations, I also analyzed the total matter power spectra at different redshifts. Figure 5.7 shows these spectra for $|\bar{f}_R| = 10^{-5}$ and Λ CDM scenarios at redshifts $z = 2, 2.5$ and 3, as well as the relative difference between the models. Comparing the power spectrum enhancement to previous works, my results at redshift $z = 2$ are in good agreement with those of Li *et al.* (2013c). The evolution of the enhancement with time in our simulations is consistent with previous works, too (Li *et al.*, 2013c; Winther & Ferreira, 2014). This confirms that the $f(R)$ simulations feature an impact of modified gravity at the expected level, even though the effects on the Lyman- α forest properties are weak.

Comparing matter and flux power spectra at the same scale, the relative differences between $f(R)$ and GR are of similar size. The matter power spectra exhibit larger differences at smaller scales. There the Lyman- α flux power spectrum becomes, however, degenerate with uncertainties in the temperature of the intergalactic medium. Other gas properties like the temperature of gas in collapsed objects typically show $f(R)$ effects of order 30% in the unscreened regime (Arnold *et al.*, 2014). This also illustrates that the impact of $f(R)$ gravity on the Lyman- α forest is rather small in comparison. In order to constrain $f(R)$, it therefore appears more promising to focus on other measures of structure growth rather than the Lyman- α forest.

5.4 Summary and Conclusions

In this chapter, I analyzed the statistical properties of the Lyman- α forest and the matter power spectra in hydrodynamical cosmological simulations of $f(R)$ gravity. My simulations employed the Hu & Sawicki (2007) model and used the modified gravity simulation code MG-GADGET. For comparison, I also ran a set of simulations for a Λ CDM universe. The main findings can be summarized as follows:

- The PDF of the transmitted Lyman- α flux fraction is only mildly affected by $f(R)$ gravity. The maximum relative difference between $|\bar{f}_{R0}|=10^{-5}$ and GR is of order 7%. For $|\bar{f}_{R0}|=10^{-4}$ the difference grows to at most 10%. The simulation results do not fit the observational data of Kim *et al.* (2007) at all redshifts, regardless of the gravitational model. If the observations are normalized to the GR results from the simulations, the relative differences between the gravitational models do not exceed the 2σ relative error of the observations. For $z=3$, the Calura *et al.* (2012) data matches the simulation results at intermediate transmitted flux fractions much better. This highlights that the present observational data is relatively uncertain. At high transmissions there are also significant deviations.
- For the flux power spectra one arrives at similar results. The relative difference between the models reaches at most 5% for $|\bar{f}_{R0}|=10^{-5}$ and about 10% for $|\bar{f}_{R0}|=10^{-4}$. Again, the differences to GR for the stronger model are within the 2σ relative error of the observational data (McDonald *et al.*, 2006). Despite tuning the mean transmitted flux to the observational values, the power spectrum at $z=3$ does not accurately reproduce the observational data.
- There is no significant change in the shapes and abundances of absorption lines in $f(R)$ modified gravity: Both the column density and line width distribution functions based on Voigt profile fitting do not exhibit any systematic change.
- The relative differences between $f(R)$ and GR in the flux PDF and power spectra do not depend significantly on the observed mean transmission value to which the simulated spectra are scaled. The tuning affects only the absolute values of these statistical Lyman- α measures.
- The matter power spectrum shows an enhancement in $f(R)$ gravity which grows with time. The amplitude of the effect and the relative difference to GR is consistent with previous works. These relative changes in the matter power spectrum are of comparable magnitude as the changes in the Lyman- α forest flux power spectrum at the same scale. Note, however, that the enhancement of the matter power spectrum continues to grow towards low redshift where it is no longer probed by the Lyman- α forest. Also, note that a much stronger influence of $f(R)$ has been found for other gas properties like the gas temperature in collapsed objects in the unscreened regime as has been reported in Arnold *et al.* (2014).

All in all I arrive at the conclusion that the impact of $f(R)$ gravity on the Lyman- α forest is small. The relative differences in flux PDFs and flux power spectra are only of the order of 5%. Even for likely excluded models, like $|\bar{f}_{R0}| = 10^{-4}$, the changes in the statistical Lyman- α forest properties do not exceed the relative errors of available observations in individual flux or wavenumber bins. Using the full data over a range of redshifts a detection of modified gravity effects could probably be statistically significant due to its clearly defined signature. However, currently, systematic effects do not seem to be understood at the required level to get competitive constraints in practice. One can therefore conclude that Lyman- α forest properties are of limited discriminative power to constrain $|\bar{f}_{R0}|$ at the moment. The remarkable robustness of the forest statistics has however also advantages. Given that the considered gravitational models have a negligible impact on the Lyman- α forest compared to other cosmological and astrophysical uncertainties, it may not be necessary to consider $|\bar{f}_{R0}|$ as an additional parameter in constraining cosmological parameters based on the Lyman- α forest.

6 Zoomed cosmological simulations in $f(R)$ -gravity ¹

6.1 Introduction

In this section, I present the first simulations of Milky Way sized objects using high-resolution cosmological zoom simulations of $f(R)$ -gravity. They are carried out employing the upgraded version of MG-GADGET with the local time-stepping approach described in Section 3.2.3 to resimulate a set of seven halos from the Aquarius project (Springel *et al.*, 2008). The analysis focuses on the impact of modified gravity on density profiles, gravitational forces, circular velocities as well as velocity dispersions. In addition, I derive an analytic estimate for the $f(R)$ -force profile in NFW-halos (Navarro *et al.*, 1997) and compare this theoretical approximation to the simulation results.

6.2 Simulations and methods

Using the same initial conditions as the Aquarius project (Springel *et al.*, 2008; Marinacci *et al.*, 2014) I carry out for the first time zoom simulations in $f(R)$ -gravity of a set of 7 Milky Way sized halos (A, B, C, D, E, G and H in the Marinacci *et al.* 2014 terminology) employing the cosmological simulation code MG-GADGET. For all halos I simulate the evolution of the matter distribution for $\bar{f}_{R0} = -10^{-6}$ (referred to as F6), $\bar{f}_{R0} = -10^{-7}$ (F7), and for the Λ CDM cosmology as a reference. In the simulations, a $\Omega_m = 0.25$, $\Omega_\Lambda = 0.75$, $h_0 = 0.73$ cosmology was used. The mass resolution in the zoomed region reaches $3.14 \times 10^6 M_\odot$.

To identify the center of the simulated halos and subhalos, i.e. the minimum of the gravitational potential of bound structures in the simulation box, the SUBFIND algorithm (Springel *et al.*, 2001) inlined in P-GADGET3 was used. Besides the standard outputs of an N-body code (particle positions, masses, velocities, GR-gravity accelerations) I also include in the output the modified gravity acceleration and the scalar field itself, interpolated from the mesh points of the AMR grid to the particle positions.

¹The results and large parts of the text in this section have already been published in Arnold *et al.* (2016).

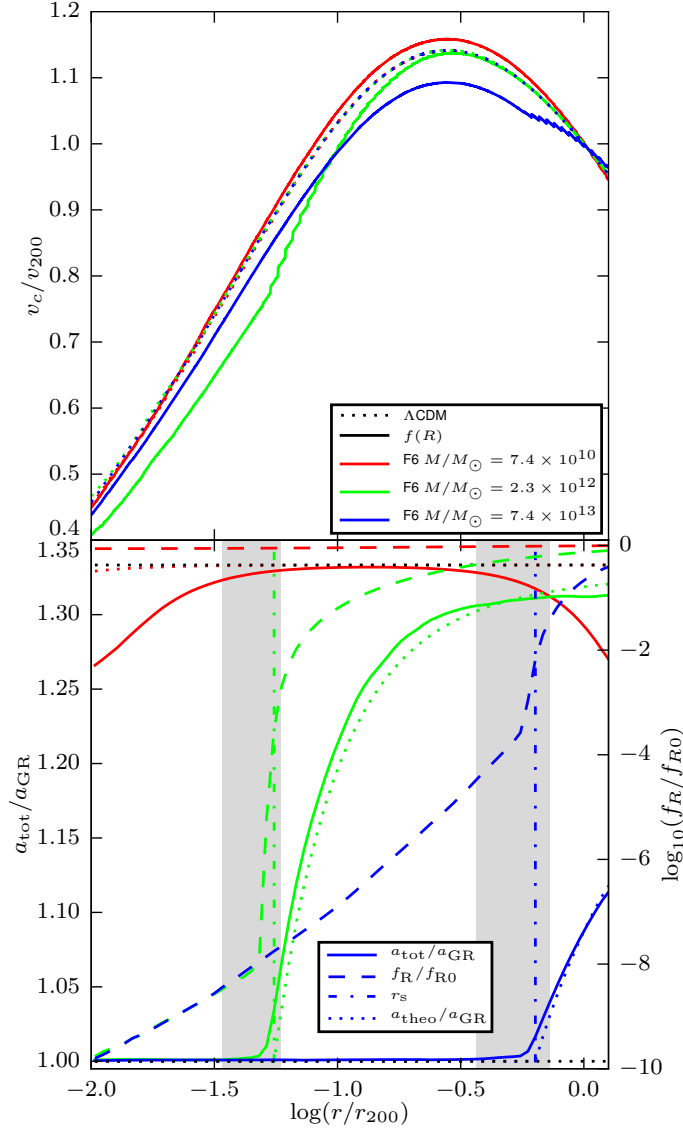


Figure 6.1: *Upper panel:* The circular velocity profiles for ideal NFW halos of three different masses but equal concentration $c \approx 10$ for $f_{R0} = -10^{-6}$ (solid lines) and Λ CDM (dotted line) scaled with the circular velocity at r_{200} . The velocities are derived from the enclosed masses, taking into account the increased gravitational forces for $f(R)$ gravity in unscreened and partially screened regions. *Lower panel:* The solid lines show the ratio of total acceleration to GR acceleration for the three different halos in $f_{R0} = -10^{-6}$ cosmology. Dotted lines show the theoretical expectations for this force ratio. The corresponding values of the scalar field are plotted as dashed lines. The theoretical values for the radius at which one expects screening to set in (obtained from Eqn. 2.100), r_s , are shown as dashed-dotted lines for the heavy and the intermediate mass halo. For the least massive object, this radius is zero. The grey shaded regions show an estimate for the uncertainty of this radius. The highest and lowest allowed values for $a_{\text{tot}}/a_{\text{GR}}$ of $4/3$ and 1 , respectively, are indicated by the black dashed lines.

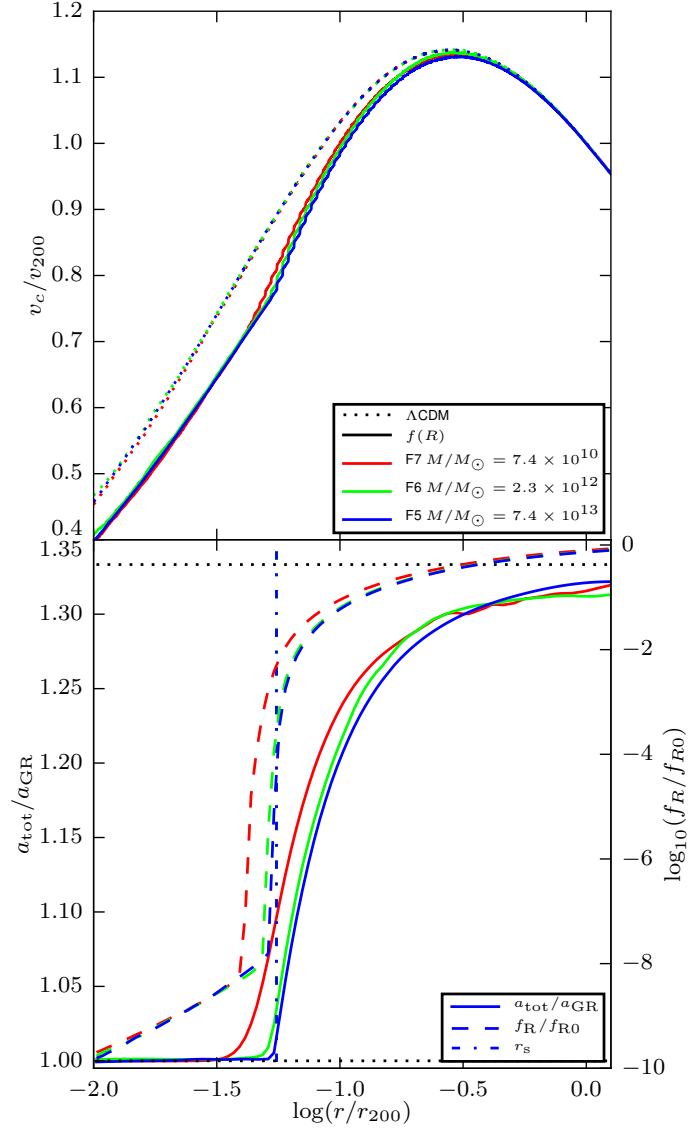


Figure 6.2: Same as Figure 6.1, but with the masses and the background values of the scalar field f_{R0} scaled such that the screening radius r_s in units of r_{200} is constant for all three halos.

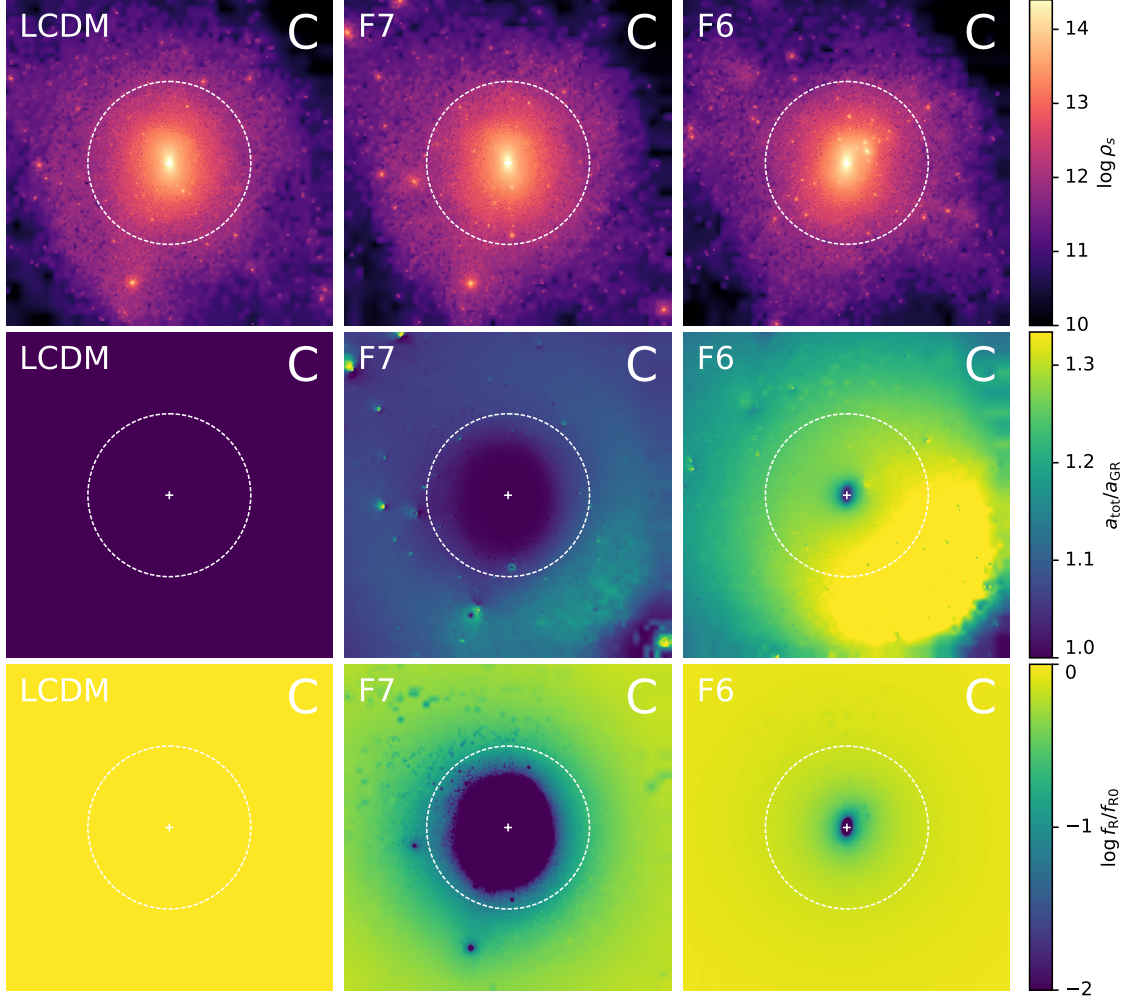


Figure 6.3: Thin slice projections through the central region of the C halo for the GR (*left panels*), the $|\bar{f}_{R0}| = 10^{-7}$ (*center panels*) and the $|\bar{f}_{R0}| = 10^{-6}$ (*right panels*) simulation. The *top panels* show the density field, the *middle panels* the modified gravity to standard acceleration ratio and the *bottom panels* the scalar field. The cross indicates the gravitational potential minimum of each halo obtained from SUBFIND and the *dashed white circles* display $r_{200 \text{ crit}}$.

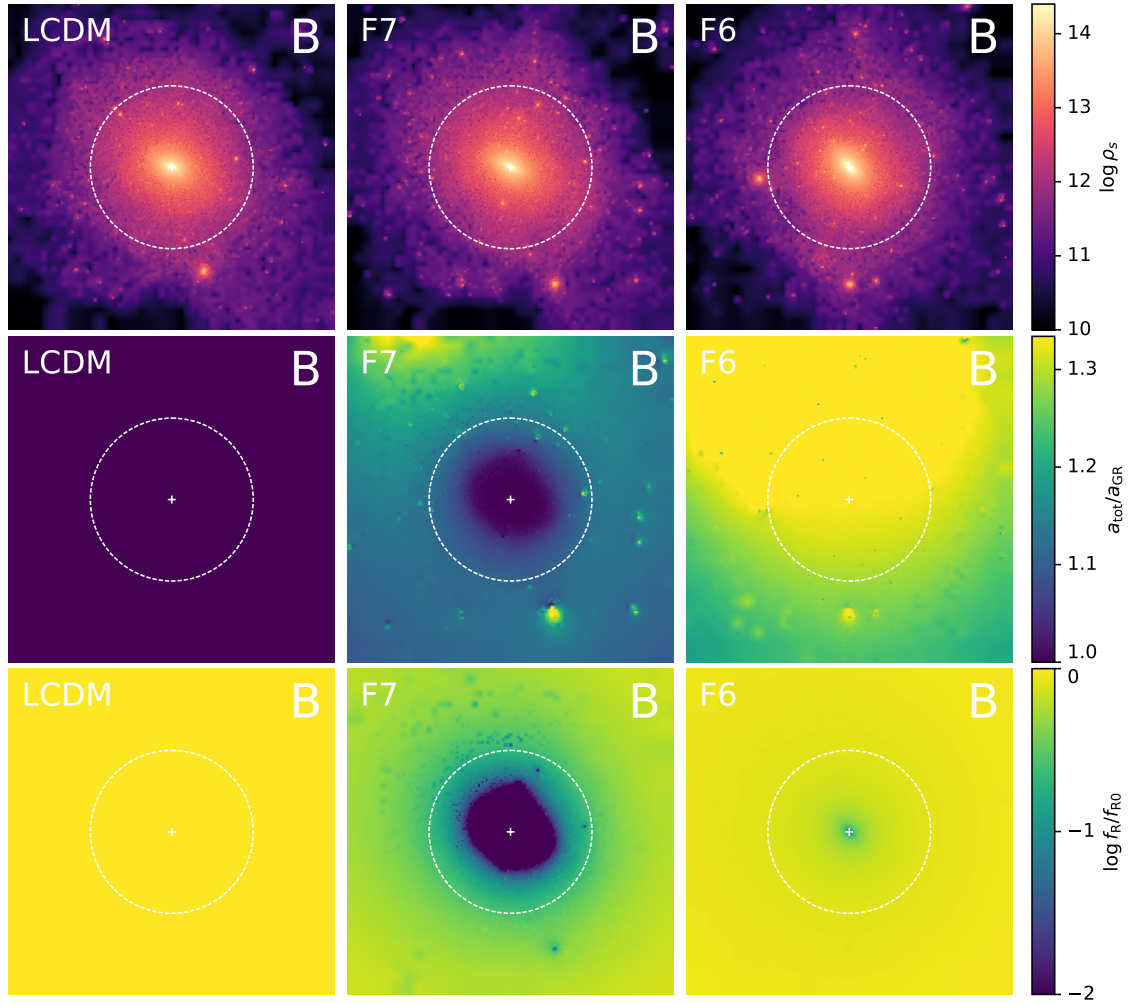


Figure 6.4: Same as Figure 6.3 but for the B halo.

6.3 Results

6.3.1 Ideal NFW halos

The theoretical estimates derived in section 2.3.8 assume perfect spherical symmetry. This is of course not true for the simulated halos from the Aquarius suite. To cross-compare the accuracy of the simulations and the theoretical approximations in a more controlled environment first, I set up initial conditions for a collection of three perfectly symmetric halos with a NFW density profile. The halos have equal concentration of $c \approx 10$ but different mass. Each object is situated in a cubic box of 100 Mpc side-length and constant background density. The halos serve as initial conditions for MG-GADGET to obtain circular velocity profiles, accelerations and f_R -profiles based on the code's multi-grid $f(R)$ solver.

Figure 6.1 displays the results of these tests. The upper panel shows the circular velocity profile in units of $v_{200} \equiv \sqrt{GM_{200}/r_{200}}$ for $f_{R0} = -10^{-6}$ as well as for a Λ CDM reference simulation for each of the halos. The values for the velocity profiles are obtained from the enclosed mass but with an additional boost accounting for the – in unscreened regions – higher accelerations in $f(R)$ -gravity $v_c = \sqrt{GM/r} \times \sqrt{a_{\text{tot}}/a_{\text{GR}}}$. In Λ CDM, the velocity profiles for the three halos overlap almost perfectly, which is expected due to the self-similarity between halos of equal concentrations. This self-similarity is broken in modified gravity because of the scale introduced by chameleon screening.

If the object is massive enough, the gravitational potential will drop below a certain threshold at the screening radius r_s , causing the chameleon screening to set in. As a result, the fifth force quickly decreases to zero. This is exactly what one can see in Figure 6.1. The circular velocity profiles in the upper panel do not coincide anymore in $f(R)$ cosmology. For the two more massive objects, there is a tilt in the velocity curves at a certain radius depending on the mass of the object causing the circular velocities to drop with increased screening. Having a look at the lower panel, this can be easily explained by the force ratio of total-to-GR force. For the least massive halo, the force ratio stays roughly constant at the theoretically expected value of $4/3$ (indicated by the black dotted line) because even in the center the gravitational potential is not deep enough to trigger screening. The slight deviations at small radii are due to the lack of resolution in the AMR grid of the multigrid solver (the size of the grid cells is of the order $10^{-2}r_{200}$ for this object). At large radii, GR- and $f(R)$ -forces are not necessarily aligned anymore, which can cause a smaller force ratio as well.

The force ratio of the intermediate mass object is very close to the theoretically expected value for unscreened regions in the outer part as well. But moving inwards, the ratio starts to decrease and quickly drops to unity. The radius at which the fifth force becomes negligible is almost exactly at the theoretically predicted value for r_s , which was calculated from Eqn. (2.100). The grey shaded regions indicate the uncertainty range of this radius. The errors were obtained by varying the outer integration bound R in (2.100) from $r_{200}/2$ to $2r_{200}$. Comparing the force ratio

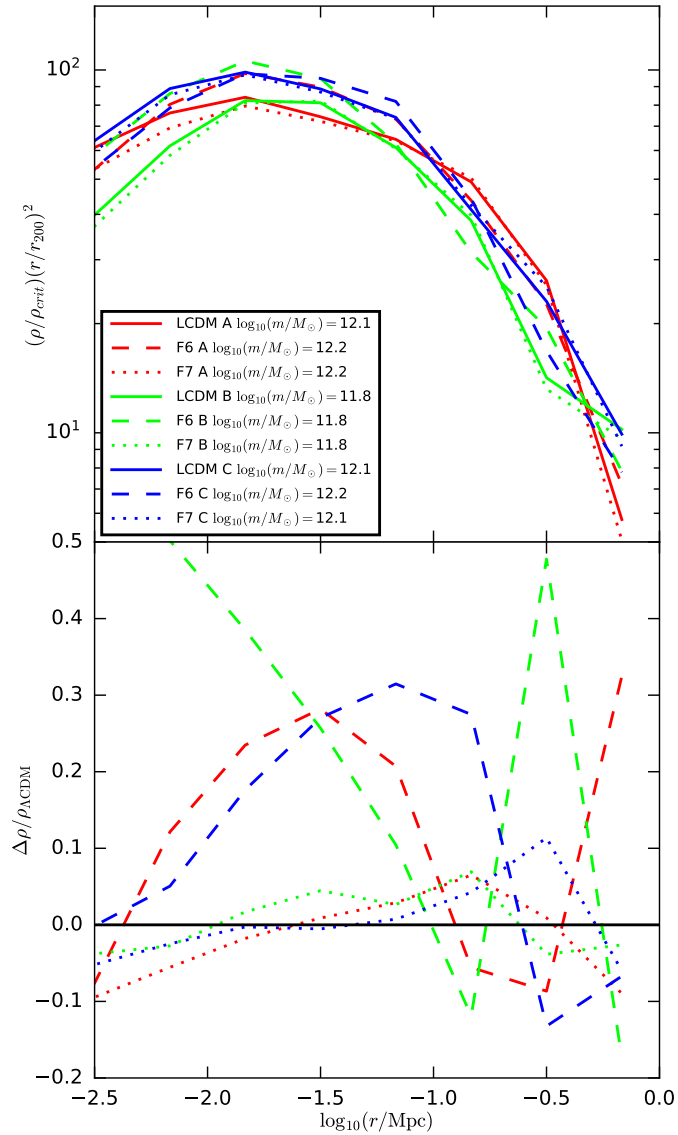


Figure 6.5: Density profiles of the Aquarius halos A (red lines), B (green lines) and C (blue lines) for the three cosmological models Λ CDM (solid lines), F6 (dashed lines) and F7 (dotted lines). *Upper panel:* The density relative to the critical density multiplied by $(r/r_{200})^2$. *Lower panel:* Relative difference between the densities in $f(R)$ cosmology and the corresponding Λ CDM values. The solid black line indicates equality.

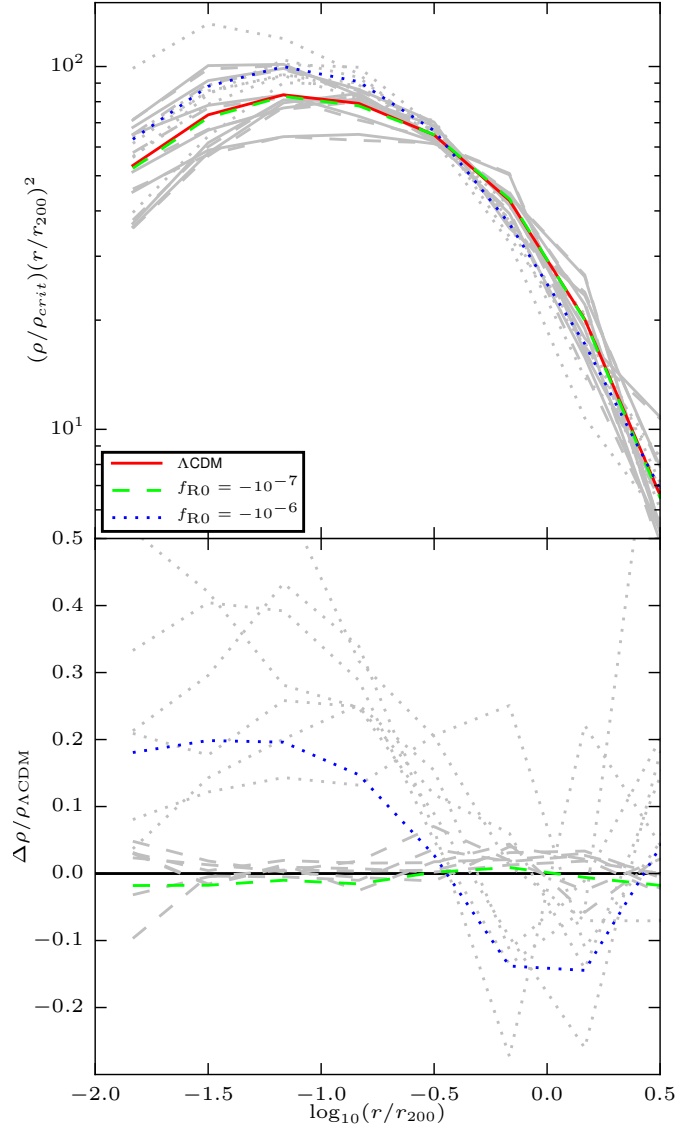


Figure 6.6: *Upper panel:* Stacked density profiles for all simulated Aquarius halos for ΛCDM (red solid line), F6 (green dashed line) and F7 (blue dotted line) cosmology. *Lower panel:* Relative difference of the stacked density profiles to the ΛCDM values. The grey lines indicate the densities of the individual halos.

of the simulation with the theoretical estimate calculated from Eqn. (2.99) shows remarkably good agreement, too. The largest halo is already partially screened at the outermost radius shown in Figure 6.1. The gravitational potential well of the object is so deep that it crosses the screening threshold already in the outskirts of the halo. Again, both the screening radius and the force ratio show a high level of agreement with the theoretical expectations. From Figure 6.1, one can also see that the value of the scalar field drops by several orders of magnitude at the screening radius, underlining its highly nonlinear behaviour.

Next, I investigate if the self similarity of the DM halos in the Λ CDM cosmology can be restored in $f(R)$ -gravity by a suitable rescaling of the background field amplitude f_{R0} . To this end, I scale f_{R0} according to Eqn. (2.103) such that the ratio r_s/r_{200} of the high and low mass halos are the same as for the intermediate mass object. I also use the same concentration. Figure 6.2 displays the circular velocity profiles and the total-to-GR force ratio for the objects. In contrast to the previous plot, a good agreement of the $f(R)$ circular velocities can be observed. The force ratios and f_R profiles are very similar as well. Only the lowest mass halo shows a slight deviation from the others which can again be explained by the worse resolution of the AMR-grid relative to the halo size in the center of the object. The screening radius is – by construction – exactly the same. Knowing the impact of $f(R)$ modified gravity on a certain property for a given value of f_{R0} , it is thus possible to predict how the property would change for a different f_{R0} by scaling all masses according to Eqn. (2.103).

6.3.2 The Aquarius halos

The ideal NFW halos analyzed in the previous section have identical density profiles in the $f(R)$ and Λ CDM cosmological models. Since $f(R)$ gravity already modifies the gravitational forces during structure formation, this will in general not be the case for the outcome of self-consistent halo formation. The halos will furthermore not be completely spherically symmetric as one can see from Figures 6.3 and 6.4. The halos' screened regions visible as the dark blue regions in the scalar field projections are consequently not spherical. Moreover, substructure can cause screened bubbles in unscreened regions (bright yellow areas) around the halo (see e.g. the bottom center panel of Figure 6.3). Comparing Figures 6.3 and 6.4 it is obvious that the size of the screened region relative to r_{200} depends not only on f_{R0} but also on the mass of the object. As expected from theory, the less massive halo B features a much smaller screened region in the center than the halo C. Let me now analyze the properties of the Aquarius halos in a more quantitative way.

Figure 6.5 shows the density profiles of the Aquarius halos A, B and C, at $z = 0$, simulated in the $f_{R0} = -10^{-6}$ (F6), $f_{R0} = -10^{-7}$ (F7) and Λ CDM cosmological models. The upper panel displays the density profiles relative to the critical density multiplied by $(r/r_{200})^2$. The lower panel shows the relative difference of the density curves in $f(R)$ gravity relative to the GR runs. Clearly, the density profiles in F6 change significantly compared to the cosmological standard model. The density in

	M_{200} [$10^{12} M_{\odot}$]	V_{\max} [km/s]	r_{\max} [kpc]	c
GR A	1.846	209.13	30.46	15.24
F7 A	1.954	206.52	40.79	11.95
F6 A	2.020	229.19	41.87	12.72
GR B	0.821	158.62	43.72	9.10
F7 B	0.863	160.54	42.78	9.36
F6 B	0.919	182.22	38.92	11.22
GR C	1.772	223.07	33.76	14.78
F7 C	1.811	222.08	32.96	15.01
F6 C	2.294	241.75	48.01	11.89
GR D	1.800	204.78	57.43	8.97
F7 D	1.871	206.28	56.46	9.16
F6 D	2.251	224.31	56.70	9.78
GR E	1.192	179.95	57.26	8.08
F7 E	1.229	183.08	58.94	8.00
F6 E	1.324	205.66	42.38	11.55
GR G	1.034	154.61	82.35	5.21
F7 G	1.077	154.02	60.11	6.81
F6 G	0.984	179.41	34.46	12.22
GR H	0.852	177.20	19.84	18.75
F7 H	0.910	176.77	19.60	18.89
F6 H	0.963	202.97	17.92	22.56

Table 6.1: v_{\max} and r_{\max} for the Aquarius halos simulated in the models Λ CDM, F6 and F7. The values for v_{\max} , r_{\max} and c are obtained with the SUBFIND algorithm and neglect fifth force contributions. c is the traditional concentration parameter describing the shape of the density profile.

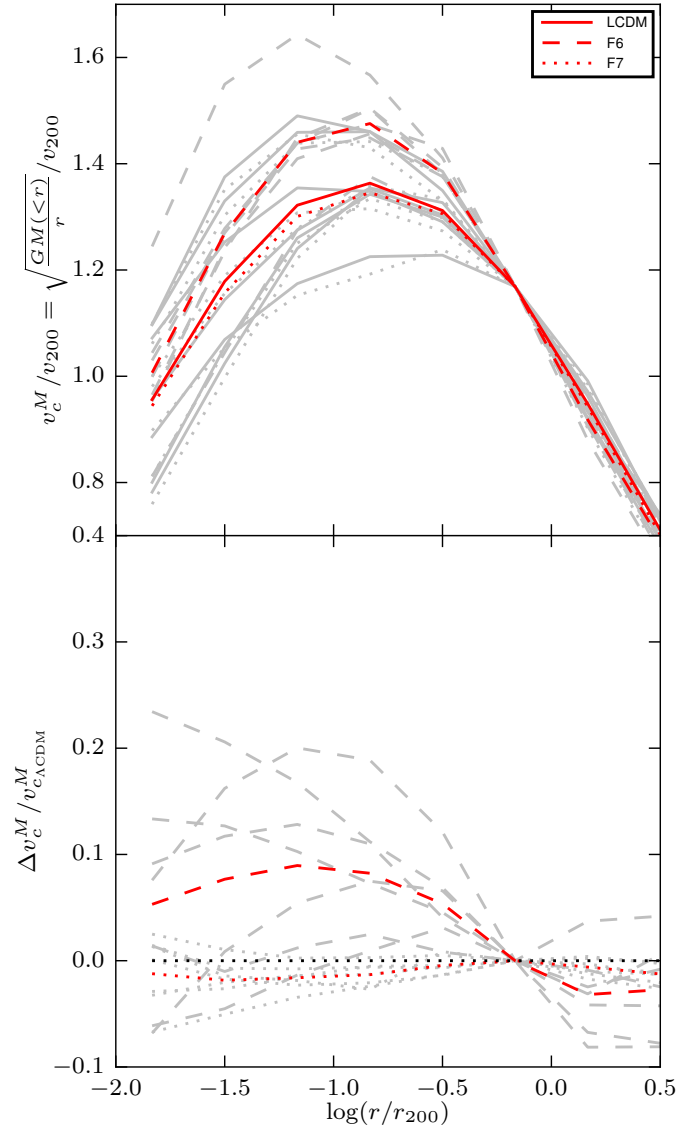


Figure 6.7: *Upper panel:* Stacked circular velocity profiles for the simulated Aquarius halos calculated only based on the enclosed masses in units of v_{200} as a function of r_{200} for Λ CDM (solid line), F6 (dashed line) and F7 (dotted line). *Lower panel:* Relative difference in the circular velocity of the $f(R)$ models compared to Λ CDM. The *dotted black line* indicates equality. The grey lines in the background show the profiles for the individual halos.

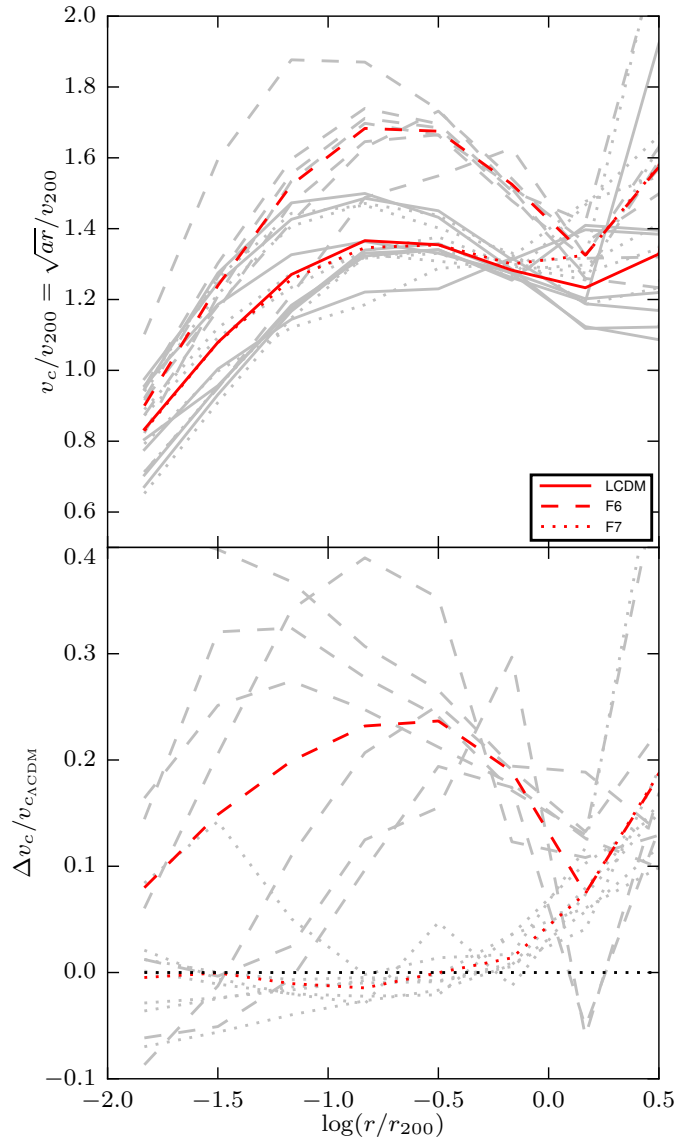


Figure 6.8: Same as Figure 6.7 but with the circular velocities obtained from the total accelerations taking increased gravitational forces in unscreened regions for the $f(R)$ models into account.

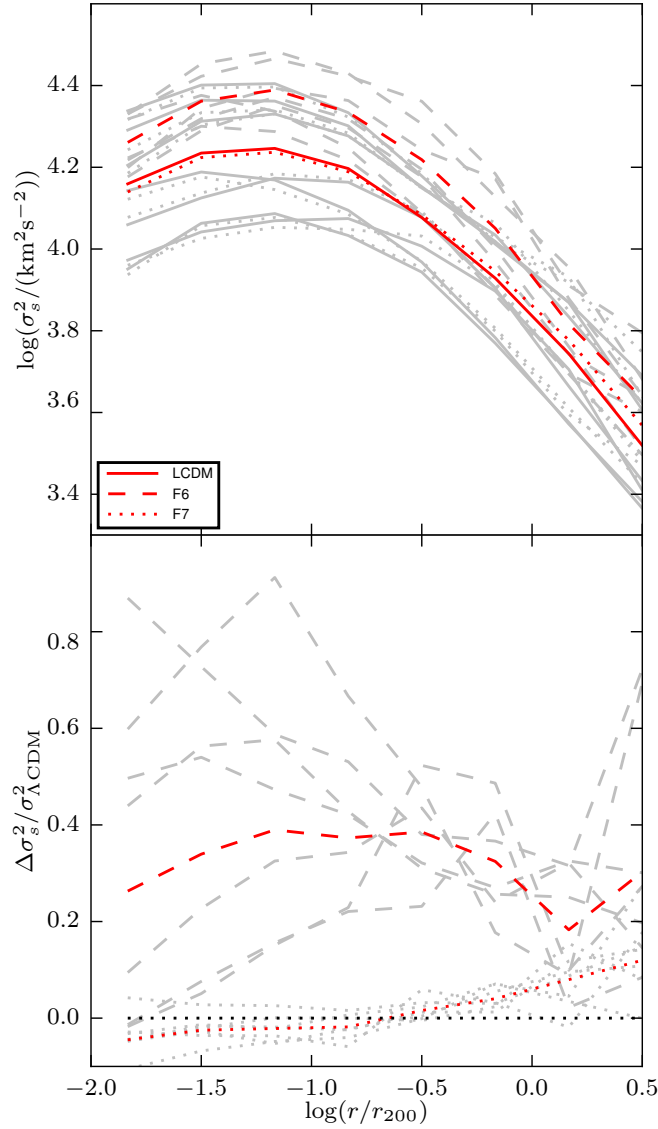


Figure 6.9: *Upper panel:* Stacked velocity dispersion profiles for the simulated Aquarius halos for the ΛCDM (solid line), F6 (dashed line) and F7 (dotted line) cosmological models. For the $f(R)$ models the velocity dispersions were scaled according to $\sigma_s^2 = (M_{GR}/M_{f(R)})^{2/3}\sigma^2$ to filter effects due to the mass difference of the halos in the different models. *Lower panel:* Relative difference in scaled velocity dispersion between $f(R)$ gravity and ΛCDM . The black dotted line indicates equality. The grey lines in the background show the values for the individual halos.

the outer region decreases by about 10% while it increases by roughly 30% in the inner part. The transition radius depends on the mass of the halo. For F7 the changes are less significant. The density change in the C halo is about 10% in the outer region but it is hard to tell if this is really a systematic effect or caused by small timing differences in halo assembly.

To make a robust quantitative statement about the changes in the halo densities, the density profiles of all simulated Aquarius halos were stacked. The profiles for the three cosmological models as well as the relative difference between $f(R)$ and Λ CDM are illustrated in Figure 6.6. The grey lines in the background show the values for the individual halos. As already expected from the previous plot, the change in the density is quite large for the F6 model. Around r_{200} the density is about 10 – 15% lower than in a Λ CDM cosmology. At $\log_{10}(r/r_{200}) \approx -0.5$, the stacked density ratio crosses equality and reaches a maximum of about 20% difference for the inner part of the objects. This is easily explained. The higher gravitational forces in unscreened regions in $f(R)$ gravity move mass from the outer to the inner part of the halos, thereby steepening their density profiles. The difference of the stacked density profiles in the Λ CDM and F7 models is consistent with zero. This shows that Milky Way sized halos are largely screened in F7. Keeping in mind that the F6 model passes present constraints on f_{R0} , I would like to stress that viable $f(R)$ models can hence change the density profile of Milky Way sized dark matter halos by about 20%.

Systematic differences in the density profiles are likely to affect the concentrations of halos. To investigate if the concentration shows systematic changes in $f(R)$ gravity as well, NFW-profiles (Navarro *et al.*, 1997) were fitted to the density of the simulated halos for each of the three simulated models. Unfortunately, I found that the concentrations obtained from the fits show a relatively large residual dependence on the radial fitting range, resulting in sizable random scatter for my small halo sample. It is thus hard to judge on this basis if $f(R)$ gravity influences the concentration parameter in a significant way. As an alternative to profile fitting, I also employed another technique and obtained the concentration from the maximum of the circular velocity curve in terms of v_{\max} and r_{\max} (Springel *et al.*, 2008):

$$\delta_c = 7.213 \delta_V = 7.213 \times 2 \left(\frac{v_{\max}}{H_0 r_{\max}} \right)^2, \quad (6.1)$$

$$\delta_c = \frac{200}{3} \frac{c^3}{\log(1+c) - c/(1+c)}.$$

The results are summarized in Table 6.1, where v_{\max} and r_{\max} are obtained from the density profile directly through the SUBFIND algorithm. These values can be used to calculate the concentration parameter of the NFW-profile. In computing v_{\max} the force modifications which occur in unscreened regions in $f(R)$ -gravity, i.e. v_{\max} are ignored and r_{\max} are completely determined by the density profile, as appropriate for measuring its concentration. They should not be confused with the velocities shown in Figure 6.8. The numbers in Table 6.1 are rather connected to the curves

in Figure 6.7.

Comparing the concentration c of the objects simulated in F6 and GR, one finds that the concentrations are increased for the B, D, E G and H halo. For the A and the C halo, however, the concentration parameter decreases in $f(R)$ gravity compared to Λ CDM. One can thus conclude that there appears to be a slight trend to higher concentrations in $f(R)$ gravity, but a much larger number of halos would be needed to establish this finding robustly. It would also be important to carefully select sufficiently relaxed halos (e.g. as in Neto *et al.*, 2007) to avoid influences from mergers or large substructures. Because the effects in F7 are weaker, it is even harder to demonstrate if and how the concentration changes for this model.

Figure 6.7 shows stacked circular velocity profiles for the Aquarius halos in F6, F7 and GR as well as the relative differences between the modified gravity models and Λ CDM. The grey lines in the background display the velocity profiles of the individual halos. For this plot, the velocities were obtained from the enclosed masses using the standard relation for Newtonian gravity, hence neglecting any $f(R)$ effects other than those encoded in the mass distribution. In order to clearly separate effects which are induced by the slightly higher masses in $f(R)$ gravity, the velocities are scaled with $v_{200} \equiv (GM_{200}/r_{200})^{1/2}$. The velocity curves are therefore a direct measure of the mass profile and useful to determine, for example, the concentration of the mass profile in the standard way. It is not surprising that the relative difference between the F6 model and GR is of order 10% compared to a 20% difference in density in the inner part of the halo ($v \propto \sqrt{M}$). In contrast to the density, the velocity does not drop significantly below the Λ CDM value in the outer regions since the velocities see the cumulative mass profile which includes the higher density in the center. The slightly lower values outside of r_{200} are due to the rescaling with v_{200} . Since the density profile does not change noticeably in F7 the change in circular velocities is negligible as well.

As a cautionary remark I would like to add that the velocities shown in Figure 6.7 should not be confused with observable circular velocities. For those, the differences in the accelerations between the different models must be included in the analysis. This was done for Figure 6.8, where stacked circular velocity profiles obtained from the total accelerations are shown. In the upper panel, the absolute values of the velocities are displayed for the three simulated models, the lower panel shows the relative differences of $f(R)$ gravity to GR. The velocities in the F6 model are significantly higher compared to standard gravity and to the previous plot. This is easily explained. In addition to the higher densities in the inner region of the halos, higher gravitational accelerations in unscreened regions force the DM particles in the simulation to orbit faster in order to prevent infall. As a result, the circular velocities are increased by up to 25% compared to GR in unscreened regions. Although a 25% difference in the velocity profile for an allowed $f(R)$ model seems large, one has to keep in mind that the effects will be at least partially degenerate with (the quite uncertain) baryonic physics (Vogelsberger *et al.*, 2014a; Marinacci *et al.*, 2014) and uncertainty in the halo mass. Also, the error bars of the current observational constraints (Avila-Reese *et al.*, 2008; Hall *et al.*, 2012; McGaugh, 2012) allow a broad

range of velocities. It will therefore be hard to constrain f_{R0} relying on the rotation curves of Milky Way sized objects.

For the F7 model, the circular velocities stay unchanged in the inner region of the halo because the $f(R)$ modifications to gravity are screened by the chameleon mechanism. At around $0.5 r_{200}$ the relative velocity difference increases and reaches 20% at $3 r_{200}$. This can be explained by two mechanisms. On the one hand, the halo becomes unscreened in the outer parts due to the shallower gravitational potential. The gravitational forces are thus by a factor of 4/3 higher and increase the velocities even if the density is the same. On the other hand, all velocities increase outside r_{200} because the particles start to see other objects and are not in virial equilibrium. In combination with higher forces, this adds another boost to the velocities.

Figure 6.9 shows the stacked velocity dispersion profiles for F6, F7 and GR (upper panel) as well as the relative difference of the modified gravity values to Λ CDM (lower panel). Since the difference in halo mass between the models for a given object (see Table 6.1) would also lead to differences in the velocity dispersion, it was scaled according to $\sigma_s^2 = (M_{\text{GR}}/M_{f(R)})^{2/3} \sigma^2$ for the $f(R)$ curves to account for the mass difference. The scaled velocity dispersion shown in the plot is therefore a measure how the velocity dispersions of halos of a given mass would change in $f(R)$ -gravity. For the F6 run, one finds the velocity dispersions increased by about 40% in the inner part ($-1.5 < \log_{10}(r/r_{200}) < -0.5$) which is again a result of the higher densities in this central part of the halo and the increased gravitational forces. In the outer regions, the cumulative mass profile stays unchanged compared to GR and thus only the 4/3 enhancement of the forces contributes to the about 30% higher velocity dispersion. Outside r_{200} , the halo shows again larger differences between the models due to a lack of virialisation.

The 40% difference between the $f(R)$ and Λ CDM cosmological models is slightly higher than the values for unscreened halos of about 30% reported in Schmidt (2010), Lam *et al.* (2012), Arnold *et al.* (2014) and Gronke *et al.* (2015). There are several reasons for this difference. First, all of these other works used cosmological simulations with mass resolutions poorer by factors 10 – 100 (relative to the mass of the considered object) compared to the high resolution simulations in this work. They were therefore most likely not capable of capturing the increased density in full in the inner region of the halos. Second, the previous works either present the averaged velocity dispersion of the whole object or do not show the profiles in the inner part. For both cases, the velocities will be dominated by the outer regions which obey a smaller velocity dispersion. It is obvious that for the weaker F7 model, the velocity dispersion stays unchanged in the central region because the fifth force is again screened. Further out, the difference to GR grows to 10% at r_{200} .

In the following I like to extend my comparison of the theoretically predicted screening radius and fifth force (see section 2.3.8) to the simulated Aquarius halos. In contrast to perfectly symmetric NFW profiles the simulated halos are ellipsoidal and feature substructures which breaks spherical symmetry. My goal is to find out if the theoretical approximations are nevertheless applicable and reasonably accurate for realistic halos. The upper panel of Figure 6.10 shows the circular velocity profiles of

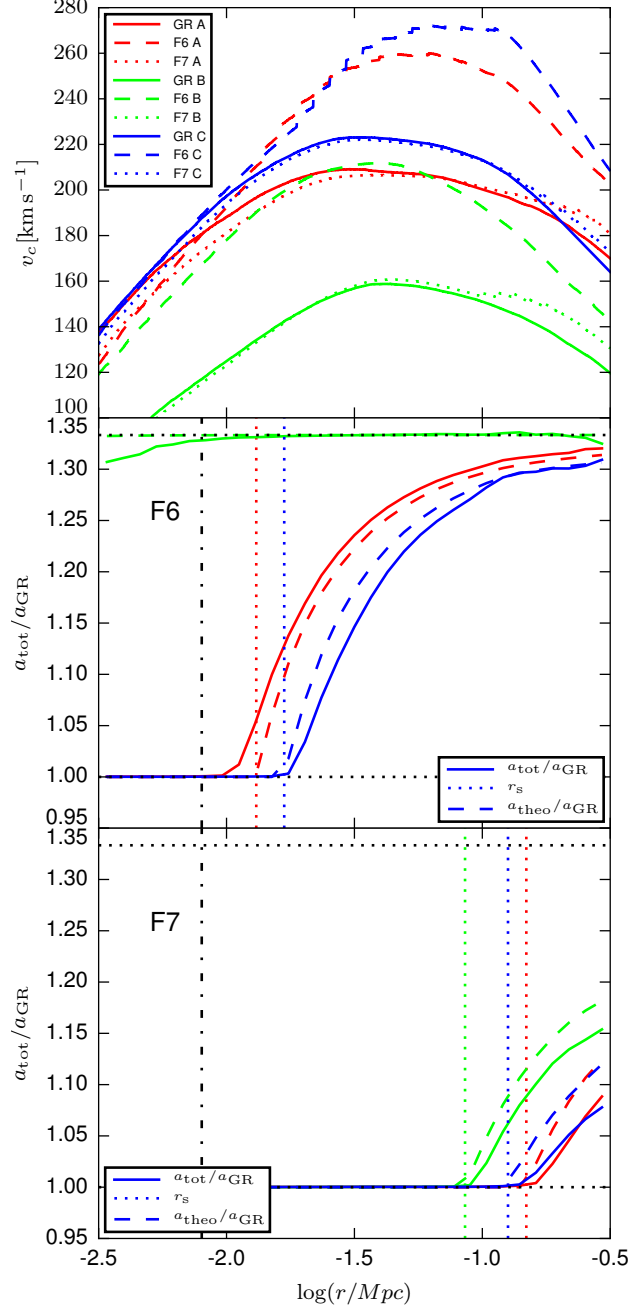


Figure 6.10: Circular velocity and acceleration profiles for the halos A (red lines), B (green lines) and C (blue lines). *Upper panel:* Circular velocity profiles for Λ CDM (solid lines), F6 (dashed lines) and F7 (dotted lines) taking the increased accelerations due to modified gravity fifth forces in the $f(R)$ models into account. *Center panel:* Ratio of the total force to GR force for the three halos in the F6 cosmology. The results from the simulations are shown as solid lines. Dashed lines indicate the theoretical expectations. The predicted screening radii, r_s , are shown as vertical dotted lines. The two black horizontal dotted lines indicate equality and the maximum value for the force ratio of $a_{\text{tot}}/a_{\text{GR}} = 4/3$. For reference, the distance of the Sun from the Galactic center is indicated by the vertical dashed dotted line. *Lower panel:* Same as the center panel but for the F7 cosmology.

the Aquarius halos A, B and C, for F6, F7 and GR. The profiles are, as in Figure 6.1, obtained from the enclosed mass with an additional factor for the increased forces in $f(R)$ -gravity. The small steps visible in some of the $f(R)$ profiles are due to the binning of the acceleration ratio. For the A and the C halo, the velocities are increased by about 20–30% with respect to GR in the outer region. Moving further in, the difference between the $f(R)$ and Λ CDM curves decreases due to chameleon screening until they almost match. The B halo has a slightly lower mass. Its velocity curve is by 20–30% higher than the curve obtained from the GR simulation over the whole range of radii shown in the plot. This suggests that this halo is largely unscreened.

These results are confirmed by the acceleration ratios for the F6 model displayed in the middle panel. For the two massive halos, the acceleration ratio drops to unity at $r \approx 0.02$ Mpc. Inside this radius, the $f(R)$ modifications to gravity are screened by the chameleon mechanism. For the B halo, the acceleration ratio stays at the theoretical maximum of 1.33 over almost the whole range shown in the plot. Only in the innermost part there is a slight deviation which could naively be interpreted as the onset of screening, but is more likely an effect caused by the lack of resolution of the AMR-grid in the central region of the least massive object.

In the weaker F7 model, all three objects are almost totally screened. The velocity profiles coincide with the Λ CDM curves. Only in the very outer region, chameleon screening breaks down and the velocities in F7 are increased with respect to GR. Again, the acceleration ratios confirm this result. The lower panel of Figure 6.10 shows that the fifth force vanishes everywhere, except in the outskirts.

The middle and the lower panel of Figure 6.10 also display the theoretically expected screening radius and force ratio. It turns out that the analytical screening radius r_s (again, calculated from Eqn. 2.100) is still a very good proxy for the radius where the actual force ratio drops to unity, although it is unsurprisingly not as accurate as for the ideal NFW profiles (Figure 6.1). The force ratios are also captured pretty well by the theoretical predictions, but are only accurate to about 5% for realistic halos. As already mentioned, these differences occur due to the asymmetric shapes of the simulated halos and the presence of substructures. In the vicinity of a large subhalo the main halo may already be screened while the chameleon screening has not necessarily set in at the same radial distance on the opposite side of the halo. So my results show that the analytic model predictions are quite powerful for reasonably smooth halos whereas for objects with a high abundance of massive substructures, such as forming galaxy clusters or groups, their accuracy is somewhat compromised. This then also underlines that for scenarios with a very non-linear dependence of the fifth force on the density field, numerical simulations are essential to accurately capture all relevant effects.

Coming back to the requirement that the Solar system should be screened within the Milky Way, it is evident from Figure 6.10 that even the stronger F6 model fulfills this constraint. For the two more massive objects A and C, which are closer to the Milky Way in mass, the halo is already completely screened at the radius of the Solar system, i.e. $r \approx 8$ kpc. There is nevertheless not much space for more

strongly modified models. This finding is consistent with previous constraints of the $f(R)$ -model (see e.g. Terukina *et al.*, 2014).

6.4 Summary and Conclusions

In this chapter I analyzed the properties of Milky Way sized dark matter halos in Hu & Sawicki (2007) $f(R)$ -gravity employing cosmological zoom simulations. Using the simulation code MG-GADGET, I simulated a set of 7 DM halos from the Aquarius suite in the F6 and F7 models, as well as in the Λ CDM cosmology, for comparison. I also compared the simulation results against an analytical estimate of the fifth force in DM halos. My main findings can be summarized as follows.

- The theoretical predictions for the screening radius and the fifth force inside a spherical object derived in Vikram *et al.* (2014) (see also Section 2.3.8) reproduce the results obtained with my numerical modified gravity solver to high precision for ideal NFW-halos. For realistic halos from the cosmological simulations, the applicability is somewhat limited due to triaxial halo shapes and substructures. The theoretical estimate can nevertheless serve as a proxy for reasonably smooth and relaxed halos in relatively isolated environments.
- The self-similarity of DM halos observed in Λ CDM is broken in $f(R)$ -gravity due to the scale introduced by the screening radius for a given choice of f_{R0} . It can be approximately restored by appropriately scaling both f_{R0} and the mass of the object.
- My simulations show that the density of a Milky Way sized halo in F6 modified gravity is increased in the inner part, while it is slightly lower around r_{200} compared to GR. For the F7 model, the density profiles are largely unchanged.
- The impact of $f(R)$ -gravity on the mean halo concentration parameter cannot be reliably quantified from the simulations due to random scatter in fitting individual NFW density profiles and the small sample size. The density profiles, nevertheless, suggest a higher concentration of DM halos in $f(R)$ -gravity compared to Λ CDM. As higher concentrations imply a smaller Milky Way mass to match observational constraints, this appears to provide yet another potential solution for the too-big-to-fail problem (Boylan-Kolchin *et al.*, 2011; Cautun *et al.*, 2014).
- Circular velocities in $f(R)$ gravity are increased in unscreened regions with respect to the Λ CDM cosmology. Velocities calculated in the standard way only from the enclosed mass show a relative enhancement of about 12% in F6, while there is almost no difference for the F7 model due to the screening mechanism. For the circular velocities calculated more appropriately from the accelerations, there is an additional boost from the increased forces resulting in up to a 30% difference relative to GR for the F6 model, and in about 10%

higher velocities for the F7 model in the unscreened outer parts of the halos. One should pay attention that these two measures, which are equivalent in a Λ CDM cosmology, yield different results in $f(R)$ -gravity.

- The velocity dispersion inside the halos is increased by up to 40% in F6 with respect to standard gravity. This relative difference is larger than the enhancement of about 30% which is found in previous works. One can conclude that earlier works most likely did not have enough mass resolution to safely capture the effects on the density profile during structure formation and therefore missed an imported contribution to the enhanced velocity dispersion. For the F7 model, the differences to GR are much weaker due to the chameleon screening mechanism.
- The simulations show that the ratio of total-to-GR acceleration is increased by the theoretically expected factor of $4/3$ in the outer parts of the halos for F6 gravity. In the inner parts, the more massive halos of my sample are screened and thus show no difference in the force compared to GR. In the F7 model, the halos are almost completely screened and exhibit only a small force difference around r_{200} .
- The halos which have a mass close to that of the Milky Way are completely screened at the position of the Solar system both in the F6 and the F7 model. Halos with slightly lower mass do not show screening at the Solar circle, underlining that F6 is the strongest allowed $f(R)$ model. This is consistent with Solar system constraints on \bar{f}_{R0} from the literature.

All in all one can conclude that the effect of viable $f(R)$ -gravity models on the density profiles and velocity dispersions of Milky Way like halos are quite large. Both simulated parameter values of the Hu & Sawicki (2007) model, F7 and F6, are, according to my simulations, fully consistent with local constraints. Even models which are screened at the galactocentric radius of the Solar system can exhibit large differences in the velocity dispersion and the density profile. In the context of upcoming missions which are designed to test gravity on large scales, it is therefore essential to explore the alternatives to GR and the cosmological standard model, Λ CDM, in detail in order to provide reliable information on the effect of these theories on cosmological observables.

7 The Modified Gravity Lightcone Simulations

7.1 Introduction

In this chapter I will present first results from an ongoing project employing very large cosmological simulation in $f(R)$ -gravity and a Λ CDM model. The aim of the project is to explore the impact of $f(R)$ -gravity on structure formation at very large scales. The simulation setup is particularly designed to analyze weak gravitational lensing, halo and dark matter clustering as well as angular power spectra and correlation functions on backward lightcones which are part of the simulation output. With this analysis I hope to find hints how to best test $f(R)$ -gravity with upcoming large scale structure surveys like EUCLID or LSST.

The following sections are structured as follows. In Section 7.2 I will describe the simulation setup, the output and analysis methods used in detail. Section 7.3 presents preliminary results and in Section 7.4 I will summarize them and draw conclusions.

7.2 Simulations and methods

The complete simulation setup for this project consists of four collision-less cosmological simulations containing 2048^3 simulation particles in $768 \text{ Mpc}/h$ and $1536 \text{ Mpc}/h$ boxes. These simulations are, in terms of particle number the largest $f(R)$ -gravity simulations carried out so far. The $f(R)$ -gravity run for the larger box is currently not finished yet. I will therefore focus on an analysis of the two smaller box simulations in the following. Each of the boxes is simulated once for a Λ CDM cosmology and once for $f(R)$ -gravity. The set of cosmological parameters is $\Omega_m = 0.3089$, $\Omega_\Lambda = 0.6911$, $\Omega_B = 0.0486$ and $h_0 = 0.6774$, consistent with Planck Collaboration *et al.* (2016a) constraints. The simulations are carried out with MG-GADGET employing the local timestepping approach described in Section 3.2.3.

Besides a frequent standard snapshot output the simulations feature both a 2D and a 3D lightcone output. The 2D lightcones are written in terms of 401 HEALPIX maps (Górski *et al.*, 2005) which are equally spaced in look-back time between redshift $z = 49$ and $z = 0$. The 3D lightcones contain full particle positions in the range $z = 1.4 - 0$.

The lightcones are written in the following way. If the simulation reaches a redshift at which a lightcone output is desired, the lightcone routine is called. This routine repeats the simulation box periodically in all directions around a given center (an

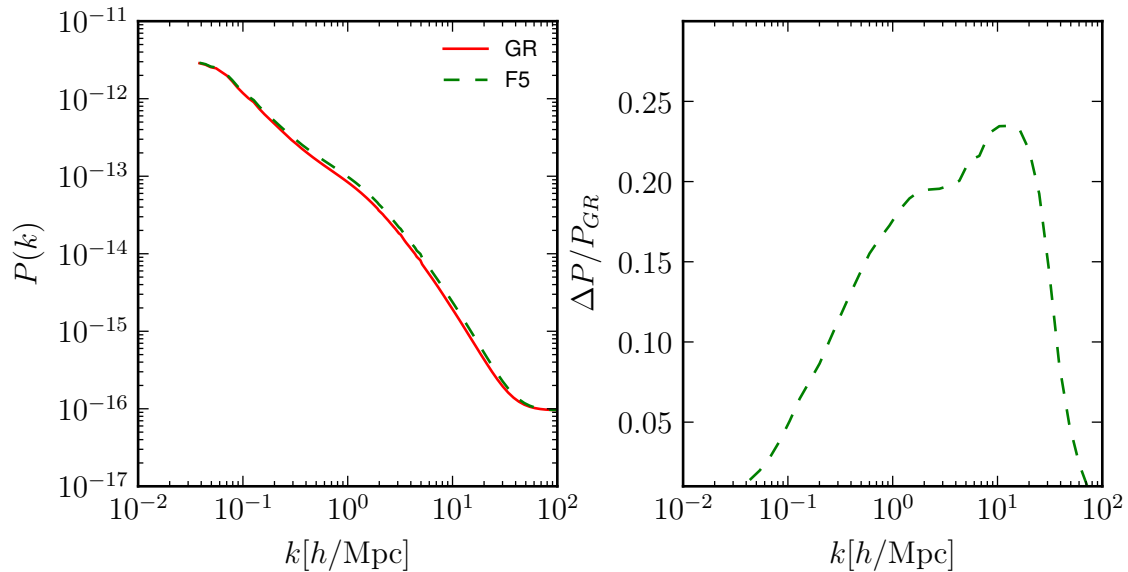


Figure 7.1: *Left panel:* The matter power spectrum of the 1536Mpc/ h boxes at $z = 0$ for $f(R)$ -gravity (*green*) and standard gravity (*red*). The relative difference between the $f(R)$ and the Λ CDM power spectrum is shown in the *right panel*.

imaginary observer). The algorithm then selects all particles which are contained in a spherical shell of finite thickness around the imaginary observer. The radius of the shell corresponds to the current redshift of the simulation. Its thickness represents the desired redshift interval. The positions and the properties of the particles in the shell are finally either written out in terms of a 3D lightcone output or binned onto a HEALPIX map.

For the computation of angular power spectra and two-point correlation functions, several of these HEALPIX maps are stacked. In order to identify halos and sub-halos the SUBFIND algorithm implemented in MG-GADGET was used. It determines the position bond over-dense regions in terms of the minimum of the gravitational potential of the structure.

7.3 Results

To verify that the simulation results match the findings of previous works, I will first present a few standard cosmological measures. The matter power spectrum for the 1536Mpc/ h simulation boxes are displayed in Figure 7.1. The power spectra are extended to the high- k range of the plot by folding the density field onto itself. As one can see from the plot, the power spectrum is increased in the $\bar{f}_{R0} = 10^{-5}$ model with respect to GR. The relative difference reaches 25% on scales of $k = 10h/\text{Mpc}$. This enhancement is consistent with the values quoted in the literature (Li *et al.*, 2013c; He *et al.*, 2015).

Figure 7.2 shows the halo mass functions for a $|\bar{f}_{R0}| = 10^{-5}$ and a Λ CDM model

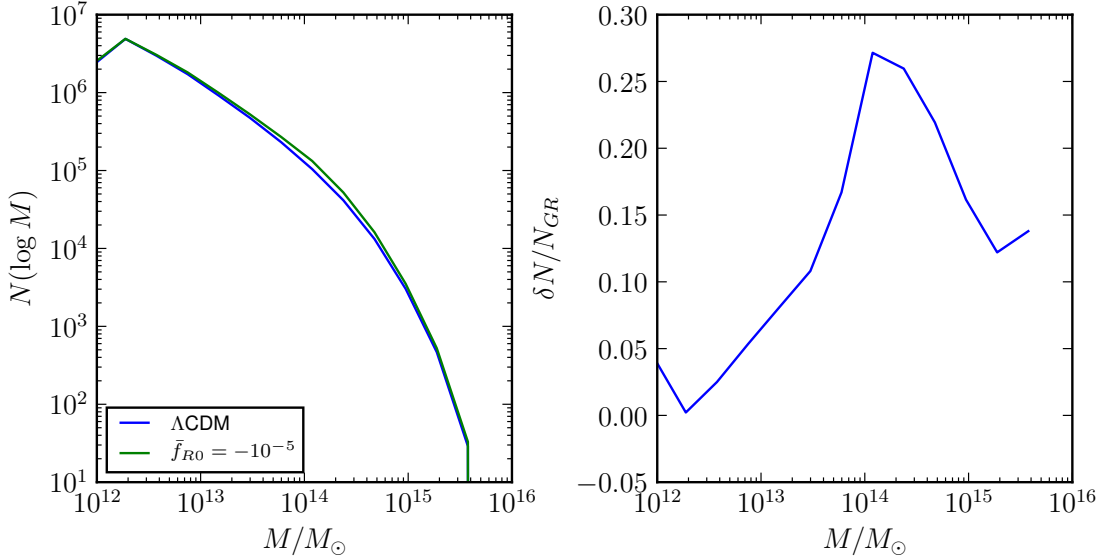


Figure 7.2: *Left panel:* The halo mass functions for the large simulation boxes at redshift zero for the $|\bar{f}_{R0}|= 10^{-5}$ model and a Λ CDM universe. The relative difference between the modified gravity and the GR results is shown in the *right panel*.

as well as the relative difference between the two. The number of halos with masses above $10^{13} M_\odot$ is enhanced in $f(R)$ -gravity due to the higher gravitational forces in unscreened regions. The higher forces cause that a given halo accumulates more mass in $f(R)$ -gravity compared to GR. It will consequently appear in a higher mass bin of the plot. At the high mass end of the plot, the halos are so massive that chameleon screening is already active during their formation. With growing mass, the forces in the outer region of the halos will thus become more and more similar to the GR forces resulting in a halo mass comparable to GR as well. The relative difference between the models is again consistent with values quoted in previous works (Lombriser *et al.*, 2013; Schmidt *et al.*, 2009).

The two point correlation function of the dark matter density fields for the modified gravity and the GR simulations are shown in Figure 7.3. Although they can in principle be obtained by calculation the Fourier transform of the matter power spectrum, the results are obtained through a tree based algorithm (Springel *et al.*, 2005) in real space. As one can see from the plot, the dark matter auto-correlation function is enhanced in $f(R)$ -gravity with respect to the standard model, while the relative difference is also redshift dependent. At $z = 1$, the differences solely appear at large scales, while the low-radius end of the plot is not significantly different from Λ CDM. At present times, the relative difference reaches 25% at small scales and grows up to 200% around $r = 20 \text{ Mpc}/h$. This behaviour can be easily explained by the evolution of the background field which sets the threshold for screening: As one can see from Figure (2.3), the value of $\bar{f}_R(a)$ drops with growing redshift. In other

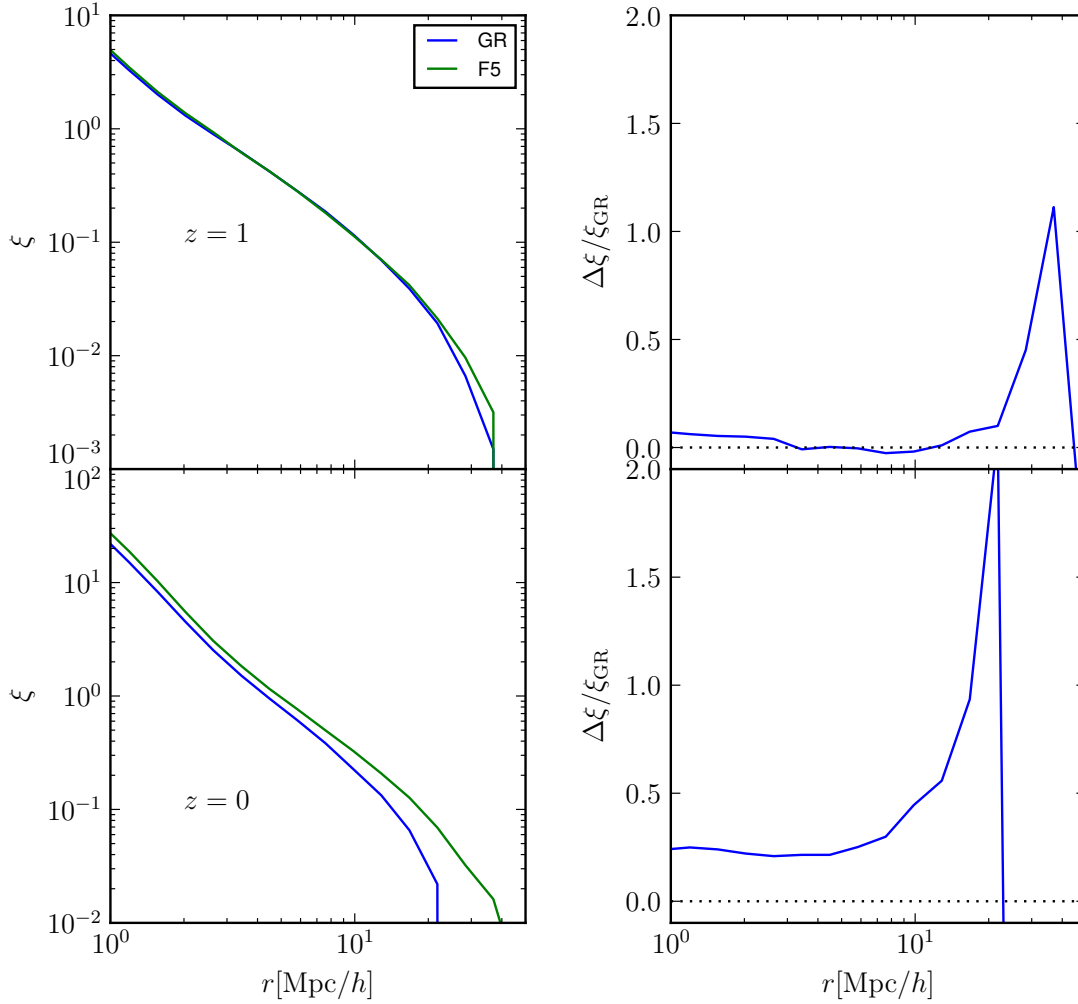


Figure 7.3: *Left panels:* The two-point correlation functions of the dark matter density field of the 1536 Mpc/h simulation boxes for a $|\bar{f}_{R0}| = 10^{-5}$ (F5, orange) universe and a Λ CDM model (blue) at $z = 1$ (top panel) and $z = 0$ (lower panel). The *right panels* show the corresponding relative differences between the correlation functions of the two cosmologies.

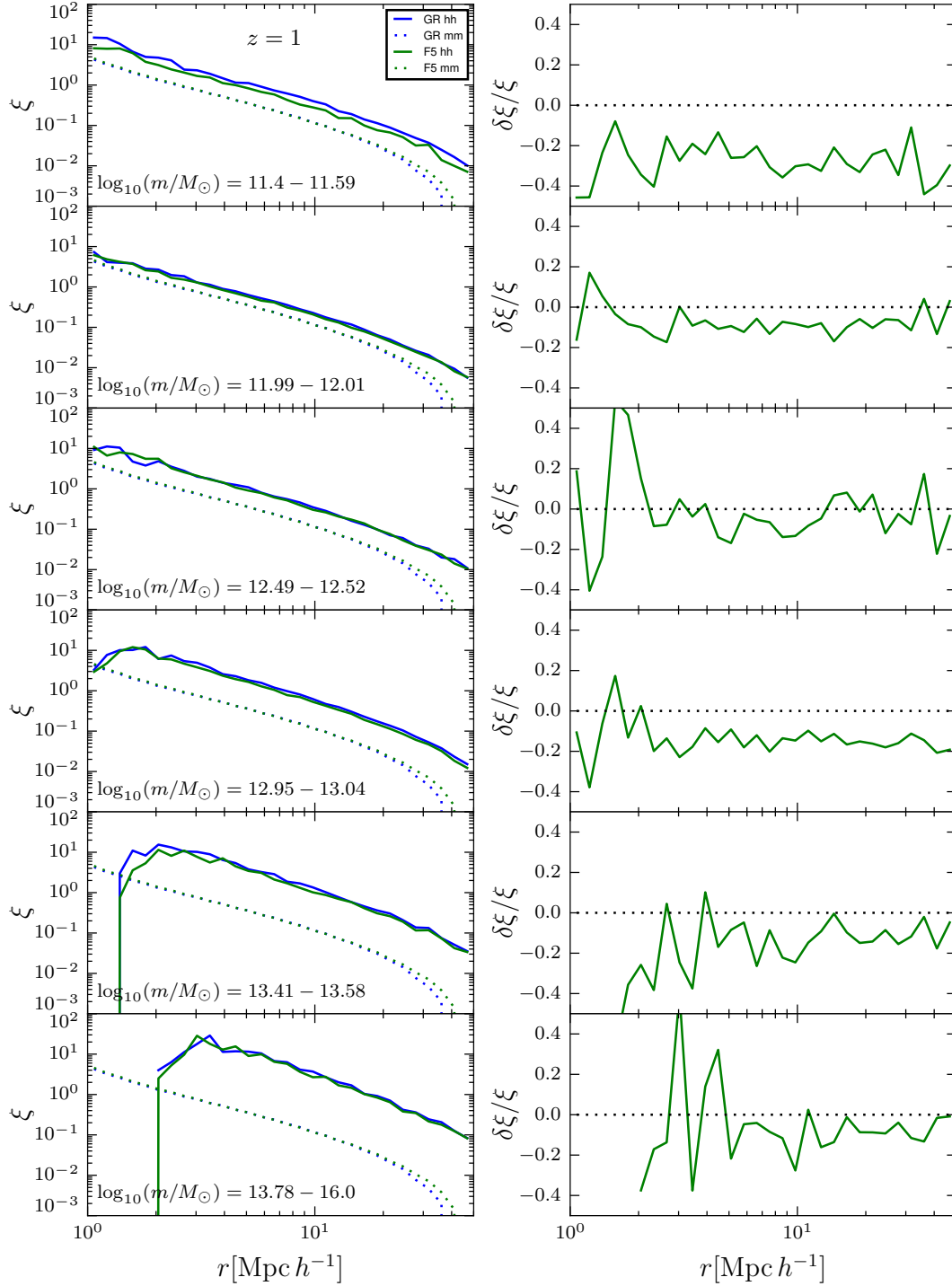


Figure 7.4: *Left panels:* The two-point correlation functions of the dark matter halos identified by the SUBFIND algorithm (halo-halo auto correlation function, hh) in the large simulation boxes (*solid lines*) for different mass-bins (in terms of $m_{200 \text{ crit}}$) at $z = 1$. GR results are displayed in *blue*, $f(R)$ results in *green*. The *dotted lines* (mm) are density field correlation functions already presented in Figure 7.3. The *right panels* show the corresponding relative differences between the halo two point correlation functions.

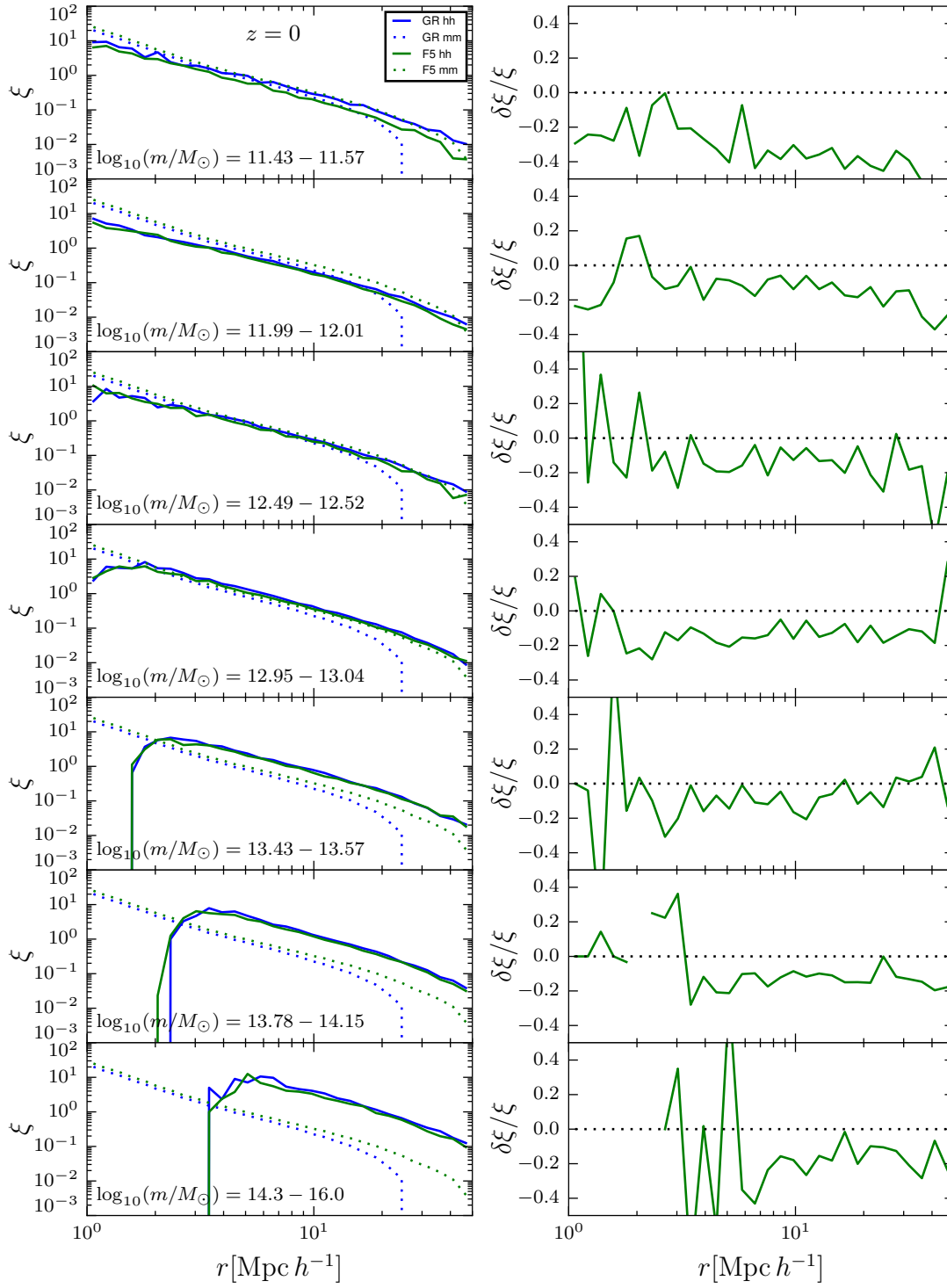


Figure 7.5: Same as Figure 7.4 but for $z = 0$.

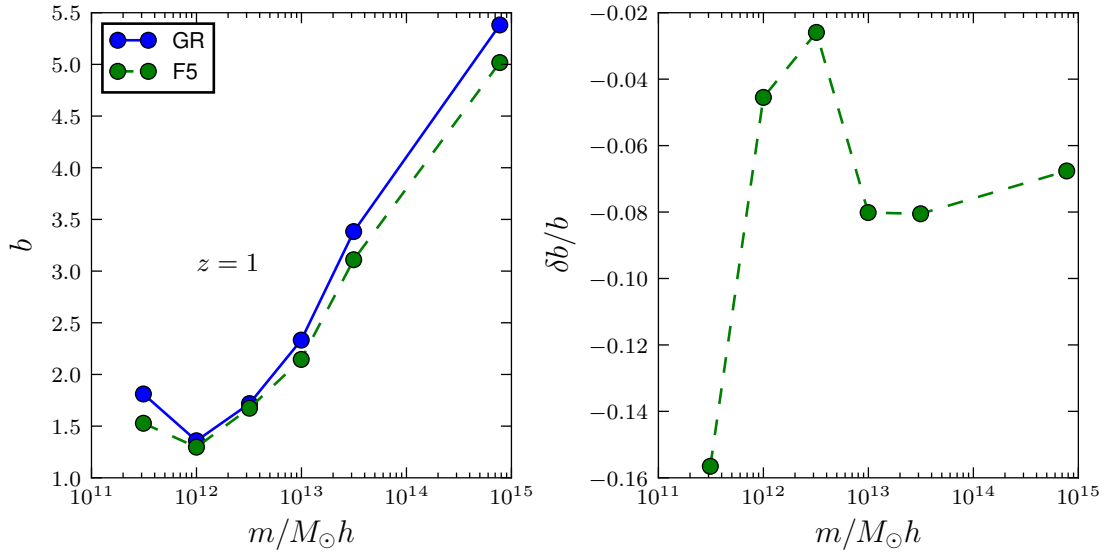


Figure 7.6: *Left panel:* The halo assembly bias for $|\bar{f}_{R0}| = 10^{-5}$ (green) and standard gravity (blue) as a function of mass at $z = 1$. The *right panel* displays the relative difference between the two models.

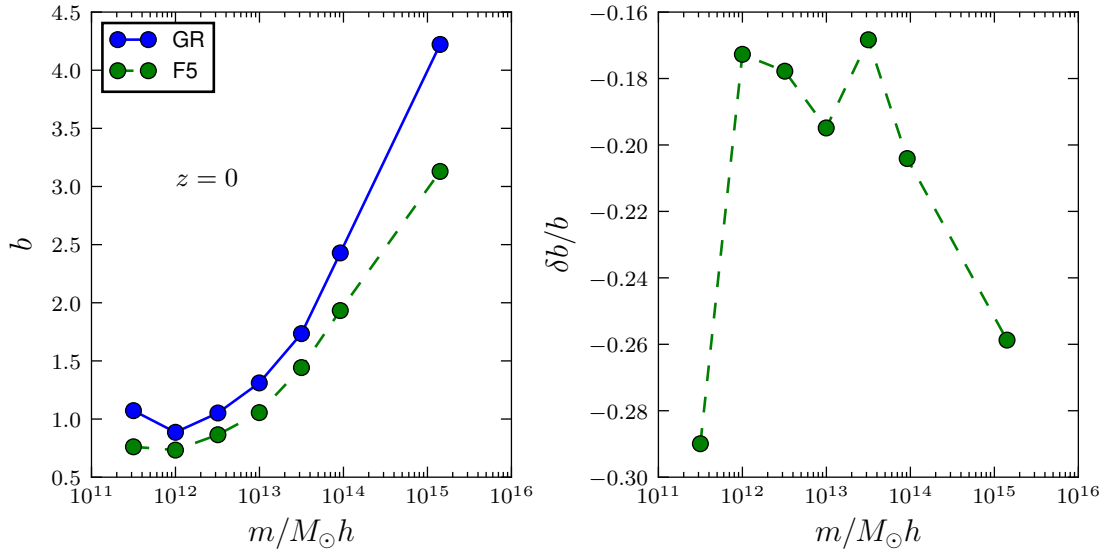


Figure 7.7: Same as Figure 7.6 but at $z = 0$.

words, the onset threshold for screening is lower at higher redshift causing lower mass objects to be screened as well. The impact of $f(R)$ -gravity at higher redshift is thus very limited and becomes larger with time. This behaviour was also observed for the results in Chapter 5 and can be explained by the redshift evolution of the scalar field (see Figure 2.3).

The statistical distribution of dark matter halos differs from that of the dark matter density field. The associated halo assembly bias, i.e. the ratio of the matter-matter and halo-halo auto-correlation functions $b = \xi_{hh}/\xi_{mm}$, is one of the highly debated measures in cosmology. To get an insight how this measure is affected by $f(R)$ -gravity, Figures 7.4 and 7.5 show the halo-halo correlation function for halos in different mass bins at $z = 1$ and $z = 0$, respectively. The Figures show that the halo two point correlation function is highly mass dependent for both modified and standard gravity. For both redshifts the differences between the halo and matter auto-correlation functions are rather small in the low mass bins and grow with increasing mass. Interestingly, the halo-halo correlation function takes on average lower values in $f(R)$ -gravity compared to Λ CDM for all mass bins at both redshifts. The differences between modified gravity and GR are larger for low mass halos which is reasonable as the fifth forces will more likely be screened in high mass objects.

In order to compute the halo assembly bias, the average value of b was calculated for each model, mass bin and redshift. The results are displayed in Figures 7.6 and 7.7. As already mentioned above, the halo bias is in general low at low halo masses and grows towards the high mass end of the plot. The bias in $f(R)$ -gravity is lower compared to GR over the whole mass range of both plots. At $z = 1$ it nevertheless remains larger than unity for all mass bins, showing an average relative difference of $\approx -6\%$ compared to a Λ CDM universe. This is not the case at present times. While the bias is approximately one for GR the values drop to $b = 0.75$ for $f(R)$ -gravity at the low mass end of the plot. This means that low-mass dark matter halos are less correlated than the dark matter density field in an $f(R)$ universe today. The relative difference in bias between $f(R)$ -gravity and GR is on average $\approx -18\%$ with outliers at the high and low mass end of the plot. One can thus conclude again that the impact of $f(R)$ -gravity grows with time.

To give an example of how the 2D lightcone output looks like Figure 7.8 displays a stacked HEALPIX map for a redshift range from $z = 1.1 - 0.9$ which was obtained by adding the individual maps corresponding to these redshifts. Each pixel encodes the simulation particle count corresponding to a part of the Sky. As all simulation particles have the same mass, these counts can easily be converted to a density map and be used to obtain the angle-based results presented below.

The first result obtained from the HEALPIX maps is the angular matter power spectrum shown in Figure 7.9. In order to reduce noise the maps were stacked over a certain redshift range for each of the plots. For all redshifts presented in the plot, the angular power is only very mildly affected by $f(R)$ -gravity at large scales ($l \approx 100$) while the relative differences between the models grow with increasing multipole number. At $z = 1.5$, the relative difference reaches $\approx 7\%$ at $l = 10^4$. For $z = 1$ the relative difference to GR is already 15% at these scales and reaches more

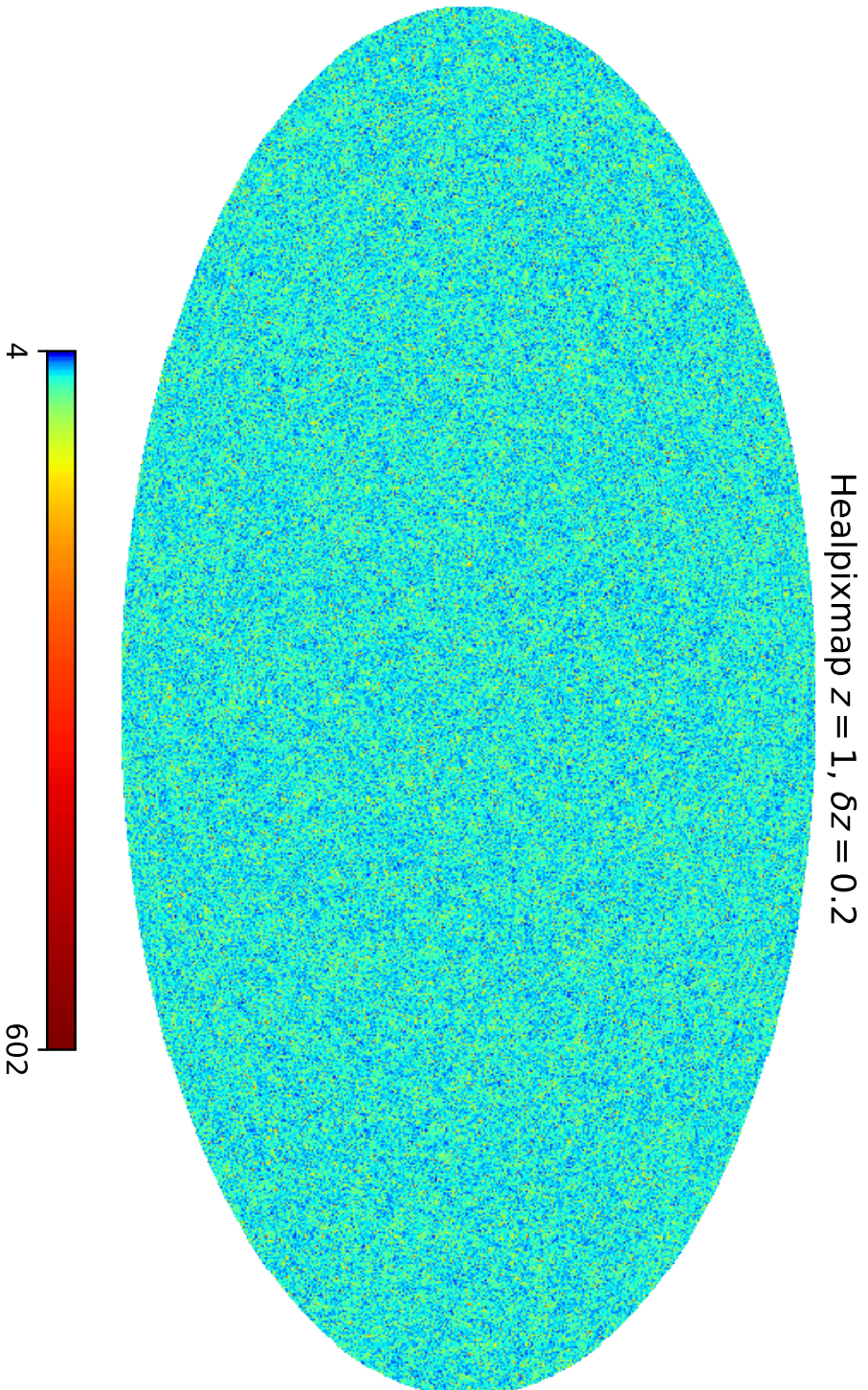


Figure 7.8: Stacked HEALPIX full sky map from the 2D lightcone output of the $|\bar{f}_{\text{hal}}| = 10^{-5}$ simulation. The map was obtained by adding the HEALPIX outputs corresponding to a redshift range from $z = 1.1 - 0.9$. The color encodes the particle count for each pixel (between 4 and 602 simulation particles). The map contains $8192^2 * 12$ pixels.

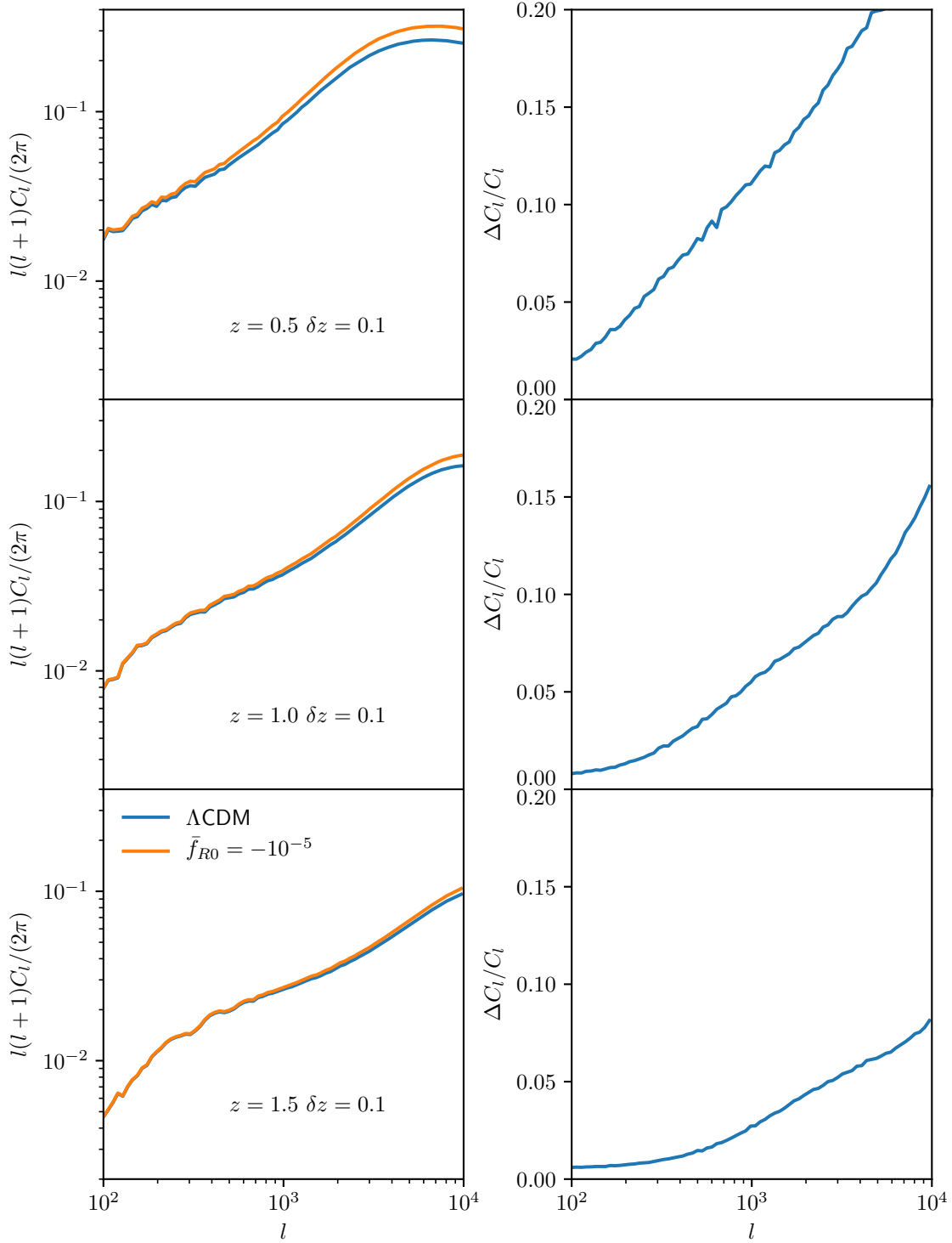


Figure 7.9: *Left panels:* Angular matter power spectra obtained from stacked HEALPIX maps at $z = 0.5, 1.0$ and 1.5 with a shell thickness of $\delta z = 0.1$ for $|\bar{f}_{R0}| = 10^{-5}$ (orange) and GR (blue). The *right panels* show the relative differences between the models at the corresponding redshifts.

than 20% at redshift 0.5. This result is thus consistent with the enhanced power in the matter power spectrum in $f(R)$ -gravity and also fits in the big picture of growing $f(R)$ influence with decreasing redshift.

7.4 Conclusion and discussion

In this Chapter I analyzed the results of simulations containing 2048^3 simulation particles in a $1536 \text{ Mpc}/h$ side-length simulation box which were carried out for both the $|\bar{f}_{R0}| = 10^{-5}$ model and standard gravity. The impact of $f(R)$ -gravity on the large scale structure in these simulations can be summarized as follows.

- Both the 3D matter power spectrum and the 2D angular power spectrum are enhanced in $f(R)$ -gravity with respect to a Λ CDM universe. The relative differences are bigger on smaller scales and increase with decreasing redshift. The maximum relative difference in the matter power spectrum is of order 25% at scales of $k = 10 h/\text{Mpc}$ at $z = 0$. The angular power spectrum is enhanced by more than 20% in modified gravity compared to GR at $z = 0.5$ and $l = 10^4$.
- The halo mass function is increased in $f(R)$ -gravity with respect to GR as well. The relative difference between the models depends on the halo mass as the screening mechanism introduces a mass scale. It reaches 25% at $m = 10^{14} M_\odot$. This and the previous result are consistent with the ones reported in the literature underlining the validity of the methods used for the simulations.
- The two point correlation function of the dark matter density field is increased in modified gravity compared to the standard model while the two point correlation function of the dark matter halos is on average lower in $f(R)$ -gravity. The effects are stronger at lower halo mass.
- The resulting halo assembly bias is significantly lower in $f(R)$ -gravity relative to GR. The difference is larger at lower redshift, reaching on average $\approx -18\%$ at $z = 0$. While the bias stays > 1 for the Λ CDM model at zero redshift it reaches values < 1 at halo masses around $10^{12} M_\odot/h$ for the considered modified gravity model. Halos of approximately Milky-Way mass will thus be less correlated than the dark matter density field in $f(R)$ -gravity at present times.

Wrapping up one can conclude that the simulations show once again that the effects due to the modified forces on statistical cosmological measures in $f(R)$ -gravity are higher at lower redshift. The screening mechanism introduces a scale, i.e. the onset threshold for screening, which results in larger $f(R)$ effects on lower mass objects. As a result, spatial scale dependent statistical measures are influenced by modified gravity to a higher degree on smaller scales. The fact that these scales are also heavily influenced by baryonic processes such as feedback from active galactic

nuclei or supernovas (see e.g. Vogelsberger *et al.*, 2014a; Puchwein *et al.*, 2013) will make the signatures of $f(R)$ -gravity very difficult to probe through power spectra or correlation functions. In order to probe gravity with upcoming large scale structure surveys such as EUCLID it is therefore crucial to also include the effects of baryons in future simulations unless one finds signatures of modified gravity which are less degenerate with baryonic physics.

8 The Sunyaev-Zeldovich effect in $f(R)$ -gravity

8.1 Introduction

In this Chapter I will present preliminary results on an ongoing project. The aim of the project is to determine the effects of $f(R)$ -gravity on the Sunyaev-Zeldovich (SZ) signal employing full-physics hydrodynamical simulations with AREPO.

The SZ effect (Sunyaev & Zeldovich, 1972) provides a powerful cosmological probe of hot intra-cluster gas (Planck Collaboration *et al.*, 2016b; Schäfer *et al.*, 2006). CMB photons which travel through these regions get an energy kick via inverse Compton scattering which changes their spectrum. The photons therefore carry information not only on the temperature of the intervening gas but also on its kinetic motion. Statistically analyzing both the kinetic and the thermal part of the SZ-signal can therefore provide constraints on cosmological models such as $f(R)$ -gravity (Arnold *et al.*, 2014).

This chapter is structured as follows. In Section 8.2, I will describe the simulation setup and the method used to obtain the SZ-maps. The results are presented in Section 8.3 while Section 8.4 concludes my findings.

8.2 Simulations and Methods

The simulations of this project are carried out with AREPO and the modified gravity solver presented in Section 3.3.1. The final simulation suite is planned to consist of a set of non-radiative hydrodynamical simulations for both $f(R)$ -gravity and a Λ CDM model as well as a set of full-physics simulations for both models. The full-physics simulations will cover a number of baryonic processes such as star formation, stellar feedback, cooling and feedback from active galactic nuclei using a model similar to the one used in Weinberger *et al.* (2017).

The results presented in the following instead focus on the non-radiative simulations. They are carried out using 512^3 simulation particles and roughly the same number of mesh-generating points (i.e. Voronoi mesh cells for the hydrodynamical solver) in a $62 \text{ Mpc}/h$ side-length simulation box. The set of cosmological parameters is $\Omega_m = 0.3089$, $\Omega_\Lambda = 0.6911$, $\Omega_B = 0.0486$ and $h_0 = 0.6774$.

The SZ-signal can be observed in different ways. One possibility is to focus on individual galaxy clusters and to integrate over the volume of the object ending up

with the (angular) integrated Compton- y parameter

$$Y_{SZ} = \int y d\Omega, \quad (8.1)$$

where the Compton parameter for the thermal SZ-effect is given by

$$y = \frac{k_B \sigma_T}{m_e c^2} \int T_e n_e dl. \quad (8.2)$$

The Thompson scattering cross-section is denoted as σ_T , the electron mass, temperature and number density are given by m_e , T_e and n_e , respectively. This method was applied in previous works on $f(R)$ -gravity simulations (Arnold *et al.*, 2014; Peirone *et al.*, 2016) and is also applicable to observations (Rozo *et al.*, 2014; Planck Collaboration *et al.*, 2011, 2013a,b). In this work I will nevertheless take a different approach.

Following the methods used in Springel *et al.* (2001) and Dolag *et al.* (2005) one can obtain the thermal SZ-signal from equation (8.2) directly by carrying out the integral along the path of the photons. The routine which creates SZ-maps from the simulation outputs works as follows. First, an arbitrary $1^\circ \times 1^\circ$ section of the sky seen by an imaginary observer in the simulation box is selected (see also Figure 8.1). The simulation box is then repeated along this direction to fully cover the small lightcone which is spanned by the section of the sky. At each position along the cone, the simulation output which is closest in time to the redshift corresponding to the position is chosen. In total, there are 46 output times for snapshots in the simulations. In order to avoid statistical correlations due to the repetition of the boxes, the simulation boxes are shifted by an arbitrary distance and rotated by an arbitrary angle for each snapshot. The redshifts for the simulation outputs are chosen such that each position in a snapshot is only used once in the z (redshift) direction for a slice z_i in Figure 8.1. It might nevertheless appear multiple times in directions orthogonal to the cone.

Once the cone of the patch on the sky is constructed, it is divided into 512×512 rectangular pixels. For each of the pixels, a ray is shot along the lightcone. To carry out the integral in (8.2), all gas cells which are intersected by the ray are considered. In order to avoid extensive geometrical computations the gas cells are assumed to be spherical, i.e. they are considered if the distance between their center of mass and the ray is

$$r_{\text{cell-ray}} < 2.5 \left(\frac{3V_{\text{cell}}}{4\pi} \right)^{\frac{1}{3}}. \quad (8.3)$$

The factor of 2.5 is used to smooth the gas distribution (similar to an SPH smoothing radius). Using the same approach as Springel *et al.* (2001), the Compton- y parameter for a pixel ij is calculated by adding the contributions of all considered cells α

$$y_{ij} = \frac{1}{h^2} \frac{\sigma_T}{m_e c^2} \sum_{\alpha} p_{\alpha} w_{\alpha,ij}, \quad (8.4)$$

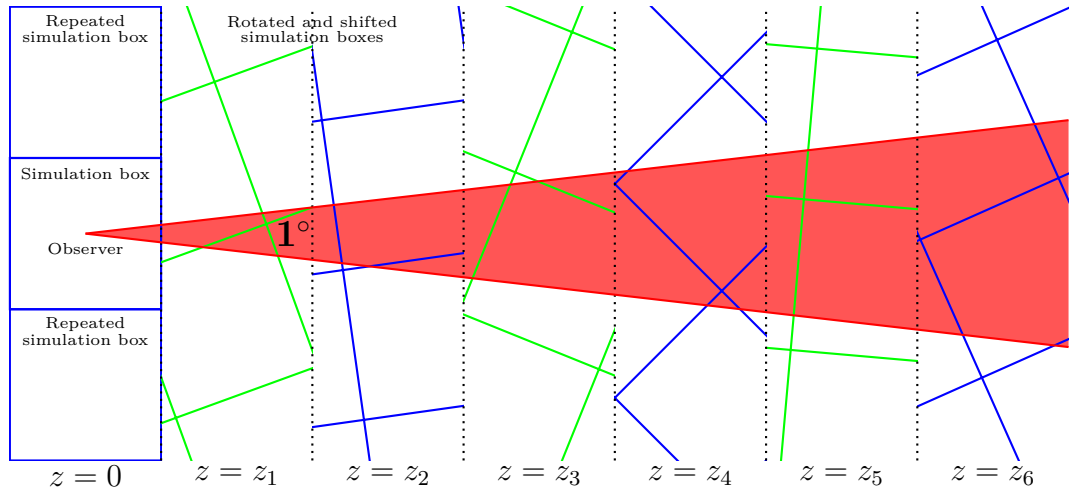


Figure 8.1: Illustration of the method used to obtain a $(1^\circ)^2$ SZ-map from the simulation outputs. The patch of the sky considered for the map is indicated in red.

where

$$p = (\gamma - 1)(1 - Y_p)mu\mu x_e. \quad (8.5)$$

h denotes the side-length of a pixel, $w_{\alpha,ij}$ is a normalized smoothing kernel, γ the ratio of specific heats, Y_p the primordial He_4 mass fraction, m the mass of the particles, u the internal energy per mass, μ the mean molecular weight and x_e the ratio of electron number density to hydrogen number density.

In a similar way, one can calculate the kinetic part of the SZ-effect through

$$b = \sigma_T \int dl \frac{n_e v_r}{c}, \quad (8.6)$$

where b is a measure of the temperature fluctuation $b = -\frac{\Delta T}{T}$ and v_r is the radial velocity of the gas.

8.3 Results

To give an impression of the SZ-maps generated by the algorithm described above, Figure 8.2 shows thermal and kinetic SZ-maps for the non-radiative run in the standard Λ CDM cosmology. Bright yellow spots in the thermal map represent a regions with strong SZ-signal, i.e. galaxy clusters with plenty of ionized gas. For the kinetic signal the b parameter can be both positive and negative, depending on if the gas is moving away from the observer (bright yellow structures in the plot) or towards him (dark blue structures), respectively.

Figure 8.3 displays the angular power spectrum obtained from both the thermal and the kinetic SZ-maps for $|\bar{f}_{R0}| = 10^{-6}$ and a standard cosmology. The results

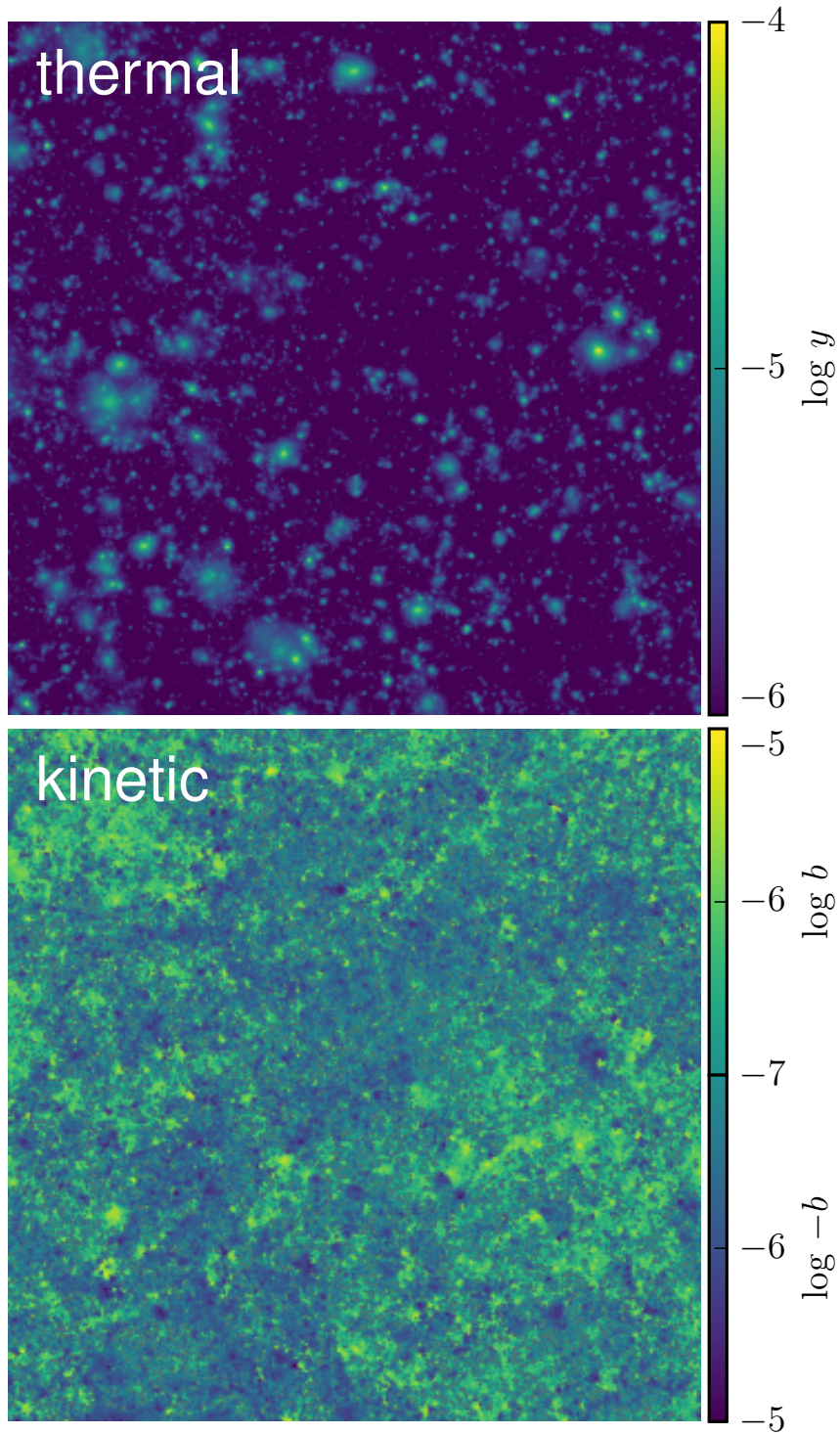


Figure 8.2: Maps for the thermal (*top panel*) and kinetic (*bottom panel*) SZ-effect obtained from the non-radiative GR simulation. The maps have a side-length of 1° and a resolution of 512^2 pixels. The thermal signal is shown in terms of the Compton- y parameter, the kinetic signal in terms of the b parameter which can be both positive and negative.

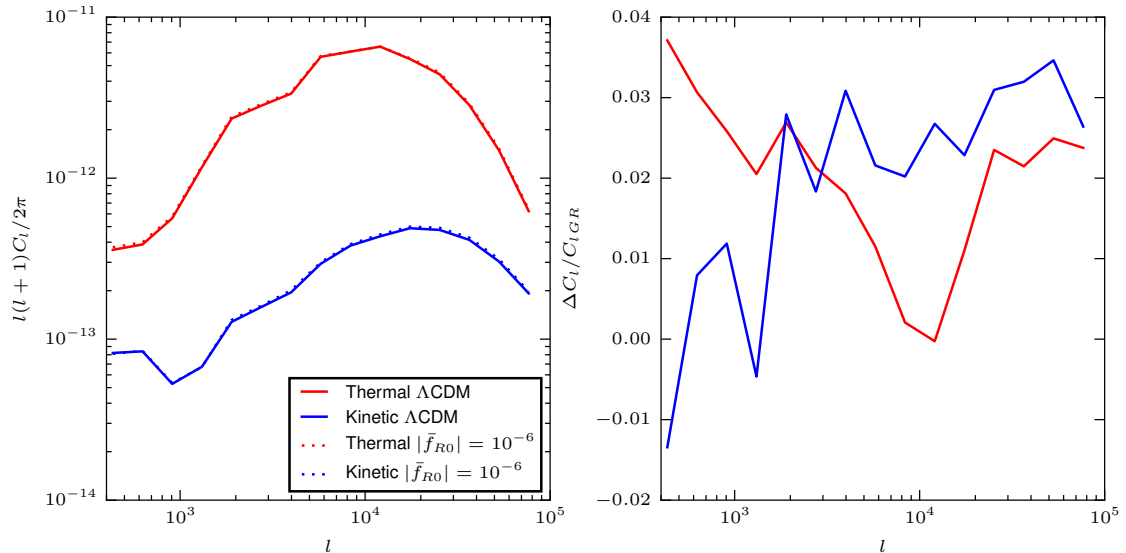


Figure 8.3: *Left panel:* The angular power-spectrum obtained from the synthetic SZ-maps for a Λ CDM universe (*solid lines*) and $f(R)$ -gravity (*dotted lines*). The spectrum for the thermal SZ-effect is shown in *red*, the one for the kinetic SZ-effect in *blue*. The relative difference between modified gravity and GR is shown in the *right panel*.

on the angular power spectra are consistent with the ones presented in Dolag *et al.* (2005). The relative difference between $f(R)$ -gravity and Λ CDM turns out to be very small for both the thermal and the kinetic SZ-effect. The thermal spectrum shows 1 – 3% higher values in modified gravity compared to GR. For the kinetic SZ-effect, the power spectrum is enhanced by on average 3% on scales smaller than $l = 2000$. As $f(R)$ -gravity makes a given galaxy cluster slightly more massive compared to standard gravity (see e.g. Arnold *et al.*, 2014) and matter more correlated on small scales, it is not surprising that the angular power spectrum is enhanced. The relatively small size of the effect is likely caused by two reasons. First, $|\bar{f}_{R0}| = 10^{-6}$ is a quite weak model which has only very moderate effects on the matter power spectrum (see e.g. Puchwein *et al.*, 2013). It is thus reasonable that the effects on the SZ-spectrum are small as well. Second, the SZ-effect primarily probes gas in massive galaxy clusters. These objects are mostly screened by the chameleon mechanism and will therefore not be heavily influenced by $f(R)$ -gravity. In order to make a more robust statement on the SZ-effect it would therefore be good to also simulate a model with stronger modifications such as $|\bar{f}_{R0}| = 10^{-5}$.

8.4 Conclusion and Discussion

In this Chapter I analyzed the thermal and the kinetic SZ-effect in a Λ CDM model and $f(R)$ -gravity employing non-radiative hydrodynamical simulations with AREPO. I constructed synthetic SZ-maps by tracing the gas along backward lightcones through

the simulation box. These maps were then analyzed by calculating angular power spectra for both the kinetic and the thermal SZ-signal.

While the angular power spectra are consistent with previous works, the difference between the $|\bar{f}_{R0}| = 10^{-6}$ model and standard cosmology turned out to be very small. Both spectra are enhanced by a few percent in $f(R)$ -gravity with respect to GR. A larger effect is expected for stronger modifications of gravity.

In order to extend the analysis presented in this Chapter also full-physics hydrodynamical simulations in both Λ CDM and $f(R)$ cosmology will be carried out, which are now possible thanks to my modifications to AREPO. The feedback processes can have a significant impact on the gas in the simulations which is traced by the SZ-effect (Vogelsberger *et al.*, 2014a).

9 Discussion and Outlook

The theoretical explanation of the accelerated expansion of the Universe is one of the big open questions in cosmology. While the standard model of cosmology which explains the acceleration via the cosmological constant is very successful and consistent with most of the observations, it also features some problems. Therefore a large variety of alternatives to the Λ CDM model have been proposed in the past years. One group of them, the so called modified gravity models, modify the laws of gravity to account for the accelerated expansion.

In this thesis I considered $f(R)$ -gravity as one theory of this kind. It features the chameleon screening mechanism to shield the modifications to GR in high density environments which is necessary to meet solar system constraints on the strength of the gravitational interaction. In regions where the chameleon mechanism is inactive, the gravitational forces are increased by a factor of 4/3 in $f(R)$ -gravity. If the functional form of $f(R)$ is properly chosen, the theory can account for the accelerated expansion. In this work I adopted the Hu & Sawicki (2007) model which is in addition consistent with the observed expansion history of the universe.

In the coming years a number of large scale structure surveys are planned which are also designed to test for possible modifications to gravity. In order to do so, they require detailed information on how structure formation is influenced by the modifications to gravity.

With this work, I tried to address exactly this question for the $f(R)$ model. Employing cosmological N-body simulations I analyzed how different astrophysical observables change in $f(R)$ -gravity compared to the standard model. The aim of this work was furthermore to put constraints on the considered model and to find signatures which are most promising in terms of deciding which model best describes our Universe.

As the equations of motion are very non-linear in $f(R)$ -gravity, cosmic structure formation can not easily be solved with analytic approaches in this theory. I therefore carried out cosmological N-body simulations in order to explore how cosmological and astrophysical observables change in $f(R)$ -gravity. The simulation codes I used and developed for this purpose are MG-GADGET and AREPO. To make these codes more efficient and versatile, I implemented a local timestepping scheme and a non-periodic PM-solver for zoomed simulations in MG-GADGET. The local timestepping can lead to a significant speedup of the code, especially for hydrodynamical and zoomed cosmological simulations. I also wrote a modified gravity solver for AREPO to be able to carry out highly accurate and efficient hydrodynamical simulations with the code's moving mesh hydrodynamics solver in $f(R)$ -gravity. The results can be summarized as follows.

As a part of this thesis I contributed to a modified gravity code comparison project which compared different modified gravity simulation codes in order to verify their methods. It was found that cosmological measures such as power spectra or halo profiles agree on a few percent level in simulations carried out with different $f(R)$ codes. Small differences in the field and force profiles are induced by different relaxation criteria and force computation methods, respectively. These differences appear nevertheless primarily in screened regions and therefore do not have a significant influence on the total force and astrophysical observables.

I also carried out a set of hydrodynamical simulations dedicated to analyze the Lyman- α forest in $f(R)$ -gravity. I found that the influence of this modified gravity model on the Lyman- α forest is very small. Lyman- α flux PDFs and power spectra change by less than 5% in $|\bar{f}_{R0}| = 10^{-5}$ compared to a Λ CDM model. The reason is that this observable is commonly measured at redshifts $z = 2 - 3$. As the background value of the scalar field rapidly drops with growing redshift, the impact of $f(R)$ -gravity is very small at early times. Absorption line shapes are therefore only very mildly affected as well. Given the – compared to the $f(R)$ -effects – quite large statistical and systematic uncertainties in the observed Lyman- α power spectra and flux PDFs, it will be very hard to put constraints on $f(R)$ -gravity using these observables.

In order to find out how $f(R)$ -gravity affects the properties of Milky Way-sized dark matter halos, I performed a set of zoomed simulations with initial conditions from the Aquarius project. Depending on the background parameter, the density profiles, rotation curves and velocity dispersion of the halos change by up to 40% in $f(R)$ -gravity compared to GR. The $f(R)$ -to-standard gravity force ratio is 4/3 in unscreened regions as expected from theory. In screened regions, there is no fifth force. The size of the screened regions inside the halos depends on both the background parameter and on the mass of the object. Small substructures in unscreened regions can be screened if they are close enough to the main halo. With the zoomed simulations, I could confirm that the $|\bar{f}_{R0}| = 10^{-6}$ model is the strongest allowed $f(R)$ model if one requires the solar system to be screened within the Milky Way.

I also compared the force profiles of the simulated halos to theoretical predictions for the screening radius and the fifth force inside spherically symmetric objects. From this comparison one can conclude that the theoretical estimates work very accurately for ideal, isolated NFW-halos while the discrepancy between simulated and theoretical forces can be large for the real simulated halos. This can be explained by the not exactly spherical shape of the objects, substructures and the influences of nearby objects. The theoretical estimates can nevertheless serve as a rough measure of the screening radius.

For the modified gravity lightcone simulation project which is also a part of this thesis, I carried out the, in terms of particle number, largest $f(R)$ -gravity simulations to date. With the 2D and 3D lightcone output which I developed in MG-GADGET for this project, one can analyse clustering and lensing on the lightcone. These observables are particularly important in the context of upcoming large scale structure surveys. The results obtained so far show that dark matter power spectra and

two-point correlation functions are increased in $f(R)$ -gravity with respect to Λ CDM while dark matter halos are slightly less correlated in this modified gravity model. The halos consequently show a lower assembly bias in $f(R)$ -gravity compared to the standard model which can even be smaller than unity for Milky Way-sized halos at redshift zero. The angular power spectrum calculated from the 2D lightcone output is enhanced in $f(R)$ -gravity as well. The size of the effect decreases with redshift.

Another set of simulations I performed during this thesis with the AREPO code is dedicated to test the kinetic and thermal SZ-effect in $f(R)$ -gravity. First results show that the angular SZ-power spectra for both the thermal and the kinetic SZ-effect are mildly increased in $|\bar{f}_{R0}| = 10^{-6}$ with respect to GR. In order to make a more robust statement about the influence of $f(R)$ -gravity on the SZ-effect it would be helpful to simulate a model with stronger modifications of gravity.

All in all one can conclude that the effects $f(R)$ -gravity has on astrophysical observables and objects increases towards lower redshift due to the redshift evolution of the background field. Due to the Chameleon screening mechanism the influence in high density regions and on high mass objects is smaller. In order to constrain $f(R)$ -gravity, it will therefore be most promising to focus on low density objects at low redshift. Due to its relatively low mass and the quality of the available observational data, observables from the Milky Way are very promising to further constrain $f(R)$ -gravity. Data on the kinematics of objects in the outer regions of our Galaxy, which will be available soon from the Gaia satellite, has a great potential in this context. As recently proposed (Carlesi *et al.*, 2017), the dynamics within the local group might give powerful constraints as well.

In order to make good use of data in the comparison to simulations, one has to push modified gravity simulations forward into two directions. On the one hand, small mass objects are usually heavily influenced by baryonic physics. As baryonic feedback processes such as supernova or AGN feedback and modified gravity effects might well interact in a non-trivial way one has to include both effects in future simulations at the same time. Baryonic effects depend largely on gas densities, which are in turn influenced by the larger gravitational forces in modified gravity. A good understanding of the interplay between gas physics and the modifications to gravity is therefore essential to put more stringent constraints on modified gravity models. This would also help to resolve the degeneracy between e.g. $f(R)$ -gravity and AGN feedback in the matter power spectrum (Puchwein *et al.*, 2014) which is important for upcoming large scale structure surveys such as EUCLID or LSST.

Current modified gravity simulation codes, especially AREPO, are on the other hand restricted to a very limited number of modified gravity models. In order to explore a larger fraction of the model space it is therefore important to include additional gravity theories in the code and to possibly find effective descriptions which can cover a number of models at once.

The hunt for constraints on $f(R)$ -gravity does of course raise the question at which point one should consider the model to be ruled out. As $f(R)$ -gravity contains GR as a limiting case for $\bar{f}_{R0} \rightarrow 0$ it is especially difficult to define a clear threshold. If the background parameter becomes very small, $f(R)$ -gravity and Λ CDM are practically

indistinguishable. At this point, one would prefer the Λ CDM model as the easier description of the same physics. For a scalar field parameter of $|\bar{f}_{R0}|=10^{-7}$, the differences are already very small but one could still see effects in the very outer regions of the Milky Way (see Chapter 6). For a $|\bar{f}_{R0}|=10^{-8}$ model, this would be hardly possible. Employing equation (2.103) one can easily estimate that a $3 \times 10^{10} M_{\odot}$ halo would be largely screened in this model. If one manages to constrain $f(R)$ -gravity to a value of $|\bar{f}_{R0}| < 10^{-8}$ the theory would from my point of view be ruled out. Considering the currently most stringent constraint of $|\bar{f}_{R0}|=10^{-6}$, there is nevertheless still some room for the theory.

In conclusion one can say that $f(R)$ -gravity is still a valid theory which can explain the acceleration of the universe without a cosmological constant. In this thesis I was able to verify the solar system constraints on \bar{f}_{R0} through cosmological N-body simulations. I was also able to show that the Lyman- α forest is only weakly affected in $f(R)$ -gravity and that Milky Way-sized halos change structure in this theory, making the Local Group a promising environment for future tests of $f(R)$ -gravity. In order to get a better understanding of how cosmic structure formation is altered by theories of modified gravity in general, the simulation codes have to be extended to a broader range of models and baryonic effects have to be included in the simulations. Proceeding in this direction, future works in the field of modified gravity simulations will possibly be able to answer the question whether gravity on large scales is best described by GR or an alternative theory.

Acknowledgements

I am very grateful to everyone who supported me during this thesis. First and foremost I like to thank my supervisor Volker Springel very much for giving me the opportunity to carry out this thesis in his group and for his encouraging but relaxed way of supervision. He always took his time to discuss my problems and ideas which gave me the opportunity to benefit a lot from his outstanding expertise in the field numerical simulations.

I would furthermore like to express my gratitude to Ewald Puchwein who helped me many times with technical questions concerning the modified gravity solver and always had very helpful and interesting ideas for my work.

I am also grateful to the members of the theoretical astrophysics group at HITS for the inspiring atmosphere and the company during an almost infinite number of coffee breaks. It was a great time working with you guys! Especially, I like to thank Andreas Bauer and Kevin Schaal for sharing their programming experiences and for assisting me with many technical problems. I am furthermore very grateful to my officemate Rüdiger Pakmor who had an – usually helpful – answer to any question and was never at loss for encouraging comments on the topic of my thesis.

I also like to thank all my friends in Heidelberg who supported this thesis by distracting me from work and constantly reminding me that there are other important things to do. In particular, I am very grateful to my climbing partners for the countless evenings and weekends at the rocks and in the gym.

Abschließend möchte ich noch meiner Familie für die Unterstützung und den Rückhalt während dieser Arbeit und meiner gesamten Zeit in Heidelberg danken.

10 List of publications

Arnold, C., Puchwein, E., & Springel, V. 2014. *MNRAS*, **440**(May), 833–842.

This publication is not a part of this thesis.

Arnold, C., Puchwein, E., & Springel, V. 2015. *MNRAS*, **448**(Apr.), 2275–2283.

This publication is a part of this thesis. The results are presented in Chapter 5.

Arnold, C., Springel, V., & Puchwein, E. 2016. *MNRAS*, **462**(Oct.), 1530–1541.

This publication is a part of this thesis. The results are presented in Chapter 6 and Section 2.3.8.

Winther, H. A., Schmidt, F., Barreira, A., Arnold, C., Bose, S., Llinares, C., Baldi, M., Falck, B., Hellwing, W. A., Koyama, K., Li, B., Mota, D. F., Puchwein, E., Smith, R. E., & Zhao, G.-B. 2015. *MNRAS*, **454**(Dec.), 4208–4234.

Parts of this publication are also part of this thesis, presented in Chapter 4.

11 Bibliography

- Adamek, J., Daverio, D., Durrer, R., & Kunz, M. 2016. *JCAP*, **7**(July), 053.
- Amendola, L. 2000. *Phys. Rev. D*, **62**(4), 043511.
- Amendola, L., Appleby, S., Bacon, D., Baker, T., Baldi, M., Bartolo, N., Blanchard, A., Bonvin, C., Borgani, S., Branchini, E., Burrage, C., Camera, S., Carbone, C., Casarini, L., Cropper, M., de Rham, C., Di Porto, C., Ealet, A., Ferreira, P. G., Finelli, F., García-Bellido, J., Giannantonio, T., Guzzo, L., Heavens, A., Heisenberg, L., Heymans, C., Hoekstra, H., Hollenstein, L., Holmes, R., Horst, O., Jahnke, K., Kitching, T. D., Koivisto, T., Kunz, M., La Vacca, G., March, M., Majerotto, E., Markovic, K., Marsh, D., Marulli, F., Massey, R., Mellier, Y., Mota, D. F., Nunes, N. J., Percival, W., Pettorino, V., Porciani, C., Quercellini, C., Read, J., Rinaldi, M., Sapone, D., Scaramella, R., Skordis, C., Simpson, F., Taylor, A., Thomas, S., Trotta, R., Verde, L., Vernizzi, F., Vollmer, A., Wang, Y., Weller, J., & Zlosnik, T. 2013. *Living reviews in relativity*, **16**(Dec.), 6.
- Arnold, C., Puchwein, E., & Springel, V. 2014. *MNRAS*, **440**(May), 833–842.
- Arnold, C., Puchwein, E., & Springel, V. 2015. *MNRAS*, **448**(Apr.), 2275–2283.
- Arnold, C., Springel, V., & Puchwein, E. 2016. *MNRAS*, **462**(Oct.), 1530–1541.
- Avila-Reese, V, Zavala, J, Firmani, C, & Hernández-Toledo, HM. 2008. *The astronomical journal*, **136**(3), 1340.
- Barreira, A., Li, B., Hellwing, W. A., Baugh, C. M., & Pascoli, S. 2013. *JCAP*, **10**(Oct.), 027.
- Becker, G. D., Bolton, J. S., Haehnelt, M. G., & Sargent, W. L. W. 2011. *MNRAS*, **410**(Jan.), 1096–1112.
- Becker, G. D., Hewett, P. C., Worseck, G., & Prochaska, J. X. 2013. *MNRAS*, **430**(Apr.), 2067–2081.
- Bolton, J. S., Viel, M., Kim, T.-S., Haehnelt, M. G., & Carswell, R. F. 2008. *MNRAS*, **386**(May), 1131–1144.
- Boylan-Kolchin, M., Bullock, J. S., & Kaplinghat, M. 2011. *MNRAS*, **415**(July), L40–L44.

- Brax, P., van de Bruck, C., Davis, A. C., Khoury, J., & Weltman, A. 2004 (Nov.). Chameleon Dark Energy. *Pages 105–110 of:* Martins, C. J. A. P., Avelino, P. P., Costa, M. S., Mack, K., Mota, M. F., & Parry, M. (eds), *Phi in the sky: The quest for cosmological scalar fields*. American Institute of Physics Conference Series, vol. 736.
- Brax, P., van de Bruck, C., Davis, A.-C., & Shaw, D. J. 2008. *Phys. Rev. D*, **78**(10), 104021.
- Broderick, A. E., Chang, P., & Pfrommer, C. 2012. *ApJ*, **752**(June), 22.
- Buchdahl, H. A. 1970. *MNRAS*, **150**, 1.
- Cai, Y.-C., Li, B., Cole, S., Frenk, C. S., & Neyrinck, M. 2014. *MNRAS*, **439**(Apr.), 2978–2989.
- Caldwell, R. R. 2002. *Physics letters b*, **545**(Oct.), 23–29.
- Calura, F., Tescari, E., D’Odorico, V., Viel, M., Cristiani, S., Kim, T.-S., & Bolton, J. S. 2012. *MNRAS*, **422**(June), 3019–3036.
- Carlesi, E., Mota, D. F., & Winther, H. A. 2017. *MNRAS*, Jan.
- Cautun, M., Frenk, C. S., van de Weygaert, R., Hellwing, W. A., & Jones, B. J. T. 2014. *MNRAS*, **445**(Dec.), 2049–2060.
- Clifton, T., Ferreira, P. G., Padilla, A., & Skordis, C. 2012. *Phys. Rep.*, **513**(Mar.), 1–189.
- Compostella, M., Cantalupo, S., & Porciani, C. 2013. *MNRAS*, **435**(Nov.), 3169–3190.
- Corbett Moran, C., Teyssier, R., & Li, B. 2014. *Arxiv e-prints*, Aug.
- Davé, R., Hernquist, L., Weinberg, D. H., & Katz, N. 1997. *ApJ*, **477**(Mar.), 21–26.
- Davis, A.-C., Lim, E. A., Sakstein, J., & Shaw, D. J. 2012. *Phys. Rev. D*, **85**(12), 123006.
- De Felice, A., & Tsujikawa, S. 2010. *Living reviews in relativity*, **13**(Dec.), 3.
- Dolag, K., Hansen, F. K., Roncarelli, M., & Moscardini, L. 2005. *MNRAS*, **363**(Oct.), 29–39.
- Dossett, J., Hu, B., & Parkinson, D. 2014. *Arxiv e-prints: 1401.3980*, Jan.
- Dvali, G., Gabadadze, G., & Porrati, M. 2000. *Physics letters b*, **485**(July), 208–214.
- Faucher-Giguère, C.-A., Prochaska, J. X., Lidz, A., Hernquist, L., & Zaldarriaga, M. 2008. *ApJ*, **681**(July), 831–855.

11 Bibliography

- Ferraro, S., Schmidt, F., & Hu, W. 2011. *Phys. Rev. D*, **83**(6), 063503.
- Fontanot, F., Puchwein, E., Springel, V., & Bianchi, D. 2013. *MNRAS*, **436**(Dec.), 2672–2679.
- Friedmann, A. 1922. *Zeitschrift für physik*, **10**, 377–386.
- Górski, K. M., Hivon, E., Banday, A. J., Wandelt, B. D., Hansen, F. K., Reinecke, M., & Bartelmann, M. 2005. *ApJ*, **622**(Apr.), 759–771.
- Gronke, M., Llinares, C., Mota, D. F., & Winther, H. A. 2015. *MNRAS*, **449**(May), 2837–2844.
- Haardt, F., & Madau, P. 2012. *ApJ*, **746**(Feb.), 125.
- Hagala, R., Llinares, C., & Mota, D. F. 2016. *Arxiv e-prints*, July.
- Hall, Melanie, Courteau, Stéphane, Dutton, Aaron A, McDonald, Michael, & Zhu, Yucong. 2012. *Monthly notices of the royal astronomical society*, **425**(4), 2741–2765.
- Hammami, A., Llinares, C., Mota, D. F., & Winther, H. A. 2015. *MNRAS*, **449**(June), 3635–3644.
- He, J.-h., Li, B., & Hawken, A. J. 2015. *Phys. Rev. D*, **92**(10), 103508.
- Hinterbichler, K., & Khoury, J. 2010. *Physical review letters*, **104**(23), 231301.
- Hinterbichler, K., Khoury, J., Levy, A., & Matas, A. 2011. *Phys. Rev. D*, **84**(10), 103521.
- Hu, B., Liguori, M., Bartolo, N., & Matarrese, S. 2013. *Phys. Rev. D*, **88**(12), 123514.
- Hu, W., & Sawicki, I. 2007. *Phys. Rev. D*, **76**(6), 064004.
- Hui, L., Nicolis, A., & Stubbs, C. W. 2009. *Phys. Rev. D*, **80**(10), 104002.
- Ivezic, Z., Tyson, J. A., Abel, B., Acosta, E., Allsman, R., AlSayyad, Y., Anderson, S. F., Andrew, J., Angel, R., Angeli, G., Ansari, R., Antilogus, P., Arndt, K. T., Astier, P., Aubourg, E., Axelrod, T., Bard, D. J., Barr, J. D., Barrau, A., Bartlett, J. G., Bauman, B. J., Beaumont, S., Becker, A. C., Becla, J., Beldica, C., Bellavia, S., Blanc, G., Blandford, R. D., Bloom, J. S., Bogart, J., Borne, K., Bosch, J. F., Boutigny, D., Brandt, W. N., Brown, M. E., Bullock, J. S., Burchat, P., Burke, D. L., Cagnoli, G., Calabrese, D., Chandrasekharan, S., Chesley, S., Cheu, E. C., Chiang, J., Claver, C. F., Connolly, A. J., Cook, K. H., Cooray, A., Covey, K. R., Cribbs, C., Cui, W., Cutri, R., Daubard, G., Daues, G., Delgado, F., Digel, S., Doherty, P., Dubois, R., Dubois-Felsmann, G. P., Durech, J., Eracleous, M., Ferguson, H., Frank, J., Freemon, M., Gangler, E., Gawiser, E., Geary, J. C.,

- Gee, P., Geha, M., Gibson, R. R., Gilmore, D. K., Glanzman, T., Goodenow, I., Gressler, W. J., Gris, P., Guyonnet, A., Hascall, P. A., Haupt, J., Hernandez, F., Hogan, C., Huang, D., Huffer, M. E., Innes, W. R., Jacoby, S. H., Jain, B., Jee, J., Jernigan, J. G., Jevremovic, D., Johns, K., Jones, R. L., Juramy-Gilles, C., Juric, M., Kahn, S. M., Kalirai, J. S., Kallivayalil, N., Kalmbach, B., Kantor, J. P., Kasliwal, M. M., Kessler, R., Kirkby, D., Knox, L., Kotov, I., Krabbendam, V. L., Krughoff, S., Kubanek, P., Kuczewski, J., Kulkarni, S., Lambert, R., Le Guillou, L., Levine, D., Liang, M., Lim, K., Lintott, C., Lupton, R. H., Mahabal, A., Marshall, P., Marshall, S., May, M., McKercher, R., Migliore, M., Miller, M., Mills, D. J., Monet, D. G., Moniez, M., Neill, D. R., Nief, J., Nomerotski, A., Nordby, M., O'Connor, P., Oliver, J., Olivier, S. S., Olsen, K., Ortiz, S., Owen, R. E., Pain, R., Peterson, J. R., Petry, C. E., Pierfederici, F., Pietrowicz, S., Pike, R., Pinto, P. A., Plante, R., Plate, S., Price, P. A., Prouza, M., Radeka, V., Rajagopal, J., Rasmussen, A., Regnault, N., Ridgway, S. T., Ritz, S., Rosing, W., Roucelle, C., Rumore, M. R., Russo, S., Saha, A., Sassolas, B., Schalk, T. L., Schindler, R. H., Schneider, D. P., Schumacher, G., Sebag, J., Sembroski, G. H., Seppala, L. G., Shipsey, I., Silvestri, N., Smith, J. A., Smith, R. C., Strauss, M. A., Stubbs, C. W., Sweeney, D., Szalay, A., Takacs, P., Thaler, J. J., Van Berg, R., Vanden Berk, D., Vetter, K., Virieux, F., Xin, B., Walkowicz, L., Walter, C. W., Wang, D. L., Warner, M., Willman, B., Wittman, D., Wolff, S. C., Wood-Vasey, W. M., Yoachim, P., Zhan, H., & for the LSST Collaboration. 2008. *Arxiv e-prints*, May.
- Jain, B., & Khoury, J. 2010. *Annals of physics*, **325**(July), 1479–1516.
- Jain, B., Vikram, V., & Sakstein, J. 2013. *ApJ*, **779**(Dec.), 39.
- Jennings, E., Baugh, C. M., Li, B., Zhao, G.-B., & Koyama, K. 2012. *MNRAS*, **425**(Sept.), 2128–2143.
- Joyce, A., Jain, B., Khoury, J., & Trodden, M. 2015. *Phys. Rep.*, **568**(Mar.), 1–98.
- Khoury, J., & Weltman, A. 2004a. *Phys. Rev. D*, **69**(4), 044026.
- Khoury, J., & Weltman, A. 2004b. *Physical review letters*, **93**(17), 171104.
- Kim, T.-S., Bolton, J. S., Viel, M., Haehnelt, M. G., & Carswell, R. F. 2007. *MNRAS*, **382**(Dec.), 1657–1674.
- Koyama, K. 2016. *Reports on progress in physics*, **79**(4), 046902.
- Lam, T. Y., Nishimichi, T., Schmidt, F., & Takada, M. 2012. *Physical review letters*, **109**(5), 051301.
- Li, B., Zhao, G.-B., Teyssier, R., & Koyama, K. 2012. *JCAP*, **1**(Jan.), 51.
- Li, B., Zhao, G.-B., & Koyama, K. 2013a. *JCAP*, **5**(May), 023.

11 Bibliography

- Li, B., Barreira, A., Baugh, C. M., Hellwing, W. A., Koyama, K., Pascoli, S., & Zhao, G.-B. 2013b. *JCAP*, **11**(Nov.), 012.
- Li, B., Hellwing, W. A., Koyama, K., Zhao, G.-B., Jennings, E., & Baugh, C. M. 2013c. *MNRAS*, **428**(Jan.), 743–755.
- Li, Y., & Hu, W. 2011. *Phys. Rev. D*, **84**(8), 084033.
- Llinares, C., & Mota, D. F. 2014. *Phys. Rev. D*, **89**(8), 084023.
- Llinares, C., Mota, D. F., & Winther, H. A. 2014a. *A&A*, **562**(Feb.), A78.
- Llinares, C., Mota, D. F., & Winther, H. A. 2014b. *A&A*, **562**(Feb.), A78.
- Lombriser, L., Koyama, K., Zhao, G.-B., & Li, B. 2012a. *Phys. Rev. D*, **85**(12), 124054.
- Lombriser, L., Schmidt, F., Baldauf, T., Mandelbaum, R., Seljak, U., & Smith, R. E. 2012b. *Phys. Rev. D*, **85**(10), 102001.
- Lombriser, L., Li, B., Koyama, K., & Zhao, G.-B. 2013. *Phys. Rev. D*, **87**(12), 123511.
- Lombriser, L., Koyama, K., & Li, B. 2014. *JCAP*, **3**(Mar.), 021.
- Marinacci, F., Pakmor, R., & Springel, V. 2014. *MNRAS*, **437**(Jan.), 1750–1775.
- McDonald, P., Seljak, U., Burles, S., Schlegel, D. J., Weinberg, D. H., Cen, R., Shih, D., Schaye, J., Schneider, D. P., Bahcall, N. A., Briggs, J. W., Brinkmann, J., Brunner, R. J., Fukugita, M., Gunn, J. E., Ivezić, Ž., Kent, S., Lupton, R. H., & Vanden Berk, D. E. 2006. *ApJS*, **163**(Mar.), 80–109.
- McGaugh, Stacy S. 2012. *The astronomical journal*, **143**(2), 40.
- McQuinn, M., Lidz, A., Zaldarriaga, M., Hernquist, L., Hopkins, P. F., Dutta, S., & Faucher-Giguère, C.-A. 2009. *ApJ*, **694**(Apr.), 842–866.
- Navarro, J. F., Frenk, C. S., & White, S. D. M. 1997. *ApJ*, **490**(Dec.), 493–508.
- Neto, A. F., Gao, L., Bett, P., Cole, S., Navarro, J. F., Frenk, C. S., White, S. D. M., Springel, V., & Jenkins, A. 2007. *MNRAS*, **381**(Nov.), 1450–1462.
- Nicolis, A., Rattazzi, R., & Trincherini, E. 2009. *Phys. Rev. D*, **79**(6), 064036.
- Noller, J., von Braun-Bates, F., & Ferreira, P. G. 2014. *Phys. Rev. D*, **89**(2), 023521.
- Oyaizu, H. 2008. *Phys. Rev. D*, **78**(12), 123523.
- Pakmor, R., Marinacci, F., & Springel, V. 2014. *ApJ*, **783**(Mar.), L20.

- Peebles, P. J. E., & Ratra, B. 1988. *ApJ*, **325**(Feb.), L17–L20.
- Peirone, S., Raveri, M., Viel, M., Borgani, S., & Ansoldi, S. 2016. *Arxiv e-prints*, July.
- Pfrommer, C., Pakmor, R., Schaal, K., Simpson, C. M., & Springel, V. 2017. *MNRAS*, **465**(Mar.), 4500–4529.
- Planck Collaboration, Aghanim, N., Arnaud, M., Ashdown, M., Aumont, J., Baccigalupi, C., Balbi, A., Banday, A. J., Barreiro, R. B., Bartelmann, M., & et al. 2011. *A&A*, **536**(Dec.), A12.
- Planck Collaboration, Ade, P. A. R., Aghanim, N., Arnaud, M., Ashdown, M., Atrio-Barandela, F., Aumont, J., Baccigalupi, C., Balbi, A., Banday, A. J., Barreiro, R. B., Bartlett, J. G., Battaner, E., Battye, R., Benabed, K., Bernard, J.-P., Bersanelli, M., Bhatia, R., Bikmaev, I., Böhringer, H., Bonaldi, A., Bond, J. R., Borgani, S., Borrill, J., Bouchet, F. R., Bourdin, H., Brown, M. L., Bucher, M., Burenin, R., Burigana, C., Butler, R. C., Cabella, P., Cardoso, J.-F., Carvalho, P., Chamballu, A., Chiang, L.-Y., Chon, G., Clements, D. L., Colafrancesco, S., Coulais, A., Cuttaia, F., Da Silva, A., Dahle, H., Davis, R. J., de Bernardis, P., de Gasperis, G., Delabrouille, J., Démoclès, J., Désert, F.-X., Diego, J. M., Dolag, K., Dole, H., Donzelli, S., Doré, O., Douspis, M., Dupac, X., Efstathiou, G., Enßlin, T. A., Eriksen, H. K., Finelli, F., Flores-Cacho, I., Forni, O., Frailis, M., Franceschi, E., Frommert, M., Galeotta, S., Ganga, K., Génova-Santos, R. T., Giard, M., Giraud-Héraud, Y., González-Nuevo, J., Górski, K. M., Gregorio, A., Gruppuso, A., Hansen, F. K., Harrison, D., Hernández-Monteagudo, C., Herranz, D., Hildebrandt, S. R., Hivon, E., Hobson, M., Holmes, W. A., Hufferberger, K. M., Hurier, G., Jagemann, T., Juvela, M., Keihänen, E., Khamitov, I., Kneissl, R., Knoche, J., Kunz, M., Kurki-Suonio, H., Lagache, G., Lamarre, J.-M., Lasenby, A., Lawrence, C. R., Le Jeune, M., Leach, S., Leonardi, R., Liddle, A., Lilje, P. B., Linden-Vørnle, M., López-Caniego, M., Luzzi, G., Macías-Pérez, J. F., Maino, D., Mandolesi, N., Maris, M., Marleau, F., Marshall, D. J., Martínez-González, E., Masi, S., Matarrese, S., Matthai, F., Mazzotta, P., Meinhold, P. R., Melchiorri, A., Melin, J.-B., Mendes, L., Mitra, S., Miville-Deschênes, M.-A., Montier, L., Morgante, G., Munshi, D., Natoli, P., Nørgaard-Nielsen, H. U., Noviello, F., Osborne, S., Pajot, F., Paoletti, D., Partridge, B., Pearson, T. J., Perdereau, O., Perrotta, F., Piacentini, F., Piat, M., Pierpaoli, E., Piffaretti, R., Platania, P., Pointecouteau, E., Polenta, G., Ponthieu, N., Popa, L., Poutanen, T., Pratt, G. W., Prunet, S., Puget, J.-L., Rachen, J. P., Rebolo, R., Reinecke, M., Remazeilles, M., Renault, C., Ricciardi, S., Ristorcelli, I., Rocha, G., Rosset, C., Rossetti, M., Rubiño-Martín, J. A., Rusholme, B., Sandri, M., Savini, G., Scott, D., Starck, J.-L., Stivoli, F., Stolyarov, V., Sudiwala, R., Sunyaev, R., Sutton, D., Suur-Uski, A.-S., Sygnet, J.-F., Tauber, J. A., Terenzi, L., Toffolatti, L., Tomasi, M., Tristram, M., Valenziano, L., Van Tent, B., Vielva, P., Villa, F., Vittorio, N.,

11 Bibliography

- Wandelt, B. D., Weller, J., White, S. D. M., Yvon, D., Zacchei, A., & Zonca, A. 2013a. *A&A*, **550**(Feb.), A129.
- Planck Collaboration, Ade, P. A. R., Aghanim, N., Arnaud, M., Ashdown, M., Atrio-Barandela, F., Aumont, J., Baccigalupi, C., Balbi, A., Banday, A. J., & et al. 2013b. *A&A*, **557**(Sept.), A52.
- Planck Collaboration, Ade, P. A. R., Aghanim, N., Arnaud, M., Ashdown, M., Aumont, J., Baccigalupi, C., Banday, A. J., Barreiro, R. B., Bartlett, J. G., & et al. 2016a. *A&A*, **594**(Sept.), A13.
- Planck Collaboration, Aghanim, N., Arnaud, M., Ashdown, M., Aumont, J., Baccigalupi, C., Banday, A. J., Barreiro, R. B., Bartlett, J. G., Bartolo, N., & et al. 2016b. *A&A*, **594**(Sept.), A22.
- Puchwein, E., Pfrommer, C., Springel, V., Broderick, A. E., & Chang, P. 2012. *MNRAS*, **423**(June), 149–164.
- Puchwein, E., Baldi, M., & Springel, V. 2013. *MNRAS*, **436**(Nov.), 348–360.
- Puchwein, E., Bolton, J. S., Haehnelt, M. G., Madau, P., & Becker, G. D. 2014. *Arxiv e-print: 1410.1531*, Oct.
- Riess, A. G., Filippenko, A. V., Challis, P., Clocchiatti, A., Diercks, A., Garnavich, P. M., Gilliland, R. L., Hogan, C. J., Jha, S., Kirshner, R. P., Leibundgut, B., Phillips, M. M., Reiss, D., Schmidt, B. P., Schommer, R. A., Smith, R. C., Spyromilio, J., Stubbs, C., Suntzeff, N. B., & Tonry, J. 1998. *AJ*, **116**(Sept.), 1009–1038.
- Rollinde, E., Theuns, T., Schaye, J., Pâris, I., & Petitjean, P. 2013. *MNRAS*, **428**(Jan.), 540–550.
- Rozo, E., Evrard, A. E., Rykoff, E. S., & Bartlett, J. G. 2014. *MNRAS*, **438**(Feb.), 62–77.
- Sakstein, J. 2013. *Phys. Rev. D*, **88**(12), 124013.
- Sawicki, I., & Bellini, E. 2015. *Phys. Rev. D*, **92**(8), 084061.
- Schäfer, B. M., Pfrommer, C., Bartelmann, M., Springel, V., & Hernquist, L. 2006. *MNRAS*, **370**(Aug.), 1309–1323.
- Schaye, J., Crain, R. A., Bower, R. G., Furlong, M., Schaller, M., Theuns, T., Dalla Vecchia, C., Frenk, C. S., McCarthy, I. G., Helly, J. C., Jenkins, A., Rosas-Guevara, Y. M., White, S. D. M., Baes, M., Booth, C. M., Camps, P., Navarro, J. F., Qu, Y., Rahmati, A., Sawala, T., Thomas, P. A., & Trayford, J. 2015. *MNRAS*, **446**(Jan.), 521–554.

- Schmidt, F. 2010. *Phys. Rev. D*, **81**(10), 103002.
- Schmidt, F., Lima, M., Oyaizu, H., & Hu, W. 2009. *Phys. Rev. D*, **79**(8), 083518.
- Schneider, A., Teyssier, R., Potter, D., Stadel, J., Onions, J., Reed, D. S., Smith, R. E., Springel, V., Pearce, F. R., & Scoccimarro, R. 2016. *JCAP*, **4**(Apr.), 047.
- Smith, T. L. 2009. *Arxiv e-prints: 0907.4829*, July.
- Sotiriou, T. P. 2006. *Classical and quantum gravity*, **23**(Feb.), 1253–1267.
- Sotiriou, T. P., & Faraoni, V. 2010. *Reviews of modern physics*, **82**(Jan.), 451–497.
- Springel, V. 2005. *MNRAS*, **364**(Dec.), 1105–1134.
- Springel, V. 2010. *MNRAS*, **401**(Jan.), 791–851.
- Springel, V., & Hernquist, L. 2002. *MNRAS*, **333**(July), 649–664.
- Springel, V., White, S. D. M., Tormen, G., & Kauffmann, G. 2001. *MNRAS*, **328**(Dec.), 726–750.
- Springel, V., White, S. D. M., Jenkins, A., Frenk, C. S., Yoshida, N., Gao, L., Navarro, J., Thacker, R., Croton, D., Helly, J., Peacock, J. A., Cole, S., Thomas, P., Couchman, H., Evrard, A., Colberg, J., & Pearce, F. 2005. *Nature*, **435**(June), 629–636.
- Springel, V., Wang, J., Vogelsberger, M., Ludlow, A., Jenkins, A., Helmi, A., Navarro, J. F., Frenk, C. S., & White, S. D. M. 2008. *MNRAS*, **391**(Dec.), 1685–1711.
- Sunyaev, R. A., & Zeldovich, Y. B. 1972. *Comments on astrophysics and space physics*, **4**(Nov.), 173.
- Terukina, A., Lombriser, L., Yamamoto, K., Bacon, D., Koyama, K., & Nichol, R. C. 2014. *JCAP*, **4**(Apr.), 013.
- Teyssier, R. 2002. *A&A*, **385**(Apr.), 337–364.
- Viel, M., Bolton, J. S., & Haehnelt, M. G. 2009. *MNRAS*, **399**(Oct.), L39–L43.
- Vikram, V., Sakstein, J., Davis, C., & Neil, A. 2014. *Arxiv e-prints*, July.
- Vogelsberger, M., Genel, S., Springel, V., Torrey, P., Sijacki, D., Xu, D., Snyder, G., Nelson, D., & Hernquist, L. 2014a. *MNRAS*, **444**(Oct.), 1518–1547.
- Vogelsberger, M., Genel, S., Springel, V., Torrey, P., Sijacki, D., Xu, D., Snyder, G., Bird, S., Nelson, D., & Hernquist, L. 2014b. *Nature*, **509**(May), 177–182.
- Vollick, D. N. 2003. *Phys. Rev. D*, **68**(6), 063510.

11 Bibliography

- Weinberger, R., Springel, V., Hernquist, L., Pillepich, A., Marinacci, F., Pakmor, R., Nelson, D., Genel, S., Vogelsberger, M., Naiman, J., & Torrey, P. 2017. *MNRAS*, **465**(Mar.), 3291–3308.
- Wetterich, C. 1988. *Nuclear physics b*, **302**(June), 668–696.
- Wetterich, C. 1995. *A&A*, **301**(Sept.), 321.
- Will, C. M. 2014. *Living reviews in relativity*, **17**(Dec.), 4.
- Winther, H. A., & Ferreira, P. G. 2014. *Arxiv e-prints*, Mar.
- Winther, H. A., Schmidt, F., Barreira, A., Arnold, C., Bose, S., Llinares, C., Baldi, M., Falck, B., Hellwing, W. A., Koyama, K., Li, B., Mota, D. F., Puchwein, E., Smith, R. E., & Zhao, G.-B. 2015. *MNRAS*, **454**(Dec.), 4208–4234.
- Zhao, G.-B., Li, B., & Koyama, K. 2011. *Physical review letters*, **107**(7), 071303.
- Zivick, P., Sutter, P. M., Wandelt, B. D., Li, B., & Lam, T. Y. 2015. *MNRAS*, **451**(Aug.), 4215–4222.

